Title

Creep Behavior of Additively Manufactured, Oxide Dispersion Strengthened, and Refractory Multi-Principal Element Alloys

Permalink

https://escholarship.org/uc/item/85m3w3k0

Author

Sahragard-Monfared, Gianmarco

Publication Date

2023

Peer reviewed|Thesis/dissertation

Creep Behavior of Additively Manufactured, Oxide Dispersion Strengthened, and Refractory Multi-Principal Element Alloys

By

GIANMARCO SAHRAGARD-MONFARED

DISSERTATION

Submitted in partial satisfaction of the requirements for the degree of

DOCTOR OF PHILOSOPHY

in

Materials Science and Engineering

in the

OFFICE OF GRADUATE STUDIES

of the

UNIVERSITY OF CALIFORNIA

DAVIS

Approved:

Jeffery C. Gibeling, Chair

Troy D. Topping

Jeremy K. Mason

Committee in Charge

2023

i

This dissertation is dedicated to my late father, Ahmad, my beautiful wife, Morgen, without whom the completion of this dissertation would not have been possible, my parents, Francesca and Akbar, who have been a constant source of encouragement, my brother, Giampiero, who has always been there for me, and my son, Ardalan, who makes it all worthwhile.

Abstract

This study investigates the influence of processing methods and oxide dispersion strengthening (ODS) on the creep behavior and deformation mechanisms of several multi-principal element alloys (MPEA). The effect of a BCC crystal structure composed of refractory elements on the creep behavior of MPEAs is also investigated. The materials examined are equiatomic wrought and additively manufactured (AM) CrCoNi, equiatomic AM ODS CrCoNi, and wrought $Nb_{45}Ta_{25}Ti_{15}Hf_{15}$. Constant stress creep tests were performed on all materials to determine stress exponents and activation energies. Stress reduction creep tests were conducted on AM CrCoNi and AM ODS CrCoNi to characterize activation areas and subsequently their rate-controlling deformation mechanisms during steady state creep. Scanning electron microscopy (SEM) was utilized to characterize initial microstructures, atomic compositions, and fracture surfaces. Pre- and post-creep dislocation structures were characterized by transmission electron microscopy (TEM). Stress exponents of 4.5 ± 0.2, 5.9 ± 0.1, 6.5 ± 0.1 were determined for wrought CrCoNi, AM CrCoNi, and AM ODS CrCoNi, respectively. These results indicate that the stress dependence of the creep behavior is different for each of these FCC MPEAs and thus they have unique creep deformation mechanisms. Activation energy ranges of $240 - 259$ kJ/mol, $320 - 331$ kJ/mol, and $335 - 367$ kJ/mol were found for wrought CrCoNi, AM CrCoNi, and AM ODS CrCoNi, respectively. The increasing activation energy ranges reflect the improved temperature resistance of these FCC alloys. The $Nb_{45}Ta_{25}Ti_{15}Hf_{15}$ exhibited creep properties superior to the investigated FCC MPEAs at all but the lowest values of applied stress, with its creep deformation behavior being attributed to thermally activated and stress assisted dislocation glide.

The AM material exhibited superior creep resistance and inferior creep ductility compared to wrought alloy. This difference was attributed to the AM material having a higher percentage of

Cr-rich oxides, a lower percentage of low angle grain boundaries (LAGB), and a higher percentage of twin boundaries (TB). Three types of Cr-rich oxides were observed via TEM/STEM-EDS in the AM material, leading to dislocation interactions with these oxide particles as well as contributing to the nucleation of voids leading to fracture. Essentially no oxides were found in the wrought material. The AM material has a lower LAGB density than the wrought material, leading to fewer dislocation pile-up stress concentrations in the wrought material due to the propensity to propagate deformation more readily through LAGBs. The higher density of TBs in the AM material do not act as dislocation sources, thereby reducing the possibility of slip transmission on the other side of the boundary. The steady state dislocation structures of the AM and wrought material consist of individual curved dislocations with dislocation multijunctions and jogs.

Compared to its non-ODS counterpart, AM ODS CrCoNi has superior creep resistance at all tested stresses and temperatures. The excellent creep resistance of AM ODS CrCoNi was attributed to the interaction of mixed character dislocations with oxide particles. The creep ductility of AM ODS CrCoNi was higher than its non-ODS counterpart due to a large percentage of low angle grain boundaries associated with its columnar grain structure. It was also found that creep ductility is significantly greater at the highest applied stress of 200 MPa compared to lower stresses. The steady state dislocation structure of AM ODS CrCoNi consists of long arrays of dislocations which is different than that observed in non-ODS CrCoNi which consists of individual curved dislocations.

Operational activation areas were determined to be 900 b^2 for AM ODS CrCoNi and 940 b^2 for AM CrCoNi. These operational activation areas are indicative of forest dislocation controlled steady state creep, which is consistent with the dislocation structures observed in these alloys.

The operational activation area of AM CrCoNi is significantly higher than the values reported for CrMnFeCoNi, revealing a difference in rate controlling mechanism. The quinary alloy is rate limited by a combination of dislocation interactions with forest dislocations and the solid solution matrix, and the simplified ternary alloy is controlled solely by forest dislocation strengthening. Similarly, the operational activation area of AM ODS CrCoNi is significantly higher than the values reported for other ODS alloys, indicating that the volume fraction of oxides in AM ODS CrCoNi is too low to effectively limit the rate of dislocation motion, and revealing that the thermal activation of dislocation glide is instead limited by forest dislocations. However, the particles limit the area swept by gliding dislocations resulting in less strain per activation event.

Creep behavior in $Nb_{45}Ta_{25}Ti_{15}Hf_{15}$ was characterized by both the power law creep model and the thermally activated dislocation glide model. Utilizing the power law creep model, a stress exponent of 1.2 was measured at low applied stresses suggesting diffusion controlled creep occurs in this regime. A stress exponent of 5.7 was measured at high applied stresses implying dislocation climb controlled creep in the high stress regime. However, an exponential relationship provides a better fit of the creep data, suggesting that the conventional phenomenological power law approach does not accurately describe the creep behavior in this material. The exponential approach is consistent with the thermally activated and stress assisted dislocation glide description of the rate controlling mechanism for creep deformation in $Nb_{45}Ta_{25}Ti_{15}Hf_{15}$. Brittle intergranular fracture was observed as a result of Hf-oxide formation at grain boundaries. This brittle intergranular fracture decreased creep ductility, creep life, and creep rate, especially at low applied stresses where extended exposure to oxygen resulted in more extensive brittle intergranular fracture.

Acknowledgments

Many people have provided support, mentorship, and love along my path to completing this dissertation. I could not imagine being in the position that I am now without their combined efforts. I am truly grateful for everyone who has contributed to my journey thus far.

I would like to begin by acknowledging the many years of love and support provided to me by my parents, Francesca and Akbar, and my brother, Giampiero. You have each aided in shaping me into the person I am today. Your influence certainly sparked my desire for knowledge and unbounded curiosity. Thank for all you have done.

My wife, Morgen, has truly been a driving force in my life since the day we met. She has always seen my potential and encouraged me to achieve everything she knew was possible, including the completion of this dissertation. She has done so even with the knowledge that it would require her to provide immeasurable support, which she has always managed to provide with love in her heart. I love you and am excited to see what the next chapter of our life has in store for us.

Ardalan, my son, you made your grand appearance roughly halfway through the completion of my PhD. I love you more than words can describe. Your contagious laugh, your ability to make friends everywhere you go, and your endless curiosity have all helped me to persevere through the inherent difficulties of earning a PhD. I hope to inspire you and guide you on your chosen path in life.

Thank you to my lab mates and friends, Bill Bania, Dayane Oliveira, Christine Smudde, Mingwei Zhang, and Will Hahn with whom I have had countless conversations regarding my research. Thank you all for your friendship.

I would also like to acknowledge all of the gracious mentors that I have had over the years who have guided my academic journey. Thank you to Susan Holl, Troy Topping, Patrick Homen, and Susan Gentry. You have all gone above and beyond to provide me with the tools that I need to be successful. My academic journey has been heavily influenced by each of you and for that I am grateful.

Thank you to Dr. Easo George of Oak Ridge National Laboratory, Dr. Timothy Smith of NASA Glenn Research Center, Dr. Mingwei Zhang and Dr. Andrew Minor of Lawrence Berkeley National Laboratory, Calvin Belcher, Dr. Cheng Zhang, Dr. Diran Apelian, and Dr. Enrique Lavernia of the University of California, Irvine for the collaborations and research guidance that you have provided. I am grateful for the research opportunities provided by each of you and our insightful discussions.

Thank you to Dr. Subhash Risbud, Dr. Ricardo Castro, Dr. Michael Hill, Dr. Scott McCormack, and again to Dr. Susan Gentry for serving on my qualifying exam committee and providing superb guidance throughout my PhD. Thank you to Dr. Jeremy Mason and again to Dr. Troy Topping for serving on my dissertation committee, I truly appreciate your excellent feedback and guidance.

Last but by no stretch of the imagination least, I would like to thank my wonderful PhD advisor Dr. Jeffery Gibeling. I could not have asked for a more knowledgeable, humorous, or compassionate advisor. You have taught me so much during my time at the University of California, Davis and I am truly proud to call you my advisor and to carry on your legacy. I am also grateful for Marsha Gibeling as she has sacrificed precious time with you as we have spent early mornings and late nights in the laboratory and revising papers. Thank you both for your generosity.

Table of Contents

List of Figures

List of Tables

Chapter 1. Introduction

The structural materials community has recently become interested in the high temperature creep properties of a new class of alloys termed multi-principal element alloys (MPEA) since their discovery in 2004 by Yeh, et al. and Cantor, et al. [1, 2]. MPEAs consist of three to five elements, each present at a minimum of ten atomic percent. Interest in the creep properties of MPEAs stems from significant solid solution strengthening which provides consistent creep strength at high temperatures [3, 4]. Other strengthening mechanisms such as grain boundary strengthening and precipitation hardening used in Ni-based superalloys are limited at high temperatures by diffusion and precipitate degradation effects. The primary class of MPEAs is single phase FCC CrCoNi-based alloys that exhibit excellent room temperature and cryogenic strength and ductility as well as superb oxidation and corrosion resistance [5, 6]. However, the creep resistance of even the best FCC MPEAs have thus far not surpassed that of superalloys which have undergone continuous development for nearly a century. Although the compositional design space of MPEAs is nearly infinite and thus still being explored, investigators have attempted to increase their creep strength through other means such as oxide dispersion strengthening (ODS), another stable high temperature strengthening mechanism [7, 8]. The addition of oxides in the MPEA matrix results in dislocation/oxide interactions which hinder creep deformation and thus increase creep strength. Although these ODS MPEAs exhibit superior creep properties compared to their non-ODS counterparts, their creep resistance still falls short of well-established superalloys.

In 2010, Senkov, et al. applied the concept of MPEAs to BCC refractory metals to take advantage of their higher strength and melting temperature as compared to their FCC counterparts [9, 10]. Although BCC alloys typically have low ductility, tailoring of the refractory

MPEA (RMPEA) design space such as the use of Nb to reduce the ductile to brittle transition temperature and provide oxidation resistance, Ta and Ti to promote solid solution strengthening, and Hf for grain boundary strengthening has been utilized to achieve excellent ductility while maintaining high strength [11-14]. Despite the prediction of excellent creep strength in RMPEAs since their discovery, their creep properties have only recently been reported in two studies to date [15, 16]. Although RMPEAs exhibit creep resistance superior to FCC MPEAs, they still fall slightly short of conventional superalloys. However, the fact that the creep resistance of MPEAs has been steadily approaching that of superalloys after only thirteen years of development, with the potential for higher temperature applications due to the higher melting points of RMPEAs, is extremely encouraging. Additionally, ODS has not yet been utilized to further enhance the creep properties of RMPEAs.

A fundamental understanding of the high temperature mechanistic behavior of MPEAs is critical for confident utilization of these alloys in energy conversion systems and other applications in extreme environments. Processing methods such as vacuum arc melting, spark plasma sintering, and additive manufacturing (AM) produce alloys with different mechanical properties even when the compositions are the same. Investigations of the effects of various processing methods on MPEAs found significant differences in microstructure, room temperature mechanical properties, and strengthening mechanisms among the methods [17, 18]. However, the effect of processing methods on tensile creep properties has not been investigated to date. Similarly, although ODS has been used to strengthen MPEAs and the creep properties of ODS MPEAs have been measured [7, 8], the underlying rate controlling creep deformation mechanisms of ODS MPEAs have thus far not been investigated. In order to tailor the compositions of MPEAs to effectively utilize strengthening mechanisms such as ODS, the mechanistic effect of oxides on creep

deformation must be understood in these alloys. Additionally, only the constant load tensile creep behavior of a single RMPEA (the Senkov alloy) has been investigated to date. To promote the continuous development of this new class of alloys the creep behavior of new, well designed, compositions must be investigated. Therefore, the work described in this dissertation aims to investigate the influence of processing methods, the effect of ODS, and the effect of a BCC crystal structure comprised of refractory metals on the constant stress creep behavior of MPEAs, as well as their rate controlling creep deformation mechanisms. The studies comprising this dissertation represent a logical sequence of investigations with the long-term goal of developing an ODS RMPEA.

The results of this dissertation are divided into four independent chapters which have also been or are intended to be submitted to scientific journals, described as follows. The work described in Chapter 2 investigates the influence of processing methods on the creep behavior of an equiatomic CrCoNi MPEA. Constant stress tensile creep tests and microstructural characterization of a wrought and AM version of the material are utilized to infer the effects of the different processing methods on creep behavior. Unintentional Cr-rich oxides in AM CrCoNi introduced by the AM process as well as a low percentage of low angle grain boundaries compared to wrought CrCoNi result in higher creep resistance and lower creep ductility in the AM material compared to the wrought material. The study in Chapter 2 is a collaboration with Dr. Timothy M. Smith of NASA Glenn Research Center (NASA GRC), Dr. Mingwei Zhang and Dr. Andrew Minor of Lawrence Berkeley National Laboratory (LBNL), and Dr. Easo P. George of Oak Ridge National Laboratory. The work described in Chapter 3 examines the creep behavior of AM CrCoNi that is strengthened with yttrium oxide, termed AM ODS CrCoNi, highlighting the strengthening effect of ODS in MPEAs. It is found that AM ODS CrCoNi has

the best combination of tensile creep strength and ductility of all FCC MPEAs investigated to date with enhanced creep ductility at high stress due to a large percentage of low angle grain boundaries. Enhanced creep ductility at high stress is determined to be caused by a large percentage of low angle grain boundaries. This study is a collaboration with Dr. Timothy M. Smith of NASA GRC, Dr. Mingwei Zhang and Dr. Andrew Minor of LBNL. The study in Chapter 4 is a collaboration with Dr. Timothy M. Smith of NASA GRC and extends Chapters 2 and 3 to investigate creep deformation mechanisms of AM and AM ODS CrCoNi. Stress reduction creep tests are utilized to probe deformation under conditions of constant dislocation structure to calculate operational activation areas from which rate controlling creep deformation mechanisms can be inferred. The rate controlling mechanism in AM and AM ODS CrCoNi is determined to be forest dislocation interactions. The work described in Chapter 5 extends beyond the FCC MPEAs investigated thus far to examine the creep behavior of a $Nb_{45}Ta_{25}Ti_{15}Hf_{15}$ refractory MPEA (RMPEA). In addition to reporting the excellent high stress creep behavior of $Nb_{45}Ta_{25}Ti_{15}Hf_{15}$, this study also suggests that currently published creep results for RMPEAs in the low stress regime are artificially low due to oxidation effects. This study is a collaboration with Dr. Mingwei Zhang and Dr. Andrew Minor of LBNL, and Calvin H. Belcher, Dr. Cheng Zhang, Dr. Diran Apelian, and Dr. Enrique J. Lavernia of the University of California Irvine. Chapter 6 includes a summary of the results presented in this dissertation as well as insights into potential areas of future research. Additionally, all creep data including creep rates, creep ductilities, and creep rupture times presented in this dissertation are tabulated in the Appendix.

References

[1]   J.W. Yeh, S.K. Chen, S.J. Lin, J.Y. Gan, T.S. Chin, T.T. Shun, C.H. Tsau, S.Y. Chang, Nanostructured high-entropy alloys with multiple principal elements: Novel alloy design concepts and outcomes, Advanced Engineering Materials 6(5) (2004) 299-303.

[2]   B. Cantor, I.T.H. Chang, P. Knight, A.J.B. Vincent, Microstructural development in equiatomic multicomponent alloys, Materials Science and Engineering: A 375-377 (2004) 213-218.

[3]   M. Zhang, E.P. George, J.C. Gibeling, Tensile creep properties of a CrMnFeCoNi high-entropy alloy, Scripta Materialia 194 (2021).

[4]   M. Zhang, E.P. George, J.C. Gibeling, Elevated-temperature deformation mechanisms in a CrMnFeCoNi high-entropy alloy, Acta Materialia 218 (2021).

[5]   B. Gludovatz, A. Hohenwarter, D. Catoor, E.H. Chang, E.P. George, R.O. Ritchie, A fracture-resistant high-entropy alloy for cryogenic applications, Science 345(6201) (2014) 1153-1158.

[6]   G. Laplanche, A. Kostka, C. Reinhart, J. Hunfeld, G. Eggeler, E.P. George, Reasons for the superior mechanical properties of medium-entropy CrCoNi compared to high-entropy CrMnFeCoNi, Acta Materialia 128 (2017) 292-303.

[7]   H. Hadraba, Z. Chlup, A. Dlouhy, F. Dobes, P. Roupcova, M. Vilemova, J. Matejicek, Oxide dispersion strengthened CoCrFeNiMn high-entropy alloy, Materials Science & Engineering A 689 (2017) 252-256.

[8]   F. Dobeš, H. Hadraba, Z. Chlup, A. Dlouhý, M. Vilémová, J. Matějíček, Compressive creep behavior of an oxide-dispersion-strengthened CoCrFeMnNi high-entropy alloy, Materials Science and Engineering: A 732 (2018) 99-104.

[9]   O.N. Senkov, G.B. Wilks, D.B. Miracle, C.P. Chuang, P.K. Liaw, Refractory high-entropy alloys, Intermetallics 18(9) (2010) 1758-1765.

[10]   O.N. Senkov, J.M. Scott, S.V. Senkova, D.B. Miracle, C.F. Woodward, Microstructure and room temperature properties of a high-entropy TaNbHfZrTi alloy, Journal of Alloys and Compounds 509(20) (2011) 6043-6048.

[11]   D.B. Miracle, O.N. Senkov, A critical review of high entropy alloys and related concepts, Acta Materialia 122 (2017) 448-511.

[12]   O.N. Senkov, S. Gorsse, D.B. Miracle, High temperature strength of refractory complex concentrated alloys, Acta Materialia 175 (2019) 394-405.

[13]   C. Zhang, B.E. MacDonald, F.W. Guo, H.R. Wang, C.Y. Zhu, X. Liu, Y.W. Kang, X.C. Xie, Y.Z. Zhou, K.S. Vecchio, E.J. Lavernia, Cold-workable refractory complex concentrated alloys with tunable microstructure and good room-temperature tensile behavior, Scripta Materialia 188 (2020) 16-20.

[14]   C. Zhang, H.R. Wang, X.Y. Wang, Q. Yu, C.Y. Zhu, M.J. Xu, S.T. Zhao, R. Kou, X. Wang, B.E. MacDonald, R.C. Reed, K.S. Vecchio, P.H. Cao, T.J. Rupert, E.J. Lavernia, Strong and ductile refractory high-entropy alloys with super formability, Acta Materialia 245 (2023).

[15]   C. Liu, C. Gadelmeier, S. Lu, J. Yeh, H. Yen, S. Gorsse, U. Glatzel, A. Yeh, Tensile creep behavior of HfNbTaTiZr refractory high entropy alloy at elevated temperatures, Acta Materialia 237 (2022).

[16]   C. Gadelmeier, Y. Yang, U. Glatzel, E.P. George, Creep strength of refractory high-entropy alloy TiZrHfNbTa and comparison with Ni-base superalloy CMSX-4, Cell Reports Physical Science 3(8) (2022).

[17]   K. Sun, W.X. Peng, L.L. Yang, L. Fang, Effect of SLM Processing Parameters on Microstructures and Mechanical Properties of Al0.5CoCrFeNi High Entropy Alloys, Metals 10(2) (2020).

[18]   D. Yang, Y. Liu, N. Qu, T. Han, M. Liao, Z. Lai, J. Zhu, Effect of fabrication methods on
        microstructures, mechanical properties and strengthening mechanisms of Fe0.25CrNiAl
        medium-entropy alloy, Journal of Alloys and Compounds 888 (2021).

Chapter 2. The Influence of Processing Methods on Creep of Wrought and Additively Manufactured CrCoNi Multi-Principal Element Alloys[1]

2.1 Introduction

Multi-principal element alloys (MPEA) are materials in which three to five elements are present at high concentrations and often in roughly equal proportions. The most extensively studied FCC MPEAs are equiatomic CrMnFeCoNi (Cantor alloy) and a derivative, CrCoNi, which have been proven to exhibit excellent room temperature and cryogenic strength and ductility [1-4]. Systematic studies of these alloys have shown that although CrMnCoNi has the highest yield strength and the Cantor alloy is capable of achieving the highest ductility compared to its derivatives, CrCoNi displays the best combination of strength, ductility, and damage tolerance [5, 6]. This favorable combination of properties has been attributed to the formation of nanotwin-HCP lamellae that partition grains into much smaller structural units that can sustain large lattice rotations and contribute to extensive strain hardening [4]. However, limited resistance to deformation at high temperatures has constrained the range of applications of MPEAs to date [7-10].

In order to enhance high temperature and other material properties, several investigators have added Ti, Al, and other elements to essentially create high entropy superalloys similar to conventional Ni-based superalloys [11-15]. However, this method does not take full advantage of the unique aspects of MPEAs with compositions that explore the center of phase diagrams as opposed to conventional alloys which are represented in the corners and edges. As an alternative, a recent study by Hadraba, et al. of oxide dispersion strengthened (ODS) Cantor alloy has shown

---

[1] Submitted as G. Sahragard-Monfared, M. Zhang, T. M. Smith, A. M. Minor, E. P. George, and J. C. Gibeling. Acta Materialia. (2022)

that it is possible to retain the MPEA matrix with the addition of dispersoids to provide good high temperature strength. Hadraba, et al. fabricated the ODS alloy by adding O_2 gas, Y, and Ti to the blend of Cantor alloy powders during mechanical alloying and subsequently spark plasma sintered the alloyed powders [16]. Recently, Smith, et al. have successfully used laser powder bed fusion (L-PBF) of acoustically mixed yttria coated CrCoNi particles to cost effectively create additively manufactured (AM) ODS CrCoNi [17]. With the advancement of AM as a novel economically viable method for combining the dispersoids and metal matrix, the new feasibility of dispersion strengthening makes it an excellent solution for overcoming the high temperature limitations of FCC MPEAs.

It is well known that processing methods such as vacuum arc melting (VAM), spark plasma sintering (SPS), and AM produce alloys with varying mechanical properties. Yang, et al. investigated processing effects of VAM, SPS, and hot-press sintering on an FeCrNiAl medium entropy alloy and found significant differences in microstructure, mechanical properties, and strengthening mechanisms among the methods [18]. However, the effect of processing methods on tensile creep properties has not been investigated thus far. To address this shortcoming and as a first step toward understanding the matrix properties of potential ODS MPEAs, this study focuses on a comparison of the initial and deformed microstructures, creep properties, and failure mechanisms of wrought and AM CrCoNi.

2.2 Experimental Methods

Wrought CrCoNi was fabricated by arc-melting and drop casting under pure Ar atmosphere. The arc-melted buttons were flipped, remelted five times to promote homogeneity, and drop cast into a copper mold, similar to the process as described for the Cantor alloy by Otto, et al. [19]. After casting, the material was homogenized under vacuum at 1473 K for 24 hours. The material then

underwent a ~95% thickness reduction via cold rolling to a final thickness of 1 mm. The AM CrCoNi was fabricated by L-PBF of pre-alloyed equiatomic CrCoNi powder with a diameter range between 10 - 45 μm, as described by Smith, et al [17]. Two 99.9% dense blanks of AM CrCoNi with a geometry of 88.9 (L) x 15.88 (W) x 15.88 (T) mm were fabricated in a single build and then HIPed at 1458 K to relieve residual stress, remove any defects caused from the AM process, and form a more equiaxed grain structure.

Tensile creep specimens, illustrated in Fig. 2-1, with 35.56 (L) x 2.54(W) x 1.00(T) mm gage dimensions were electrical discharge machined from the cold-rolled wrought sheet and AM builds. The wrought and AM CrCoNi specimens were cut such that the tensile axis (Z-direction) is parallel to the rolling and build directions, respectively. The wrought specimens were annealed in vacuum at 1173 K for 6 hours to achieve an average grain size similar to that of the HIPed AM CrCoNi in order to limit the influence of grain size in this study. Most of the AM specimens were tested in the HIPed condition, but four additional AM specimens were annealed in vacuum at 1173 K for 6 hours to minimize initial dislocation density. All specimens were polished using SiC papers to 600 grit on the surfaces and edges of the gage sections to minimize the risk of surface defects influencing the creep data.
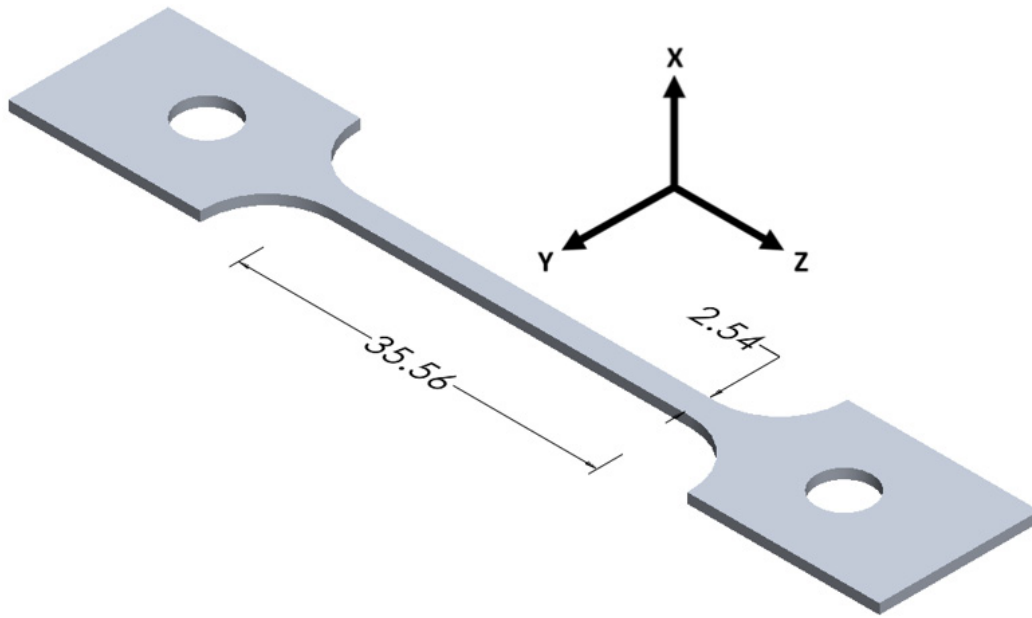
Fig. 2-1 Isometric view of a creep specimen. All dimensions are in mm.

Scanning electron microscopy (SEM) was performed on a Thermo Fisher Quattro S and an FEI Scios Dual Beam FIB/SEM equipped with EDS and EBSD detectors. All microscopy samples were prepared by grinding and polishing to 0.3 μm with an alumina suspension and then vibropolishing with 0.05 μm colloidal silica for 4 hours. The Quattro SEM was used in backscatter electron (BSE) mode to characterize the fractured specimens and grain morphologies. The Scios FIB/SEM was used to characterize the atomic compositions of each material via energy dispersive x-ray spectroscopy (EDS) and the grain orientations and boundary misorientations via electron backscatter diffraction (EBSD). EDS was performed at an operating voltage of 30 kV and EBSD was performed at an operating voltage of 15 kV and step size of 0.8 μm. The EBSD data were post-processed with MTEX (version 5.7.0) in MATLAB following a procedure similar to that used by Broyles, et al. [20] such that unreasonably small grains are removed and unindexed data points are filled based on the orientations of their neighbors. Average grain size was determined from the boundary misorientation maps using the line intercept method and excluding twin boundaries (TB). Crystallite size, as adopted from Schneider, et al. includes both annealing TBs and grain boundaries [21], and was also determined using the line intercept method on the boundary misorientation maps.

TEM samples in the YZ plane were prepared by grinding and polishing the specimen gage surface to 1200 grit and less than 100 μm thickness. The TEM samples were then twin jet polished using a Fischione Model 110 Automatic Twin-Jet Electropolisher with a 70% methanol, 20% glycerol, and 10% perchloric acid solution. The dislocation structure of the crept specimens was studied by both TEM performed on a JOEL 3010 TEM at an accelerating voltage of 300kV and diffraction contrast imaging scanning TEM (DCI-STEM) conducted on an FEI Tecnai

S/TEM at an accelerating voltage of 200 kV. Scanning TEM EDS (STEM-EDS) was performed on an FEI TitanX to identify the composition of particles in the AM CrCoNi.

Constant stress tensile creep tests were performed under vacuum (≤ 3 x 10^{-5} torr) to avoid oxidation, following the procedures described by Decker, et al. [22]. Tests were performed in the ranges of 1023-1173 K and 40-200 MPa and were conducted until fracture to ensure each specimen reached steady state creep. Two sets of interrupted tests were also performed for each material. One set of tests was terminated once steady state had been achieved, and furnace cooled with the specimen under load to preserve the dislocation structure for transmission electron microscopy (TEM). The other set of interrupted tests was terminated at 4% strain for each material to compare the extent of cracking in the two materials prior to fracture.

2.3 Results and Discussion

2.3.1 Characterization of Initial Microstructure

Wrought and AM MPEAs have been observed to have a uniform distribution of elements, however, verification of an evenly distributed matrix of elements in both materials is critical to this comparative study [23, 24]. Hence, the initial chemical composition of both materials was determined by SEM-EDS as shown in Fig. 2-2, where they were both observed to be equiatomic with a uniform distribution of the three principal elements. The EBSD images and inverse pole figure (IPF) contour plots displayed in Fig. 2-3 illustrate that there is minimal texture in both materials. The IPF contour plot shown for the AM material was generated from the EBSD map of the YZ plane and is also representative of the IPF contour plot of the EBSD map of the XY plane. It is also observed that both materials have a significant number of annealing twins, which is typical for this material [25, 26].

(a)

Cr

Co

Ni

Element	Atomic %
Cr	33.30
Co	33.24
Ni	33.45

100μm

(b)

Cr

Co

Ni

Element	Atomic %
Cr	34.10
Co	33.33
Ni	32.60

100μm
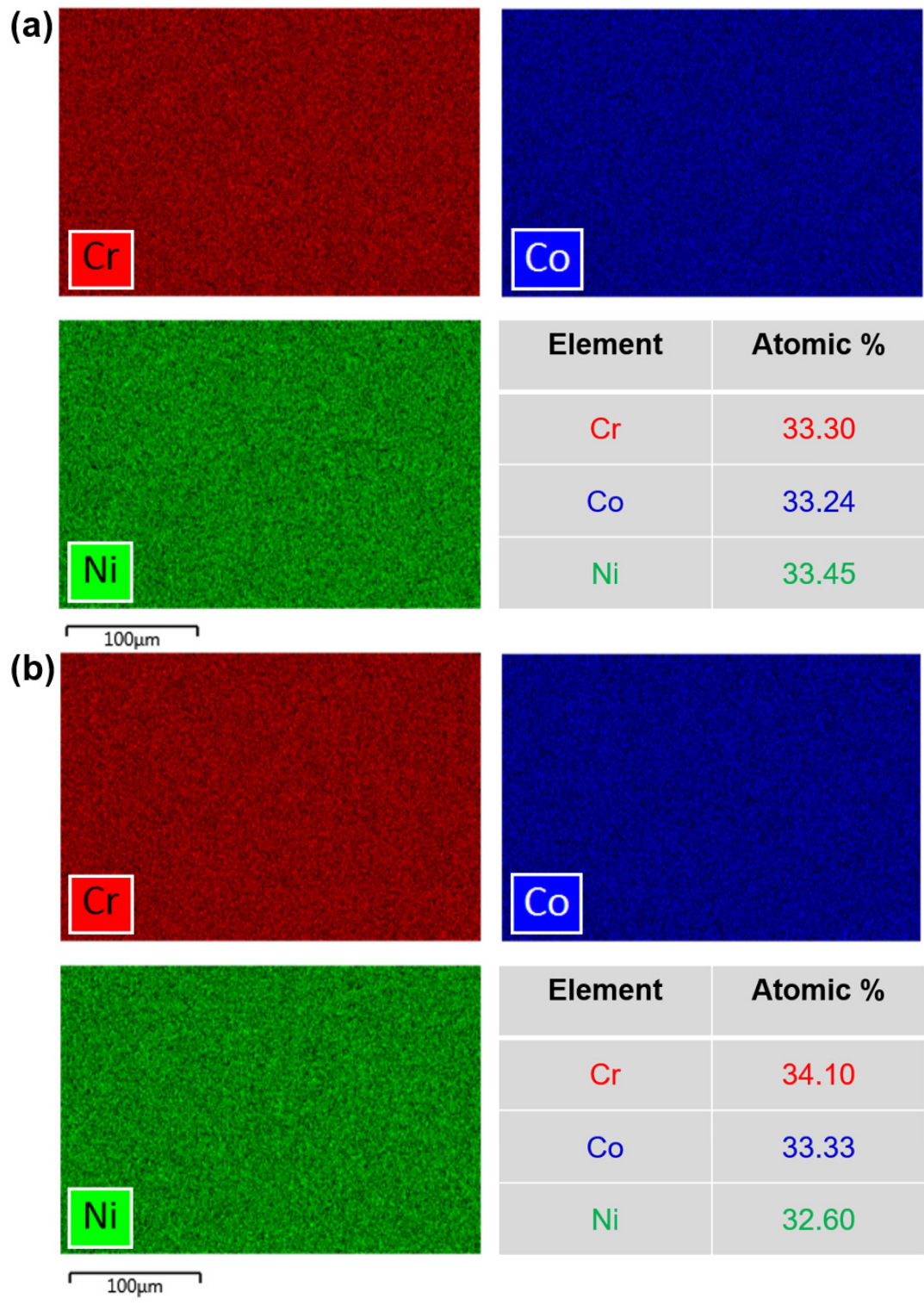
Fig. 2-2 SEM-EDS maps of (a) wrought CrCoNi (b) AM CrCoNi, and their corresponding atomic percentages.
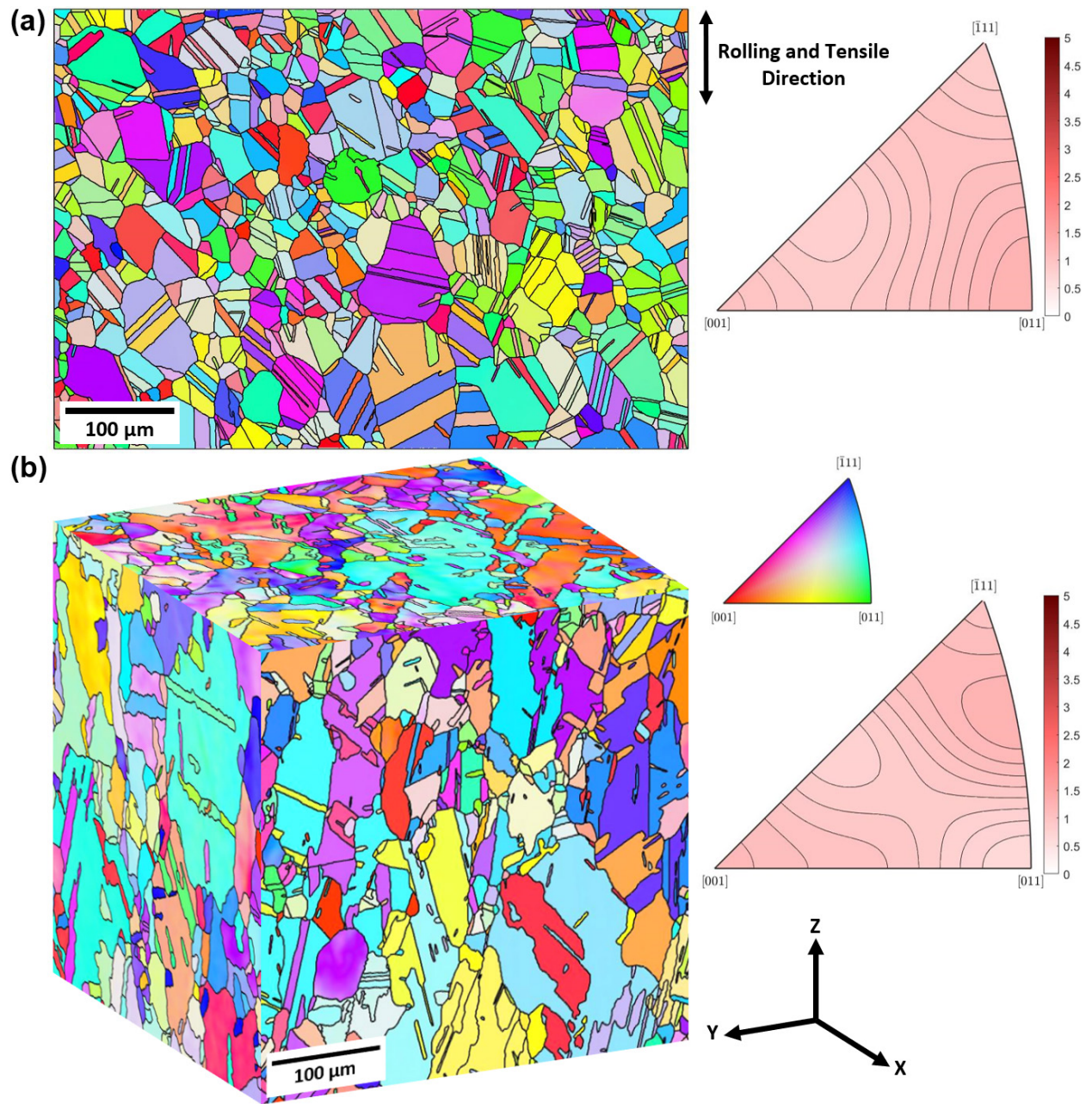
Fig. 2-3 EBSD-IPF color maps and IPF contour plots of (a) wrought CrCoNi (b) AM CrCoNi.

Fig. 2-4 shows the boundary misorientation plots of wrought CrCoNi, XY AM CrCoNi, and YZ AM CrCoNi from which grain sizes and crystallite sizes were determined. The grains in the wrought CrCoNi are equiaxed with a grain size of 31.2 ± 1.9 μm and a crystallite size of 13.8 ± 2.1 μm. The AM CrCoNi grains are slightly elongated in the build direction with an irregular shape and aspect ratio of approximately 1.8:1 such that the grain size is 74.3 ± 2.6 μm in the Z-direction of the YZ plane and 41.4 ± 2.4 μm in the Y-direction of the YZ plane; the corresponding crystallite sizes are 22.0 ± 2.2 μm and 13.7 ± 2.1 μm. As noted by Smith, et al., the HIP cycle has allowed the grains in the AM CrCoNi to partially recrystallize and become more equiaxed, although the grain structure still retains features typical of AM grain morphologies [17]. Fig. 2-4(c) illustrates the smaller number of low angle grain boundaries (LAGB, colored blue) in the YZ plane of the AM material compared to the wrought material. TBs, high angle grain boundaries (HAGB), and LAGB are quantified in Table 2-1 for both materials. These boundaries are defined with misorientation angles of 60 ± 3° (TBs), greater than 15° excluding TBs (HAGBs), and 1 – 15° (LAGBs). Histograms of misorientation angles for both materials are shown in Fig. 2-5.
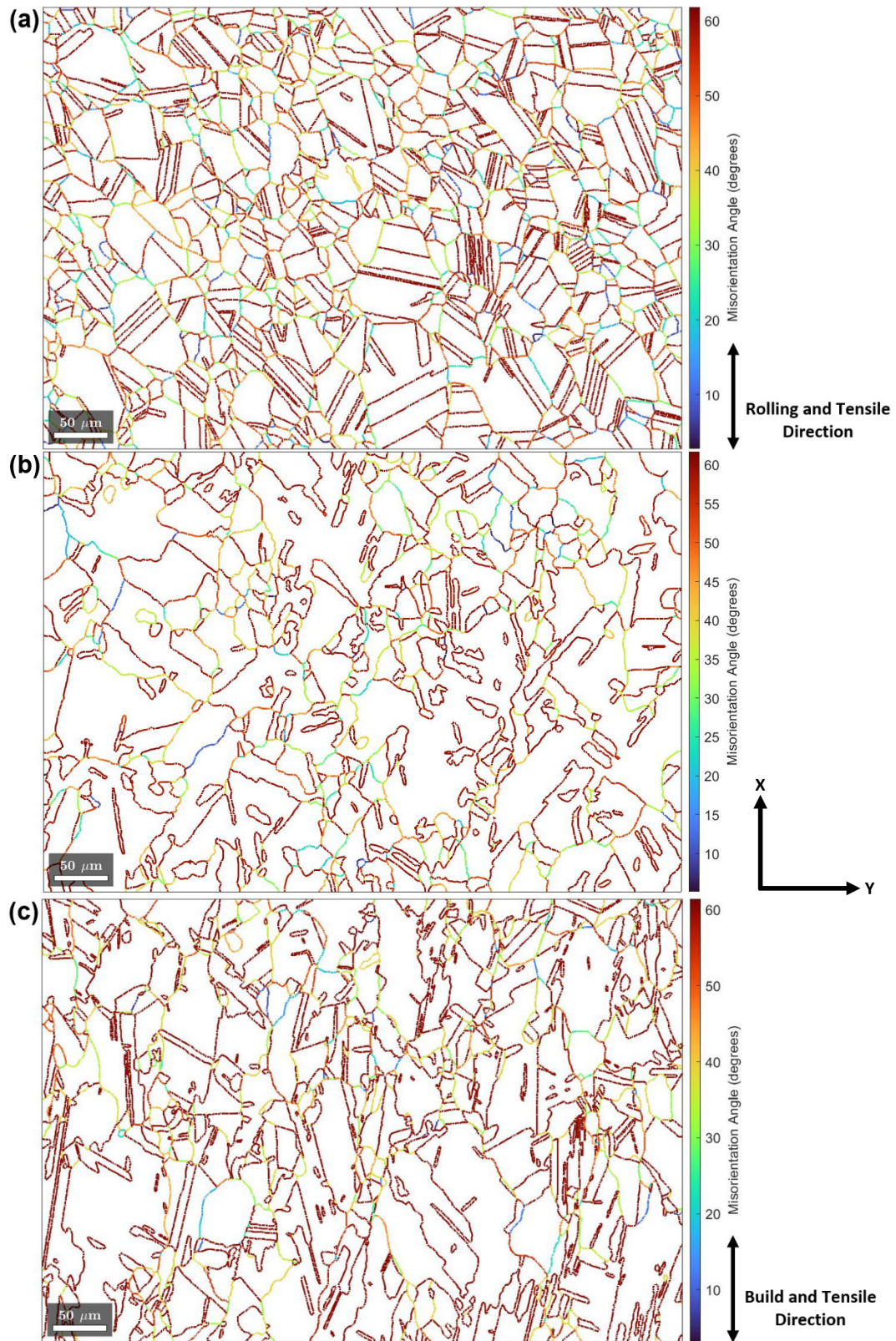
Fig. 2-4 Boundary misorientation plots of (a) wrought CrCoNi (b) XY plane of AM CrCoNi (c) YZ plane of AM CrCoNi.
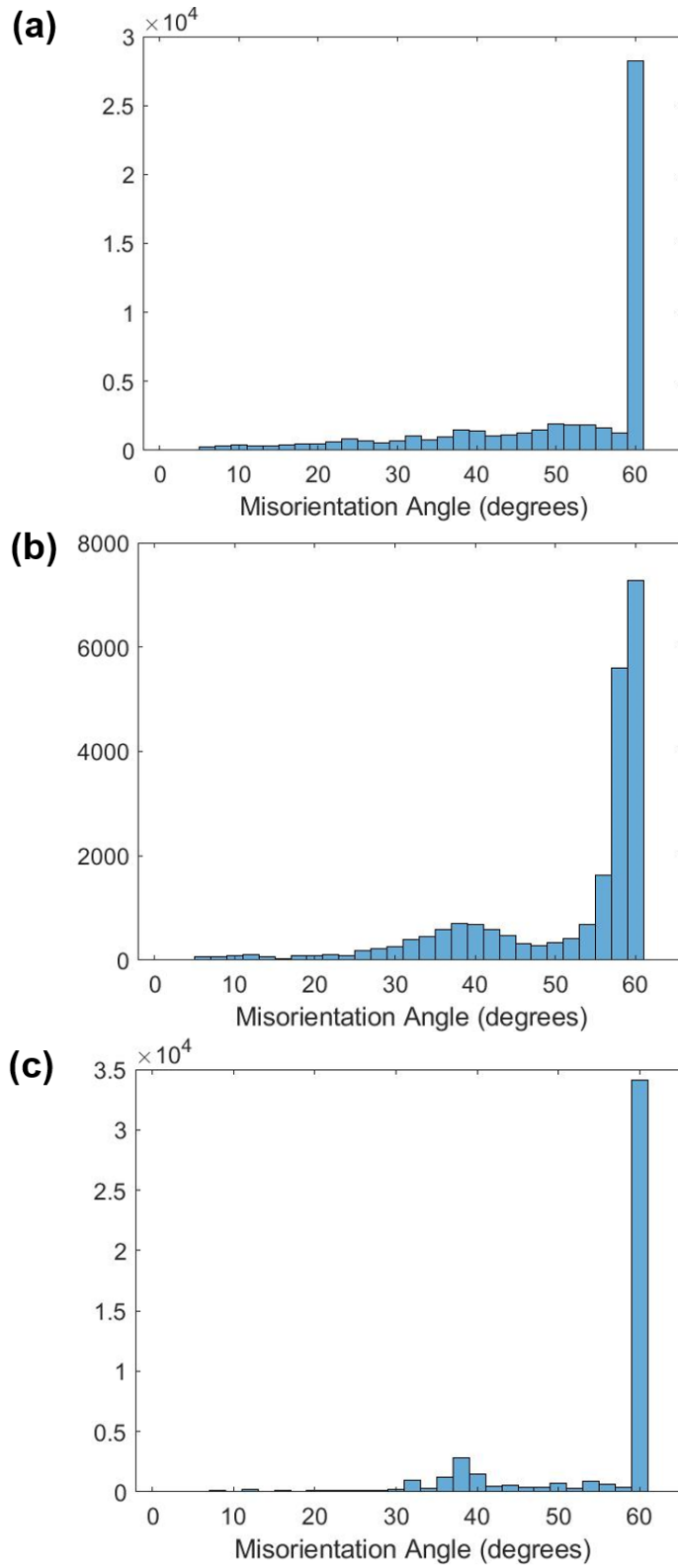
Fig. 2-5 Histograms of misorientation angle for (a) wrought CrCoNi (b) plane normal to Z-direction in AM CrCoNi, and (c) plane normal to X-direction in AM CrCoNi.

Table 2-1 Percentages of low angle grain boundaries, high angle grain boundaries, and twin boundaries.

Material	LAGB	HAGB	TB
Wrought CrCoNi	3.2%	41.9%	54.9%
AM CrCoNi (XY)	1.8%	39.4%	58.8%
AM CrCoNi (YZ)	0.9%	25.8%	73.3%

2.3.2 Creep Results

Representative creep curves illustrating the effect of variations in temperature and applied stress are presented in Fig. 2-6. Both materials display creep behavior typical of pure metals and alloys that behave like pure metals with distinct normal primary, secondary, and tertiary regions. The power law equation (Eq. (2.1)) describes the relationship between steady state creep rate, $\dot{\varepsilon}_{SS}$, and applied stress, σ, where A is a material constant that includes dislocation structure, Q_C represents the creep activation energy, R is the gas constant, and T is temperature [27].
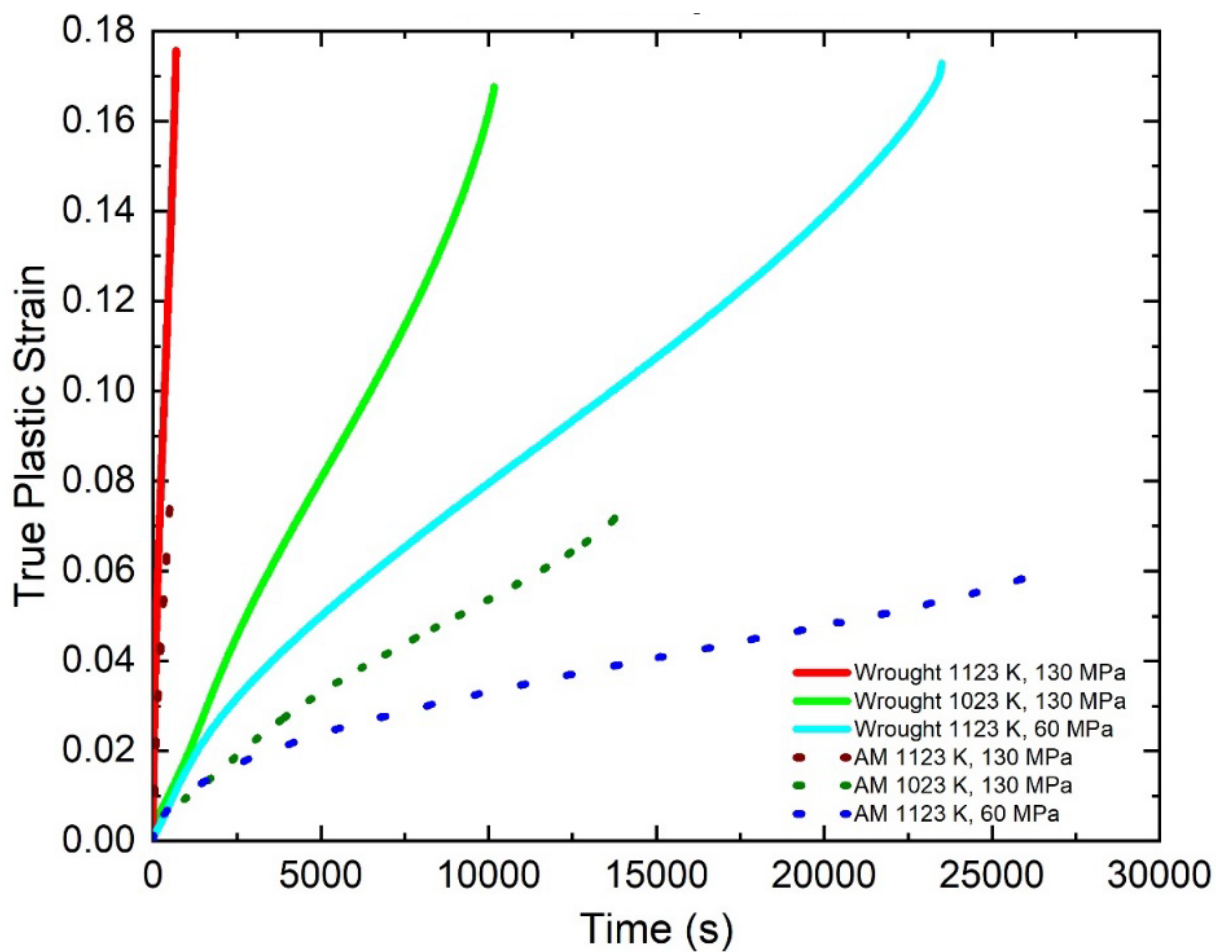
Fig. 2-6 Representative creep curves of wrought and AM CrCoNi.

$$\dot{\varepsilon}_{SS} = A\sigma^n \exp\left(-\frac{Q_C}{RT}\right) \tag{2.1}$$

Steady-state creep rates were obtained by determining the slopes of the secondary region of the creep curves and plotted as a function of applied stress to determine the stress exponents for each material; this relationship is shown on double logarithmic plots in Fig. 2-7. Stress exponents of 4.5 ± 0.2 and 5.9 ± 0.1 were found for wrought and AM CrCoNi, respectively. These values are generally in the range commonly associated with the dislocation climb mechanism of creep deformation in subgrain forming metals. By comparing the two plots in Fig. 2-7, it is clear that AM CrCoNi exhibits a lower steady state creep rate than the wrought material for all but the two most extreme combinations of temperature and stress, both of which are at an applied stress of 200MPa. To put these results in the context of creep of a high entropy alloy, Fig. 2-8 provides a comparison of the steady-state creep rates and applied stresses for wrought and AM CrCoNi along with data for the wrought Cantor alloy reported by Zhang, et al. at a single temperature of 1023 K [10]. These data illustrate that AM CrCoNi has better creep resistance than wrought, and both have better creep resistance than the wrought Cantor alloy. The stress exponents of the CrCoNi are also higher than those found in the Cantor alloy when tested under similar conditions, implying different rate-controlling creep deformation mechanisms.
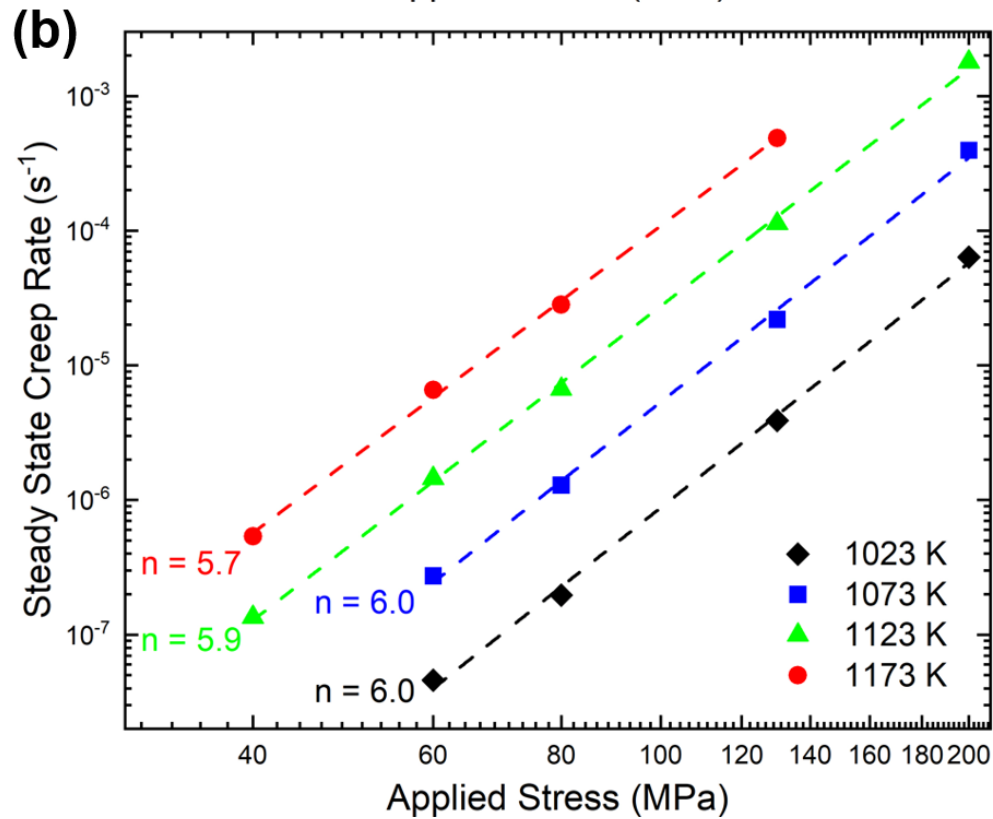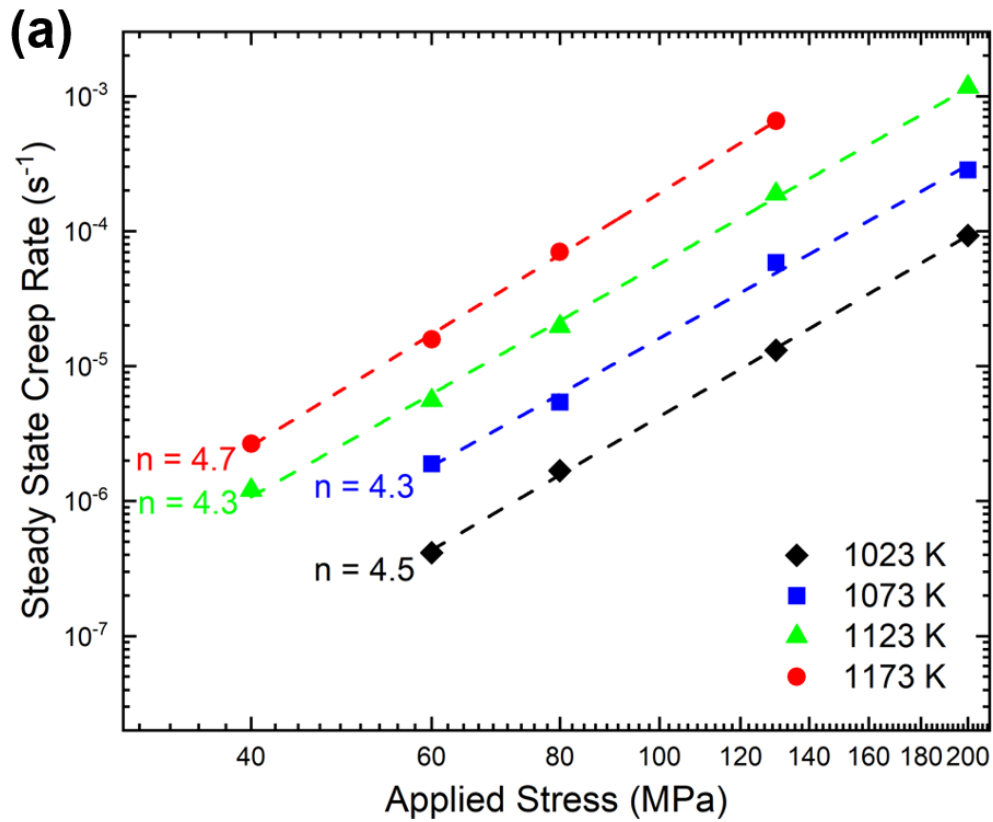
Fig. 2-7 Log-log plots of steady state creep rate vs applied stress for (a) wrought CrCoNi and (b) AM CrCoNi.
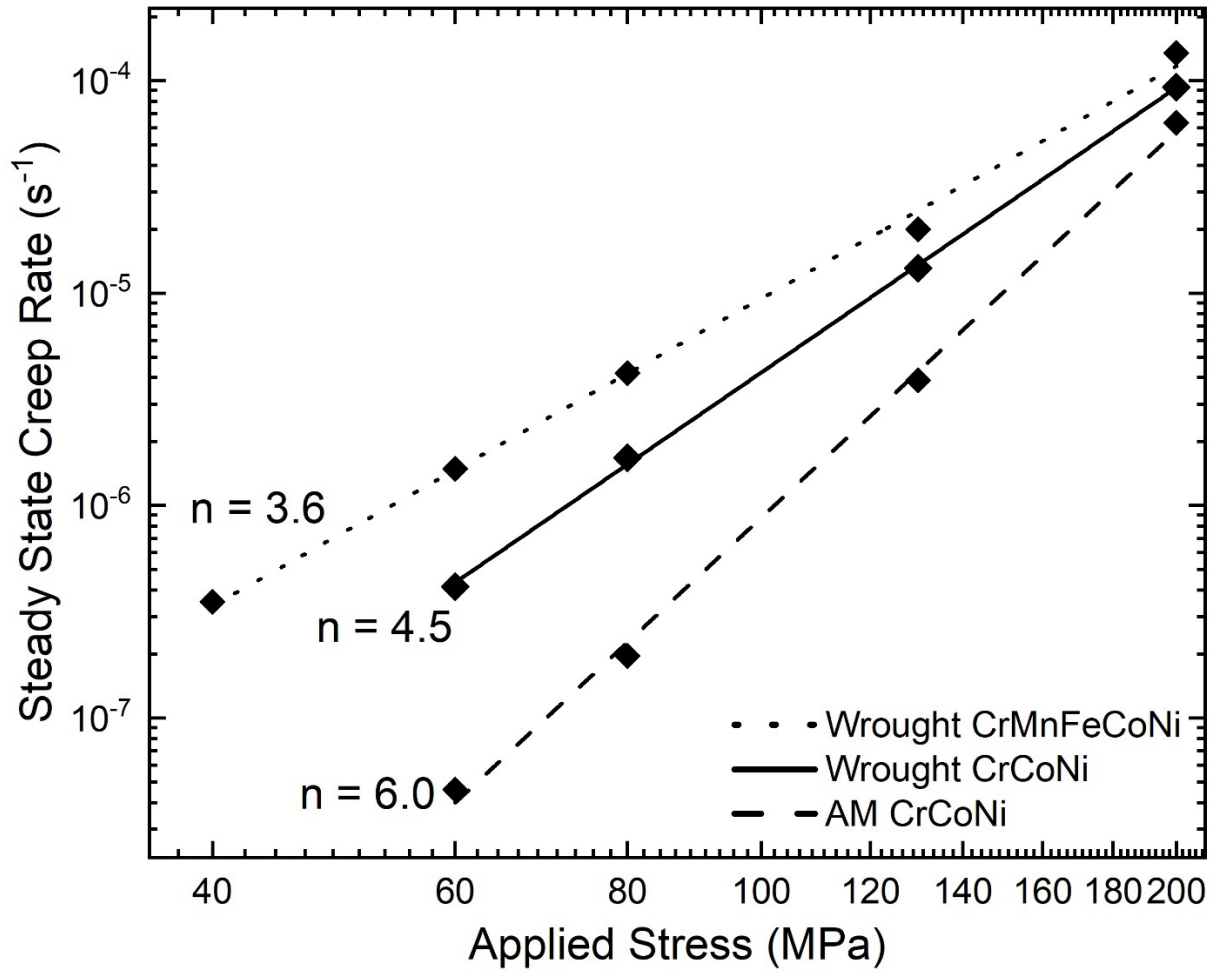
Fig. 2-8 Log-log plot of steady state creep rate vs applied stress for wrought Cantor alloy, wrought CrCoNi, and AM CrCoNi at 1023 K.

The activation energies of both materials were determined from a semi-log plot of steady state creep rate vs 1/T as shown in Fig. 2-9. The activation energies range from 240-259 kJ/mol for wrought and 320-331 kJ/mol for AM CrCoNi reflecting the better creep resistance of the AM material. While the activation energy for creep in the AM material agrees favorably with the reported self-diffusion activation energy of 330 kJ/mol, that is not the case for the wrought material which has a significantly lower activation energy [28]. The activation energy values of both CrCoNi materials exceed the activation energy range of the Cantor alloy, 219-236 kJ/mol, again reflecting their better creep resistance [10].

Schneider, et al. reported that TBs contribute to boundary strengthening in low stacking fault energy alloys, such as CrCoNi, on the same scale as GBs [26]. Sun, et al. also found that TBs act as strong barriers to dislocation motion and hence play a key role in enhancing the creep resistance of CrCoNi [29]. In contrast, for a LAGB, the orientation of grains on each side of the boundary is similar allowing a smaller dislocation pile-up stress concentration in the primary grain to propagate deformation into the secondary grain [30, 31]. Since the wrought material has more than twice as many LAGBs than the AM material, one reason for the difference in creep rates at a given stress and temperature is that lower stresses are required to propagate dislocation motion in the wrought material, contributing to its higher steady state creep rate than AM CrCoNi. Furthermore, as the stress increases, higher density barriers such as TBs are overcome, reducing the difference between AM and wrought leading to a convergence of the data.
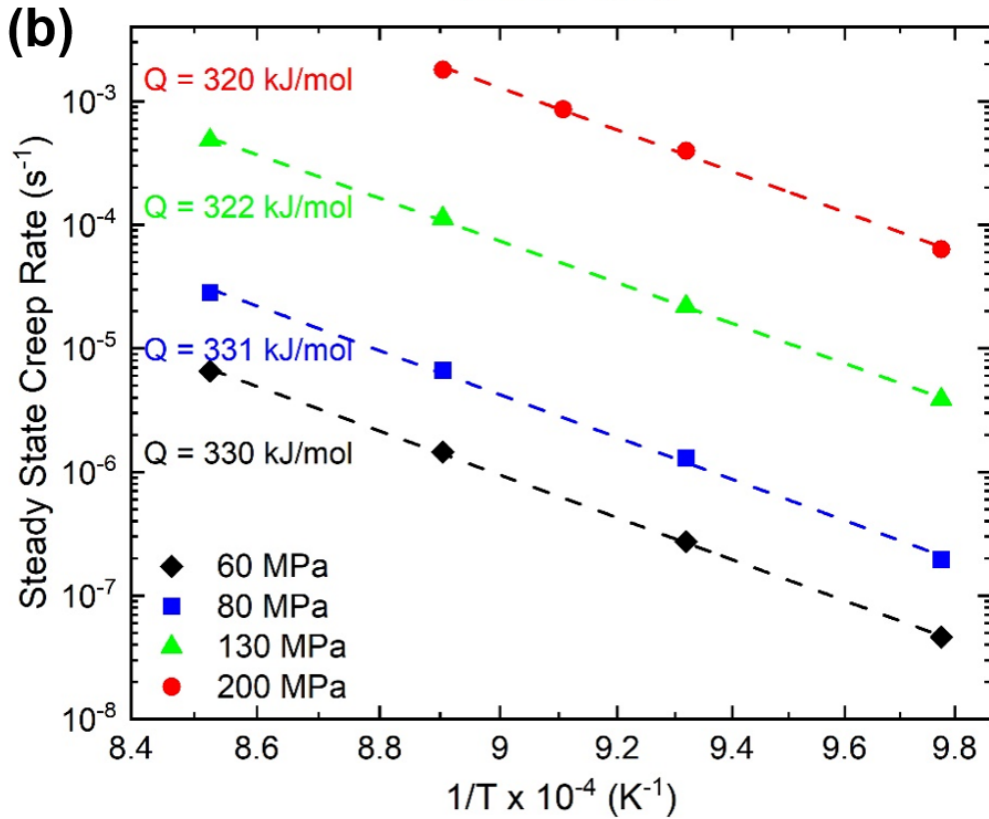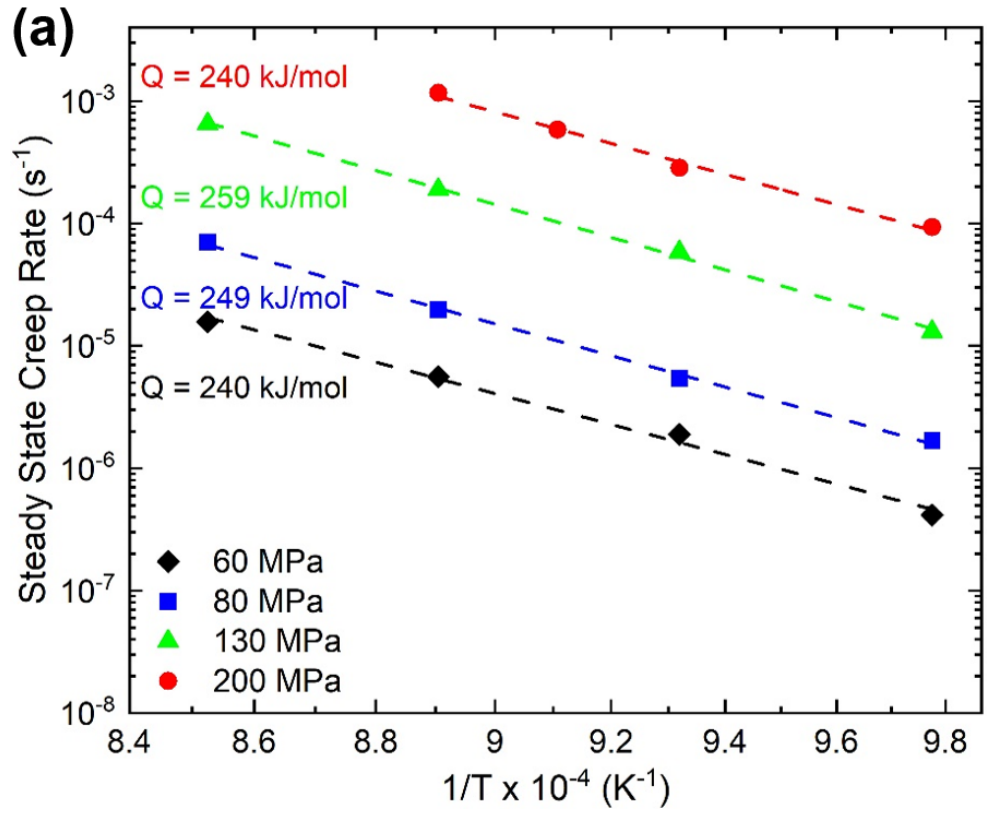
Fig. 2-9 Semi-log plot of steady state creep rate vs 1/T for (a) wrought CrCoNi and (b) AM CrCoNi.

2.3.3 Dislocation Structures of Wrought and AM CrCoNi

In order to understand the possible microstructural origins of the difference in creep behaviors of wrought and AM CrCoNi, the dislocation structures of the undeformed materials are presented in Figs. 2-10 and 2-11. The undeformed wrought material shown in Fig. 2-10(a) exhibits a very low dislocation density as a result of the prior annealing (recrystallization) process. During the recovery stage of annealing, dislocation/dislocation annihilation and dislocation absorption at grain boundaries leads to a decreased dislocation density, which is then further reduced as the stored mechanical energy drives recrystallization and new dislocation-free grains consume the deformed grains. A twin boundary is also observed in Fig. 2-10(a). In contrast, one region of the dislocation structure of the undeformed AM material (Fig. 2-10(b)) reveals a high dislocation density as well as (111) slip traces and stacking faults. These dislocations are generated during the layer-by-layer build process of AM because of differential thermal expansion/contraction during heating and cooling of adjacent layers. Another region of the uncrept dislocation structure of the AM material (Fig. 2-11) shows a dislocation network, stacking fault tetrahedra (SFT), and extended nodes. SFT were first observed by Silcox and Hirsch in quenched gold and commonly originate from the collapse of vacancies clusters [32]. The SFT in the AM material likely formed due to the fast cooling rate of L-PBF which is similar to a quenching process. Particles are also observed in Figs. 2-10(b) and 2-11 and are discussed in further detail in the next section. Although both the wrought and AM materials were thermally processed at similar temperatures, the additional pressure of the HIPing process on the AM material does not allow for recovery of the dislocation structure.
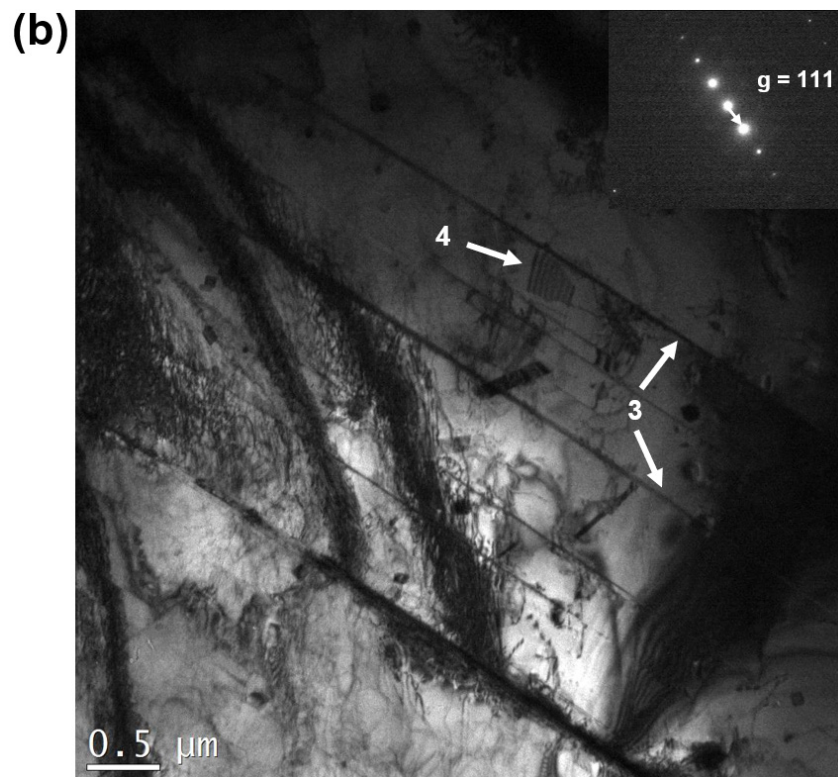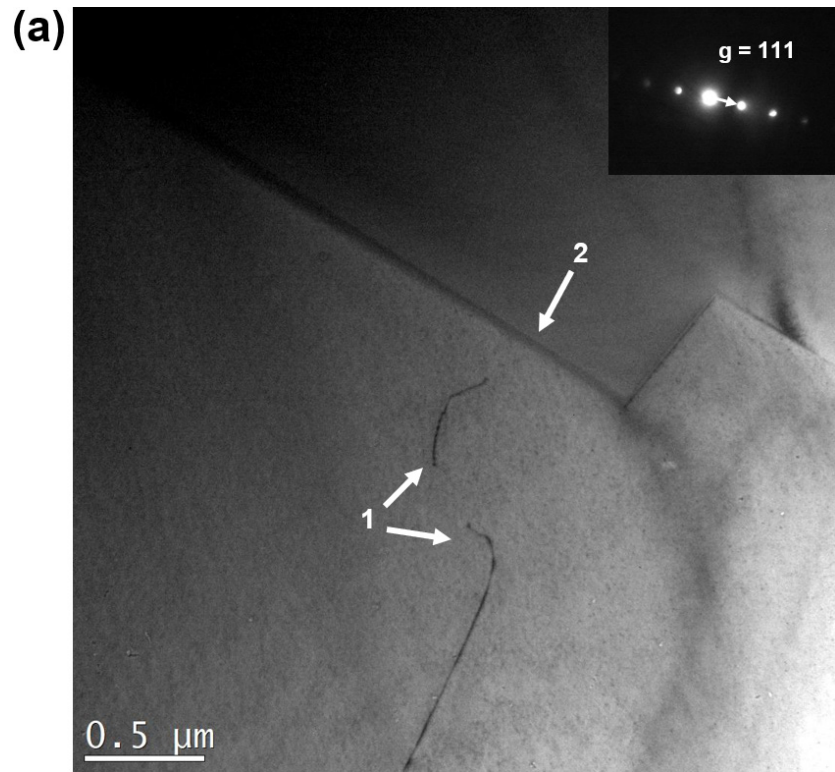
Fig. 2-10 Dislocation structure prior to creep testing of (a) wrought CrCoNi showing two dislocations (arrows 1) and a twin boundary (arrow 2) and (b) AM CrCoNi showing a high dislocation density, (111) slip traces (arrows 3), and stacking faults (arrow 4).
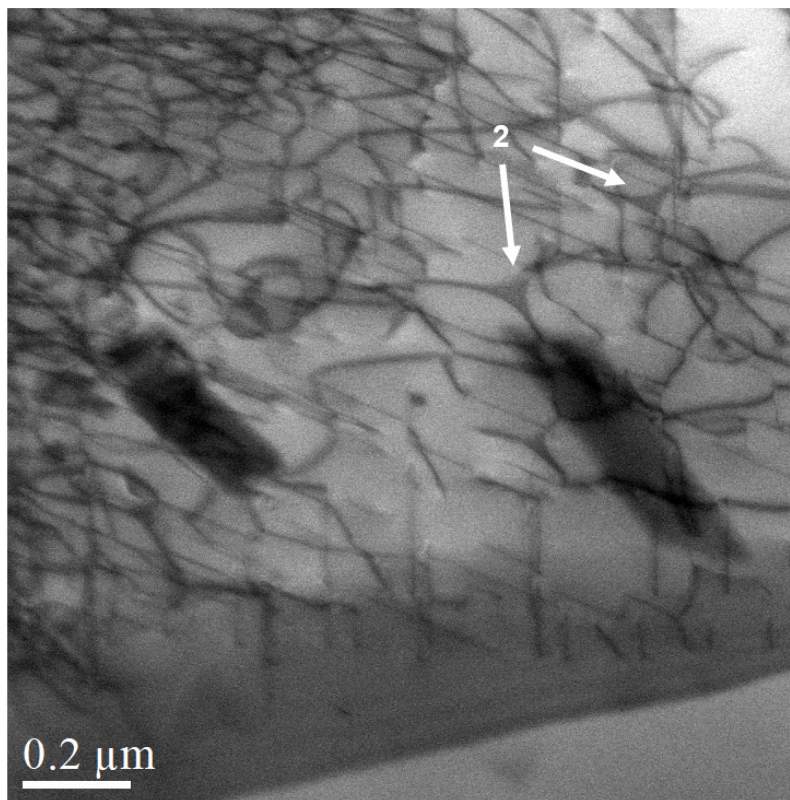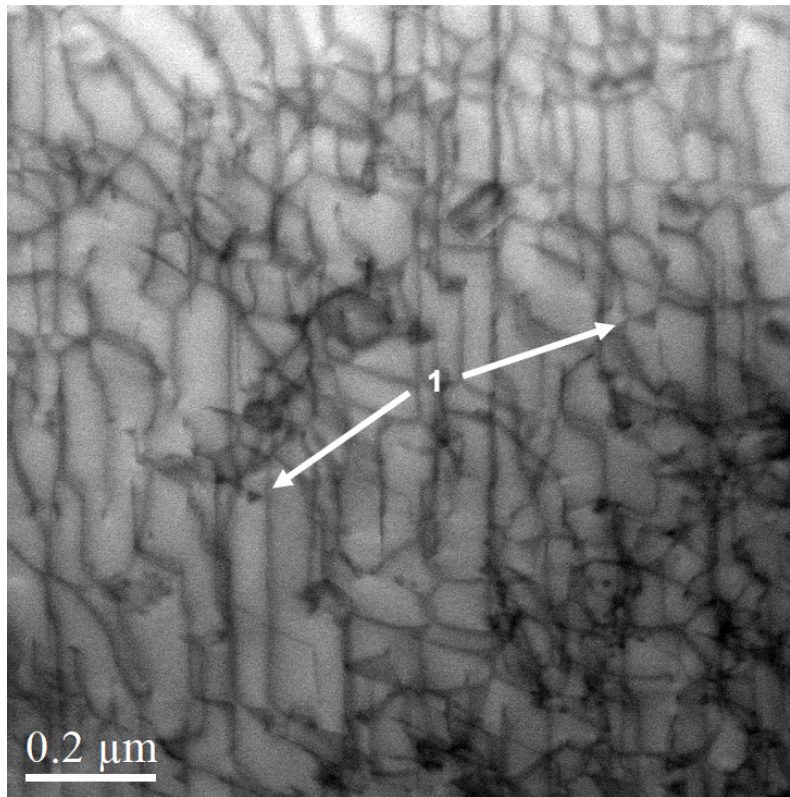
Fig. 2-11 DCI-STEM images of the dislocation structure of uncrept AM CrCoNi showing a dislocation network, stacking fault tetrahedra (arrows 1), and extended nodes (arrows 2).

It is well known that in pure polycrystalline FCC metals the transition from primary to secondary creep is caused by a decrease in mobile dislocation density typically associated with the formation of subgrain boundaries [33]. However, as seen in Figs. 2-12 to 2-14, which show the dislocation structures of both materials crept to steady state, subgrain formation was not observed in either material. Instead, the individual dislocations are broadly curved and form dislocation multijunctions and jogs. Multijuctions are associated with dislocation bowing from forest dislocation interactions and particles in the AM material. These arrangements are similar to the dislocation structures observed in the Cantor alloy crept to steady state [10]. Slip bands blocked by boundaries are observed in Figs. 2-12 and 2-14; these slip bands were not observed in the Cantor alloy. Additionally, these blocked slip bands occur more frequently in the AM material. As seen in Fig. 2-12, there are two sets of diffraction spots visible indicating that this is a twin boundary. Also, unlike the Cantor alloy, the dislocation structures of CrCoNi are not consistent with the room and cryogenic temperature dislocation structures. The dislocation structure of wrought CrCoNi deformed at room and cryogenic temperatures is characterized by the glide of dislocations dissociated into Shockley partials with stacking faults in between, and nanotwinning [34]. Some dislocations dissociated into Shockley partials connected by stacking faults are observed in Fig. 2-14, but these are much fewer in number than in the typical dislocation structures observed following room and cryogenic temperature deformation. Nanotwins are not expected to form at the relatively low stresses involved in creep tests, and indeed none were observed [35].
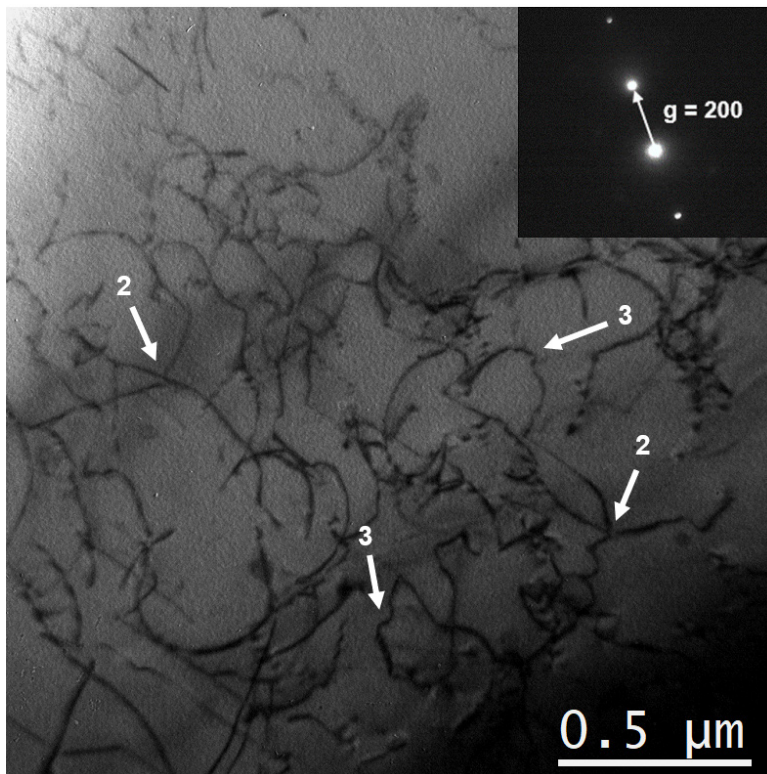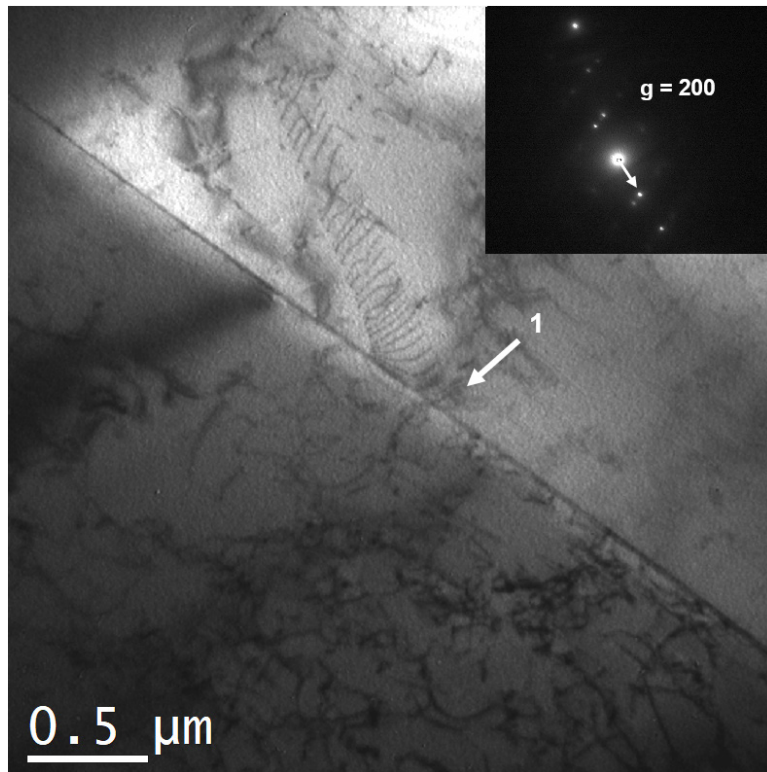
Fig. 2-12 TEM images of dislocation structures in wrought CrCoNi crept to steady state at 1023 K and 80 MPa showing a slip band blocked by a grain boundary (arrow 1), multijunctions (arrows 2), and jogs (arrows 3).
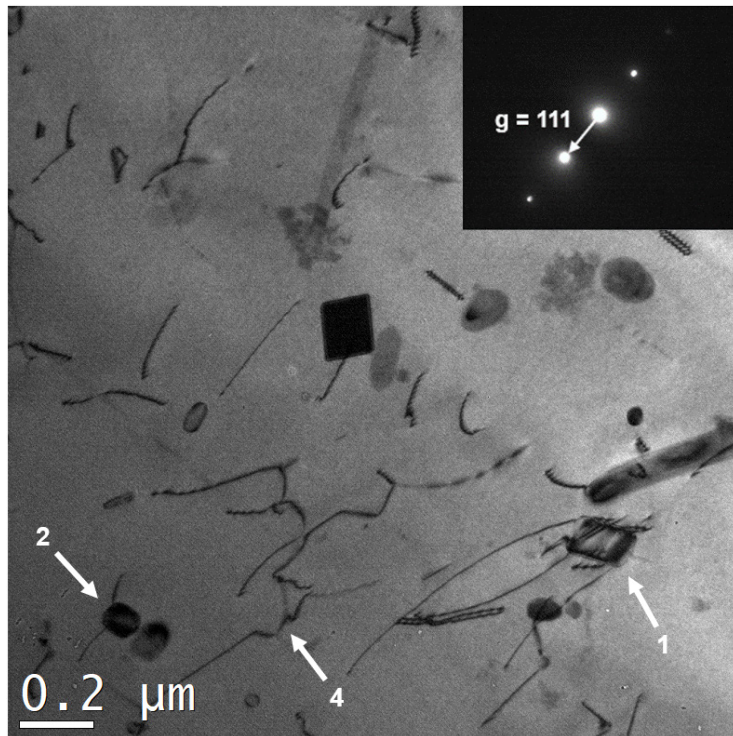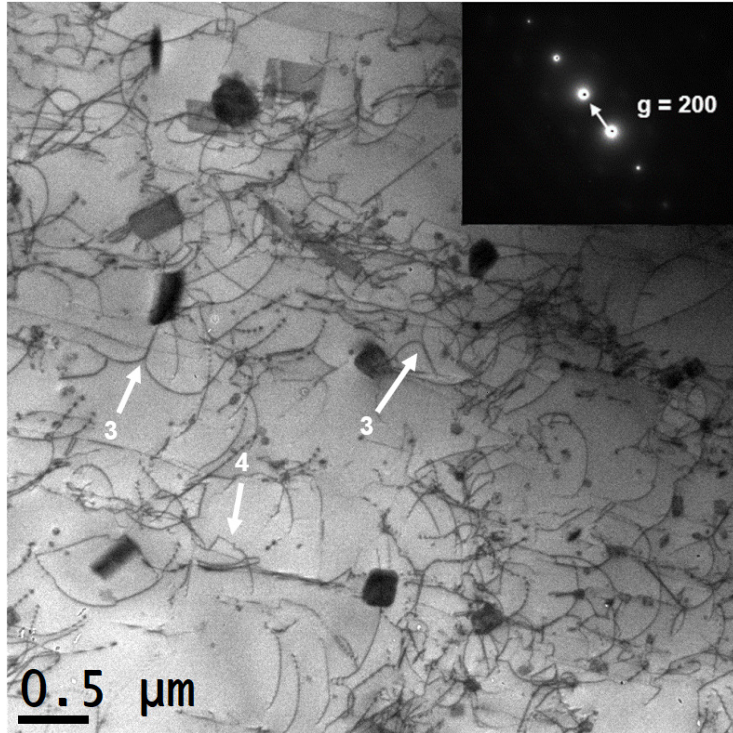
Fig. 2-13 TEM images of the dislocation structure in AM CrCoNi crept to steady state at 1023 K and 80 MPa, showing dislocation nucleation at an incoherent Cr_2O_3/CrCoNi matrix interface (arrow 1), dislocation interactions with oxides such as detachment (arrow 2), multijunctions (arrows 3), and jogs (arrows 4).
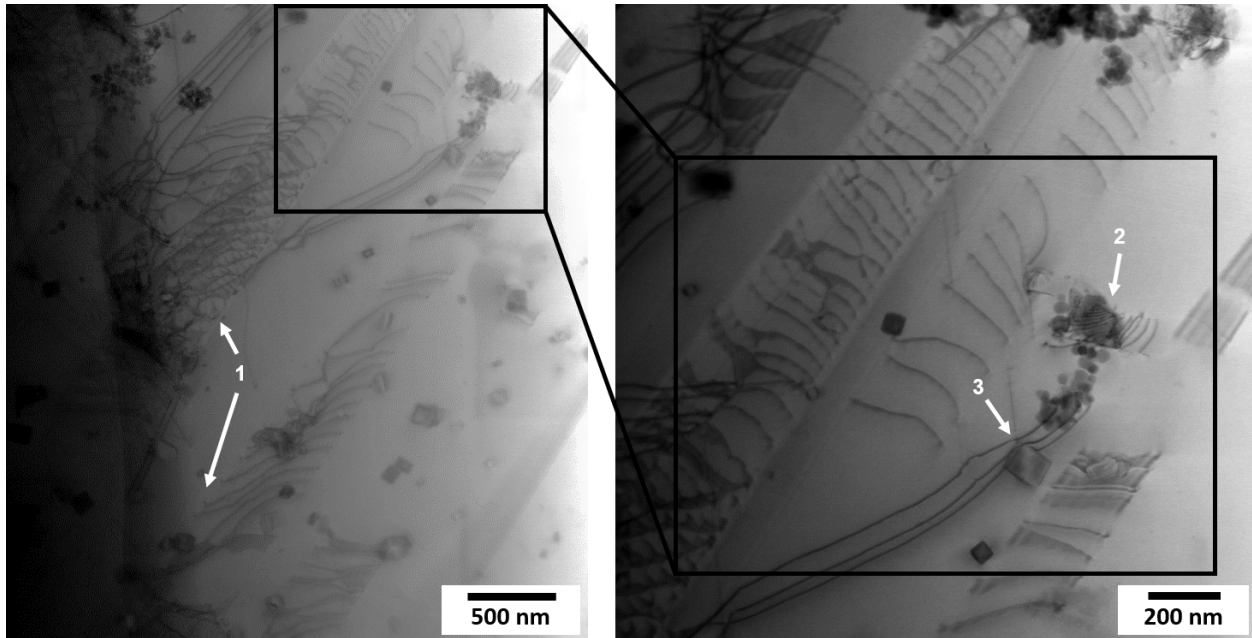
Fig. 2-14 DCI-STEM images of the dislocation structure in AM CrCoNi crept to steady state at 1023 K and 80 MPa, showing slip bands blocked by a grain boundary (arrows 1), dislocation generation at an incoherent Cr_2O_3/CrCoNi matrix interface (arrow 2), and dislocation interactions with oxides such as bowing (arrow 3).

2.3.4 Particle Characterization in AM CrCoNi

Figs. 2-10(b), 2-13, and 2-14 reveal that spherical and cuboidal particles are present in the AM

CrCoNi. STEM-EDS of the particles, as shown in Fig. 2-15, indicates that these particles are Cr-

rich oxides which have also been observed in wrought CrCoNi by other authors [36, 37]. There

are three distinct oxides in the AM material which are shown in Fig. 2-15. These oxides are

classified as bright cuboidal, dark cuboidal, and dark spherical based on their physical

appearance. The compositions of these oxides are reported in Fig. 2-15 and reveal that the bright

cuboidal oxides are Cr_2O_3 while the other two are Cr-rich complex oxides. As observed

qualitatively in the TEM images (Figs. 2-10 to 2-14), the fraction of Cr-rich oxides in AM

CrCoNi is much higher than in the wrought material, likely due to the AM processing. It has

been speculated that oxygen take-up occurs during laser melting because of the presence of

oxygen in the chamber [38]. The total area fraction of Cr-rich oxides in the AM material was

found to be 4% as determined by area measurements of 140+ particles over a total area of 74

μm^2 using ImageJ. Assuming a uniform distribution of particles, the oxide volume fraction is

calculated to be 0.6%. These incidental Cr-rich oxides are another possible contributor to the

superior creep resistance in the AM CrCoNi compared to wrought. Fig. 2-13 illustrates that

dislocations tend to cluster near the oxides even though subgrains do not form. Individual

dislocations can also be seen interacting with particles in Figs. 2-13 and 2-14, both piling up at

them and apparently detaching from them as in the Rösler-Arzt model. These processes are

characteristic of the rate-controlling processes in dispersion strengthened metals [39-42]. In

addition, the Cr_2O_3/CrCoNi matrix interface is incoherent and serves as a source of dislocations,

as observed in Figs. 2-13 and 2-14, which is also observed in conventional ODS alloys [43]. The

dislocation/oxide interactions are not widespread and thus likely are not the primary rate-

controlling mechanism in the AM material. However, the oxides limit the glide distance of mobile dislocations after overcoming an obstacle and thus contribute to the lower steady state creep rates of the AM alloy. Additionally, these interactions may still inhibit creep deformation and thereby increase creep resistance in the AM CrCoNi, despite the composition of the present alloy not being designed to include strengthening particles.

Bright Cuboidal		Dark Cuboidal		Dark Spherical	
Element	Atomic %	Element	Atomic %	Element	Atomic %
Cr	37.62	Cr	40.24	Cr	39.21
O	59.26	O	32.42	O	9.84
Co	1.88	Co	13.82	Co	25.86
Ni	1.24	Ni	13.52	Ni	25.10
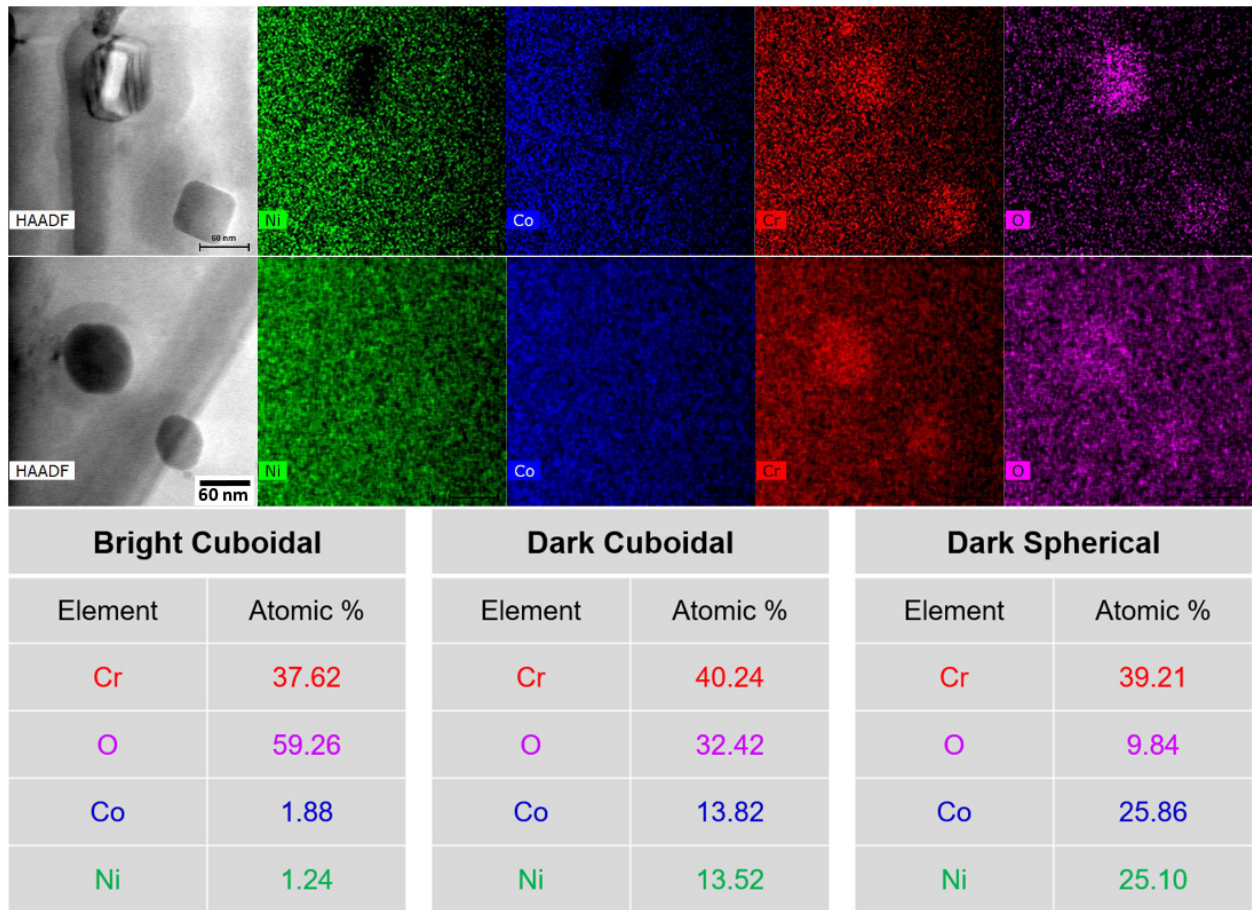
Fig. 2-15 STEM-EDS of Cr-rich oxides in AM CrCoNi and their corresponding atomic percentage.

2.3.5 Fracture Characteristics After Creep in Wrought and AM CrCoNi

The average creep ductilities of wrought and AM CrCoNi were $17.6 \pm 1.6\%$ and $7.1 \pm 1.2\%$, respectively. The lower creep ductility of the AM material stems from the higher volume fraction of oxides acting as cavity nucleation sites, the lower percentage of LAGBs which enable easy propagation of deformation across grains, and the higher percentage of TBs which do not act as dislocation sources, thereby reducing the possibility of slip transmission on the other side of the boundary. It is well known that, during creep deformation, stress concentrations on GB triple points due to GB sliding, dislocation pile-ups against GBs (Zener-Stroh mechanism), as well as hard particles on GBs lead to the nucleation of voids which coalesce and result in intergranular fracture [44-48]. As demonstrated by Dyson, creep ductility decreases as the rate of cavity production increases [49]. The fracture surfaces of wrought and AM CrCoNi in Fig. 2-16 illustrate that the higher volume fraction of oxides in the AM material causes numerous small cavities to nucleate around these oxides which then coalesce leading to fracture of the AM material at a lower ductility than the wrought material. Additionally, the lower percentage of LAGBs in the AM material causes the Zener-Stroh mechanism to be more prevalent than in the wrought material. Since dislocation pile-ups are more likely to propagate through LAGBs, Zener-Stroh induced cavities are less likely to nucleate in the wrought material. However, since the percentage of LAGBs in the YZ plane is 0.9% in the AM material and 3.2% in the wrought material, the oxides in the AM material likely have a larger contribution to its lower ductility than the Zener-Stroh mechanism.
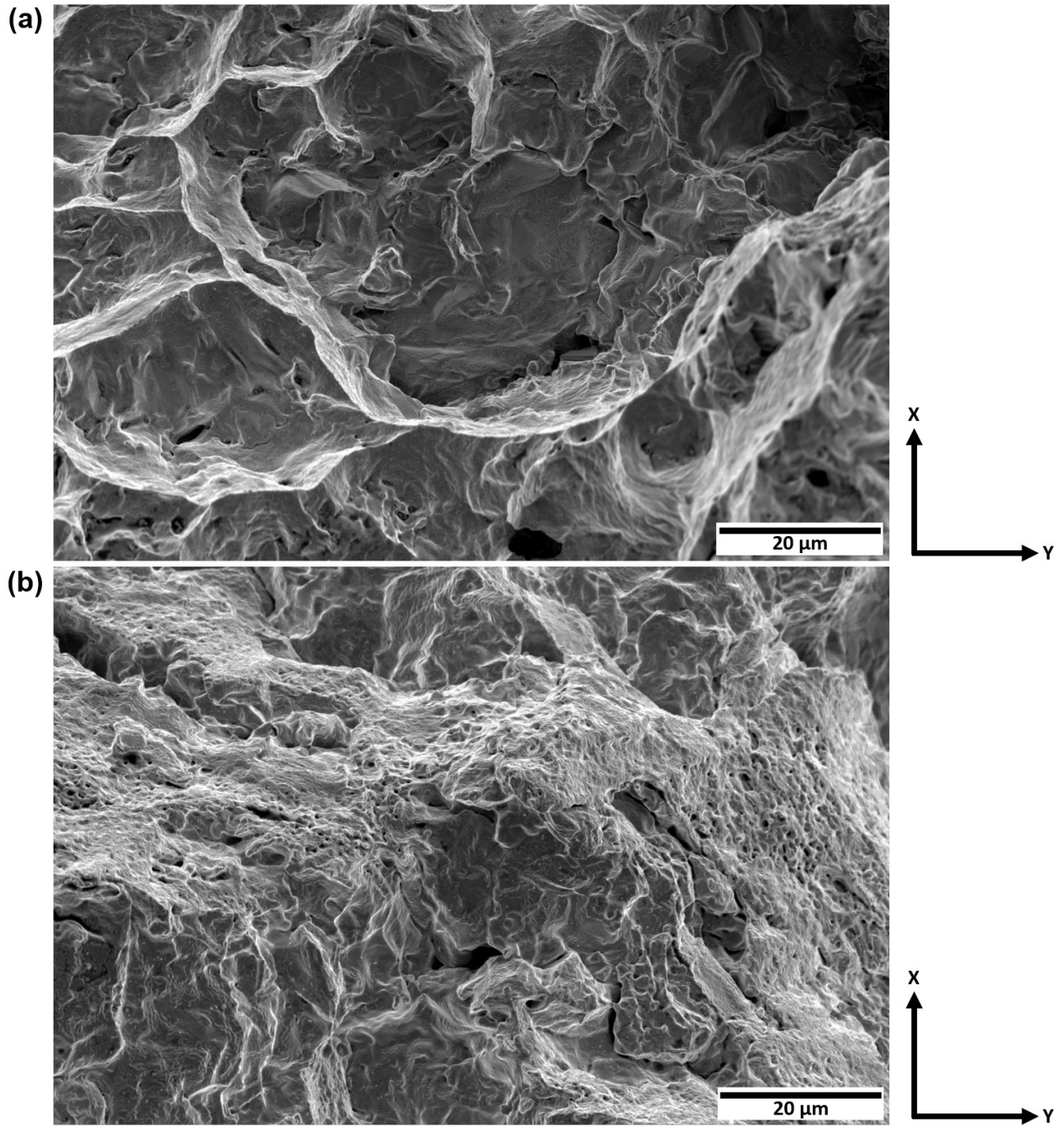
Fig. 2-16 Fracture surfaces of (a) wrought CrCoNi and (b) AM CrCoNi following creep rupture at 1023 K and 130 MPa.

Fig. 2-17 shows the surfaces of fractured specimens of both materials and verifies the intergranular fracture that is characteristic of creep deformation and the previous description. Additionally, much more extensive cracking is observed on the polished face of the wrought CrCoNi compared to the AM material. This difference reflects the higher creep ductility (and damage tolerance) of the wrought material and is consistent with the larger tertiary creep region in the wrought material than in the AM material (Fig. 2-6). The difference in the amount of cracking before failure is shown for another combination of temperature and applied stress in Fig. 2-18. Fig. 2-19 illustrates a comparison of the wrought and AM material crept to 4% strain. This is in the middle of steady state creep for the AM material and at the beginning of steady state creep for the wrought material. As shown, there is minimal cracking in both materials at 4% strain indicating that most of the cracking occurs during tertiary creep. Additionally, an EBSD map of the fractured wrought material in Fig. 2-17 is presented in Fig. 2-20 from which it can be observed that cracks do not form at TBs. It is important to note that since creep failure occurs by intergranular fracture, and cracks do not form at TBs, the number and type of transverse grain boundaries strongly influence creep ductility. Despite the attempt to minimize differences in grain size of the two materials, the elongated grains in the build direction of the AM material lead to fewer transverse grain boundaries compared to the wrought material which should be beneficial to the creep ductility of the AM material. However, as observed from the fracture surfaces (Fig. 2-16), the higher volume fraction of oxides dominates the creep fracture behavior and limits ductility in the AM material.
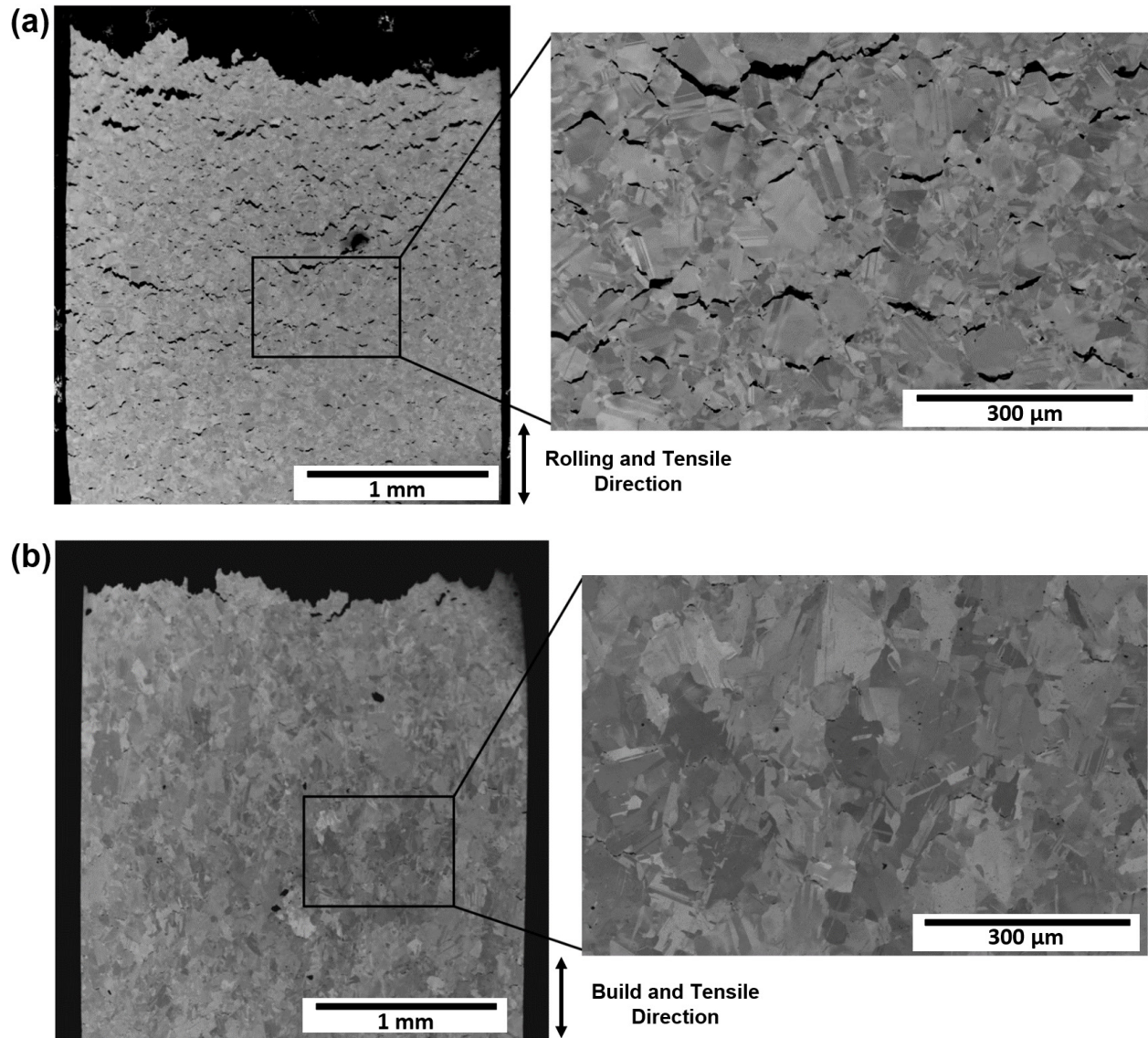
Fig. 2-17 Surfaces of specimens following creep rupture at 1023 K and 80 MPa for (a) wrought CrCoNi and (b) AM CrCoNi.
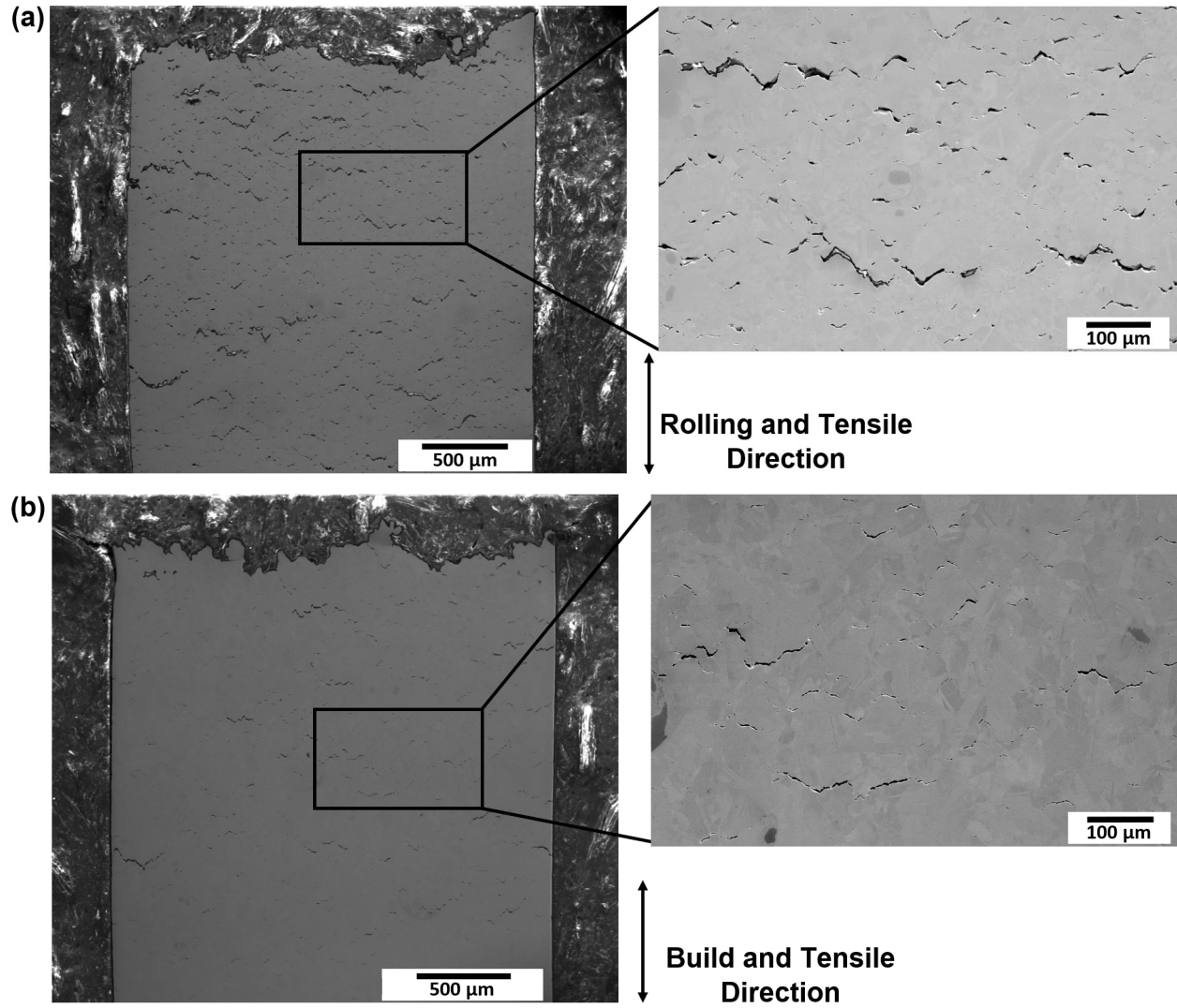
Fig. 2-18 Surfaces of specimens following creep rupture at 1073 K and 80 MPa for (a) wrought CrCoNi and (b) AM CrCoNi.

(a)

Rolling and Tensile Direction

(b)

Build and Tensile Direction
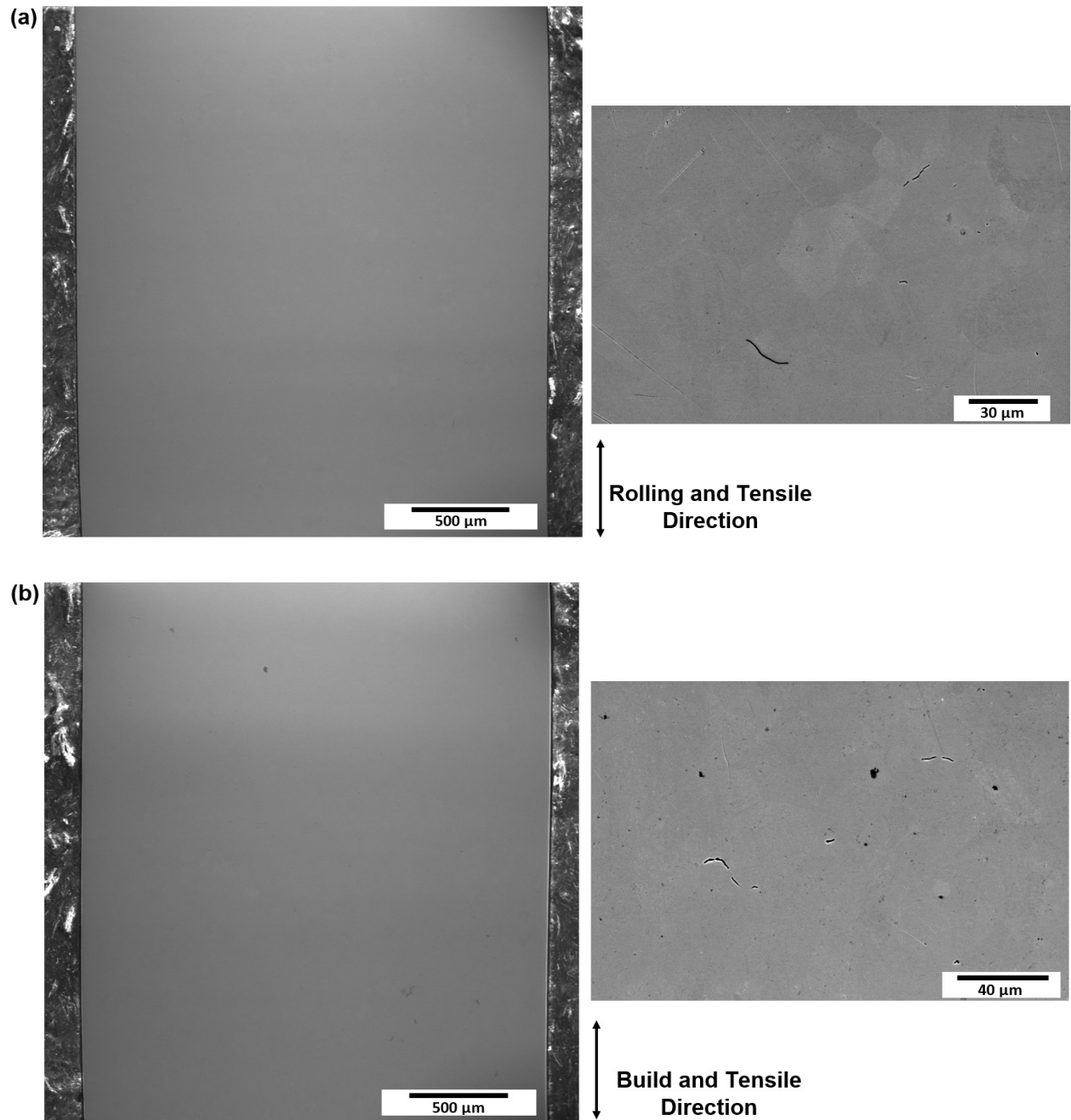
Fig. 2-19 Comparison of the surfaces of the specimens crept to 4% strain for (a) wrought CrCoNi and (b) AM CrCoNi.

40
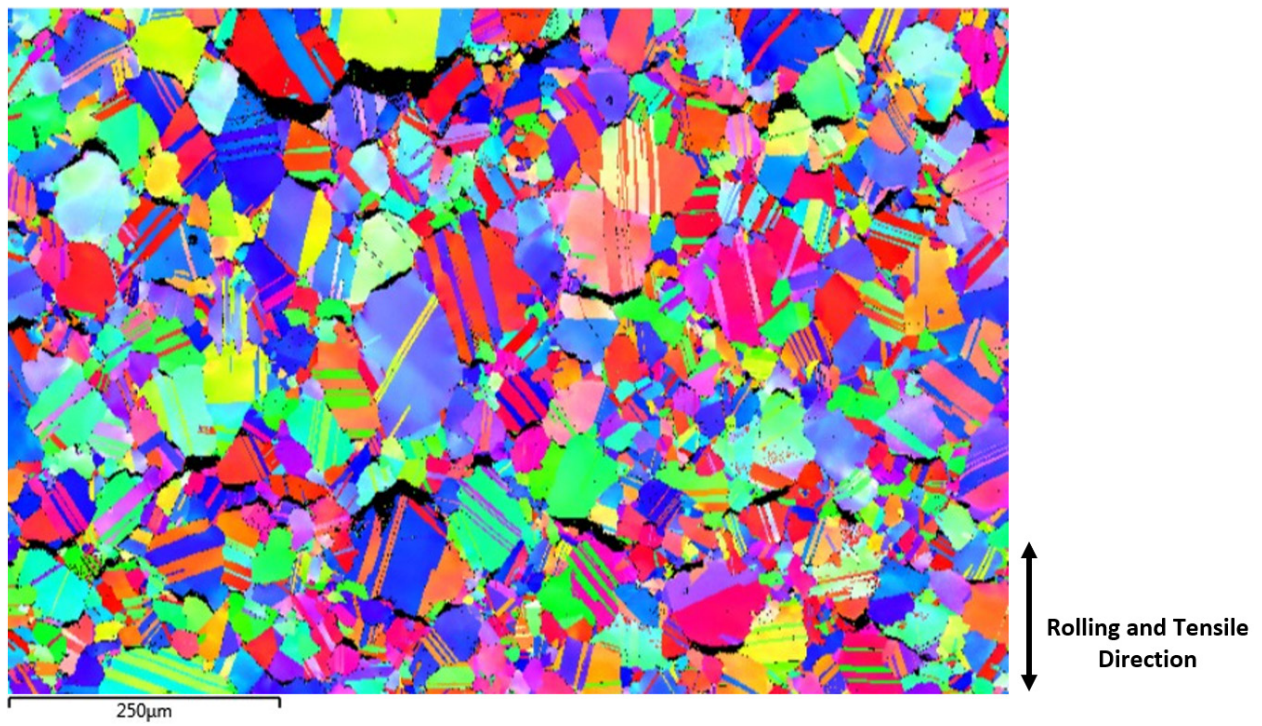
Fig. 2-20 EBSD map of the wrought CrCoNi specimen surface following creep rupture at 1023 K and 80 MPa.

The high initial dislocation density of the AM material could also contribute to its lower creep ductility; however, these dislocations annihilate during furnace heating and stabilization before creep testing which takes 3.5 hours. Fig. 2-21 shows that there is a minimal number of dislocations in the AM material after annealing at 1073 K for 6 hours (which is slightly longer than the normal heat-up period). Fig. 2-22 presents a log-log plot of steady state creep rate vs applied stress for the annealed and non-annealed AM material demonstrating that the steady state creep rates are unaffected by annealing. Additionally, creep ductilities for annealed and non-annealed AM CrCoNi were found to be within 1% for each set of testing parameters. These results show that the annealed and non-annealed AM material have nearly identical creep resistance and creep ductility, confirming that the high initial dislocation density of the AM material does not affect the creep behavior for the given testing procedures. The BSE SEM image in Fig. 2-23 shows the grain morphology of the annealed AM material with crystallite size of 16.8 ± 2.3 μm in the Z-direction of the YZ plane and 14.9 ± 2.3 μm in the Y-direction of the YZ plane. The annealing process allowed the crystallites to become more equiaxed, however the average size has not changed suggesting that the crystallites in the HIPed AM material have achieved a stable size [50, 51].
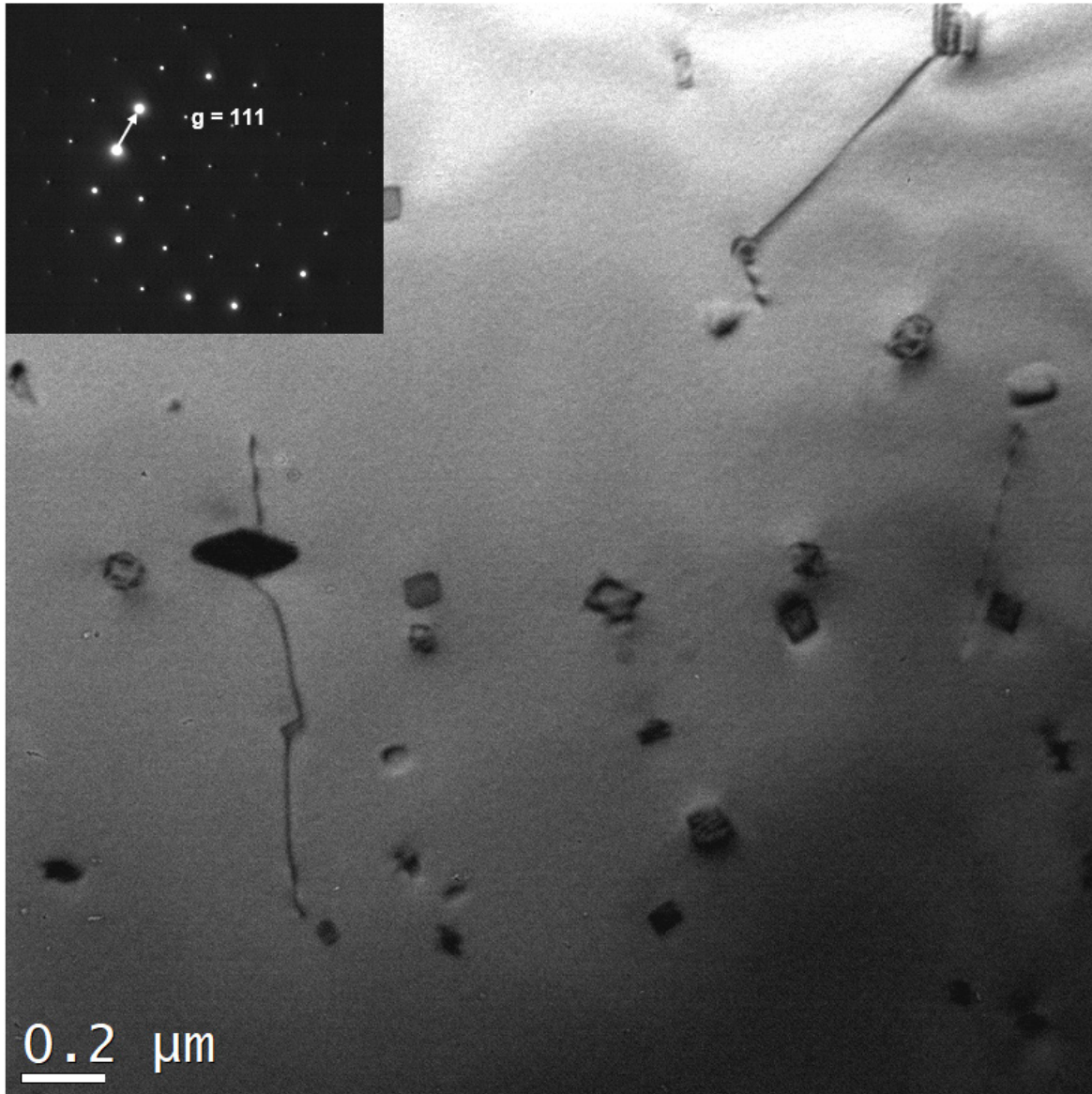
Fig. 2-21 TEM image of AM CrCoNi annealed at 1073 K for 6 hours showing a very low initial dislocation density.
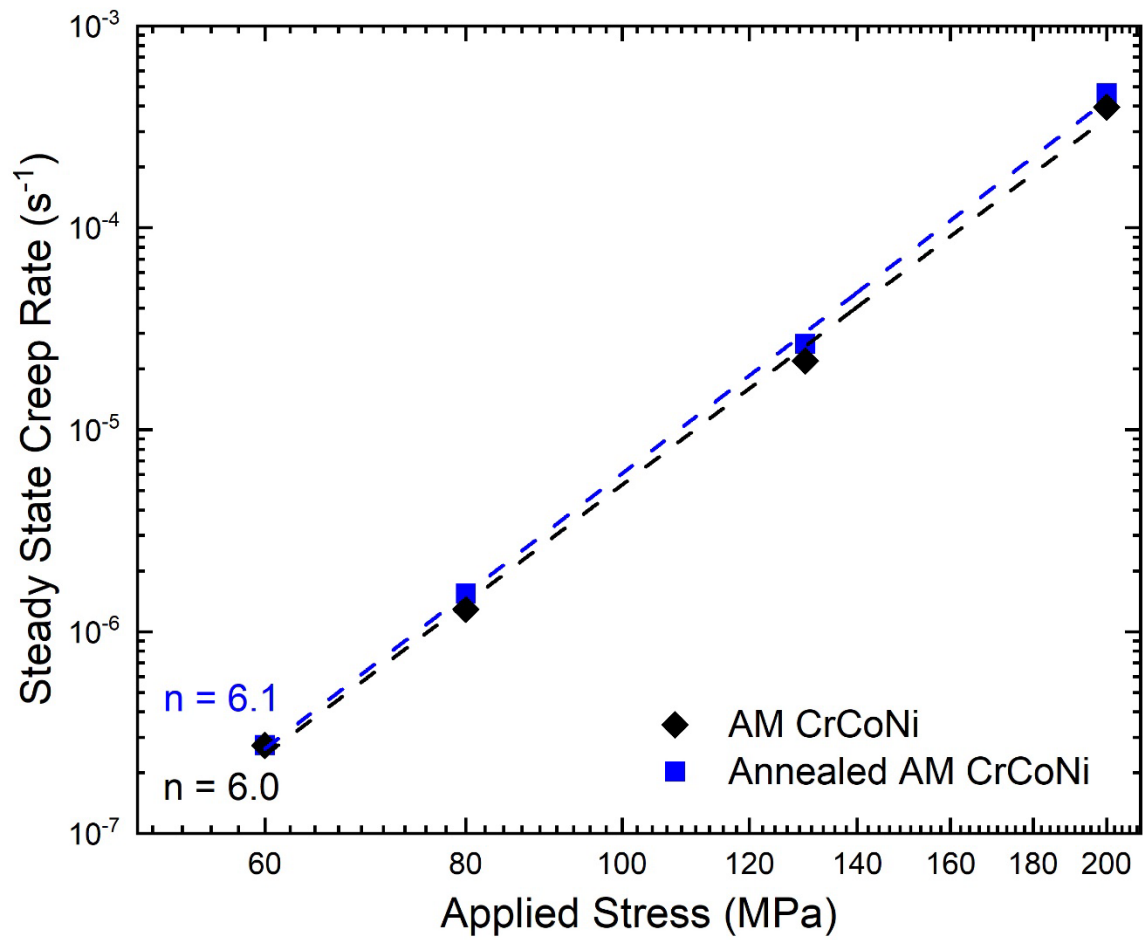
Fig. 2-22 Log-log plot of steady state creep rate vs applied stress for annealed and non-annealed AM CrCoNi crept at 1073 K.
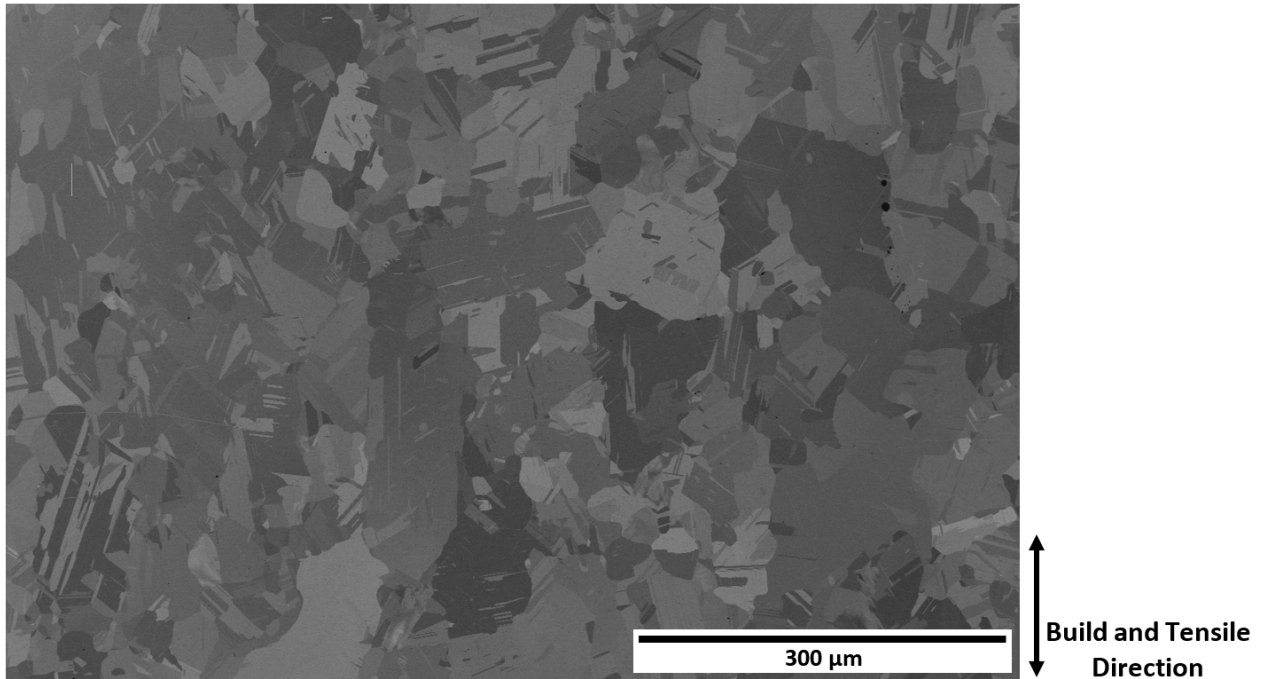
Fig. 2-23 BSE SEM image of annealed AM CrCoNi.

2.3.6 Comparison of Creep Behaviors

A comparison of creep data for CrCoNi and Cantor alloy is shown in Table 2-2. As discussed

earlier, the activation energies of AM CrCoNi, wrought CrCoNi, and Cantor alloy are

sequentially lower, reflecting their respective creep resistance. However, the activation energy

values for wrought CrCoNi from Xie, et al. [36] exceeds those for both the wrought and AM

CrCoNi of this study. This is likely due to the use of a constant load technique in their study as

opposed to the constant stress technique used in the present study and that of Zhang, et al. [10] as

well as the significantly larger grain size used in the study by Xie, et al.

Table 2-2 Comparison of creep data for CrCoNi and Cantor alloy.

Study	Grain Size (μm)	n	Q_C (kJ/mol)	T range (K)	σ range (MPa)
Wrought CrCoNi (This study)	31.2 ± 1.9	4.5 ± 0.2	240-259	1023-1173	40-200
AM CrCoNi (This study)	57.9 ± 2.5	5.9 ± 0.1	320-331	1023-1173	40-200
Wrought CrCoNi [36]	149 ± 4	5.3 ± 0.2	370	973-1073	30-130
Wrought CrMnFeCoNi [10]	24 ± 12	3.7 ± 0.1	219-236	1023-1173	20-200

One approach is to consider the AM material to be composite strengthened by non-deformable

particulates. An approach by Hong and Chung [52] is adopted as given by Eq. (2.2), which is a

simplified version of the Nardone and Prewo model [53]. Eq. (2.2) has also been used by Zhang,

et al. for a similar purpose to describe creep deformation in a rapidly solidified Al–Fe–V–Si

alloy [54].

$$\sigma_{eff} = \sigma \left[1 - \frac{f \times \left(\frac{S}{2}+1\right)}{f \times \left(\frac{S}{2}+1\right) + (1-f)} \right] \tag{2.2}$$

In this expression, σ_{eff} is the effective stress after accounting for the portion of the load carried by the particles, f is the volume fraction of particles in the material, and S is the aspect ratio of the particles. It can be observed that the use of σ_{eff} with constant f and S will simply shift the log-log steady state creep rate vs applied stress plot along the stress axis without changing its slope. While the oxides may carry a portion of the applied load and thus lower the steady state creep rates of the AM alloy, the different slopes (different values of n) between the AM and wrought CrCoNi cannot be explained by this simple composite approach.

Another important point to note in considering the source of the differences in creep rates and stress exponents in both materials is that stress exponents for ODS alloys in which dislocation/particle interactions control the deformation rate typically range from 10-50 [55, 56], with single crystal ODS alloys reaching stress exponents as high as 75 [57]. Clearly, the stress exponent of 5.9 ± 0.1 of the AM CrCoNi, although greater than is typical for power law creep in pure metals, does not compare with these high values commonly found in ODS alloys. Hence, a climb or bowing mechanism to overcome the oxides has been ruled out as a primary cause for the better creep resistance and different stress dependence of the AM material. Furthermore, the large size (approximately 100 nm) and low volume fraction of oxides in the AM material (0.6%) are generally not in the range of values in which climb over particles, bowing between particles or dislocation detachment are expected to be rate controlling processes. Additionally, as observed in Figs. 2-13 and 2-14, two Cr_2O_3 particles appear to generate dislocations at the particle/matrix interface. This dislocation nucleation as well as dislocations interacting with and clustering around oxide particles certainly contribute to the creep strength of the AM material, but only isolated instances of dislocation bowing or climb were found in the present study.

In summary, the lower steady state creep rate in the AM material compared to wrought is attributed to a combination of a larger volume fraction of oxides in AM CrCoNi which interact with dislocations and limit the area swept by gliding dislocations after release from an obstacle, these oxide particles carrying a portion of the applied load, and the lower percentage of the relatively soft LAGBs in the AM material.

2.4 Conclusions

A comparative study of the influence of processing methods on the creep properties of a CrCoNi MPEA was conducted. Material was tested in the annealed vacuum arc melted and HIPed additively manufactured conditions and both were chemically and microstructurally characterized to observe differences contributing to their distinct creep behaviors. Constant stress creep tests were performed on both materials in the ranges of 1023-1173 K and 40-200 MPa. TEM was used to observe the steady state creep behavior and BSE SEM was used to characterize the fracture behavior in these materials.

1. Stress exponents of 4.5 ± 0.2 and 5.9 ± 0.1 and activation energies ranging from 240-259 and 320-331 kJ/mol were found for wrought and AM CrCoNi, respectively. These stress exponents are in the range commonly associated with the dislocation climb mechanism of creep deformation, although no subgrains were observed in the CrCoNi as would be expected for typical metals with stress exponents in this range.

2. Cr-rich oxides were observed in the AM material in greater numbers than in the wrought material. The incoherent Cr_2O_3/matrix interface results in the generation of dislocations. Dislocation interactions with these oxide particles and the ability of these particles to bear a portion of the applied load contribute to the increased creep resistance of the AM material. Additionally, these oxides also contribute to the lower steady state creep rates of

the AM alloy by limiting the glide distance of mobile dislocations after overcoming an obstacle.

3. A lower percentage of LAGBs was found in the AM material compared to wrought. Since more energy is required for a dislocation to move through TBs and HAGBs than LAGBs, this difference also leads to increased creep resistance of the AM material.

4. Both CrCoNi materials have better creep resistance than CrMnFeCoNi (Cantor alloy) at similar stresses and temperatures. The steady state dislocation structures were similar in both CrCoNi materials with individual curved dislocations with dislocation multijunctions and jogs, similar to the Cantor alloy. However, slip bands, which have not been reported in the Cantor alloy after creep, were observed in the CrCoNi. Neither material exhibited subgrains which are typical of pure polycrystalline FCC metals.

5. The average creep ductilities were $17.6 \pm 1.6\%$ and $7.1 \pm 1.2\%$ for wrought and AM CrCoNi, respectively. The higher volume fraction of oxides in the AM material provided additional cavity nucleation sites leading to more rapid void coalescence and consequent fracture. The lower number of dislocation pile-ups in the wrought material suggest that the higher percentage of LAGBs allowed deformation to propagate more readily, reducing cavity nucleation at GBs and prolonging fracture. Additionally, the higher percentage of TBs do not act as dislocation sources and thereby reduce the possibility of slip transmission on the other side of the boundary. This difference in creep ductility was reflected by a larger amount of stable cracking before fracture in the wrought material.

Acknowledgements

References

[1]   F. Otto, A. Dlouhy, C. Somsen, H. Bei, G. Eggeler, E.P. George, The influences of temperature and microstructure on the tensile properties of a CoCrFeMnNi high-entropy alloy, Acta Materialia 61 (2013) 5743-5755.

[2]   B. Gludovatz, A. Hohenwarter, K.V.S. Thurston, H. Bei, Z. Wu, E.P. George, R.O. Ritchie, Exceptional damage-tolerance of a medium-entropy alloy CrCoNi at cryogenic temperatures, Nature Communications 7 (2016).

[3]   G. Laplanche, A. Kostka, O.M. Horst, G. Eggeler, E.P. George, Microstructure evolution and critical stress for twinning in the CrMnFeCoNi high-entropy alloy, Acta Materialia 118 (2016) 152-163.

[4]   J. Miao, C.E. Slone, T.M. Smith, C. Niu, H. Bei, M. Ghazisaeidi, G.M. Pharr, M. M.J., The evolution of the deformation substructure in a Ni-Co-Cr equiatomic solid solution alloy, Acta Materialia 132 (2017) 35-48.

[5]   F.D.G. Filho, R.O. Ritchie, M.A. Meyers, M. S.N, Cantor-derived medium-entropy alloys: bridging the gap between traditional metallic and high-entropy alloys, Journal of Materials Research and Technology 17 (2022) 1868-1895.

[6]   Z. Wu, H. Bei, G.M. Pharr, E.P. George, Recovery, recrystallization, grain growth and phase stability of a family of FCC-structured multi-component equiatomic solid solution alloys, Intermetallics 46 (2014) 131-140.

[7]   A. Gali, E.P. George, Tensile properties of high- and medium-entropy alloys, Intermetallics 39 (2013) 74-78.

[8]   J.Y. He, C. Zhu, D.Q. Zhou, W.H. Liu, T.G. Nieh, Z.P. Lu, Steady state flow of the FeCoNiCrMn high entropy alloy at elevated temperatures, Intermetallics 55 (2014) 9-14.

[9]   C. Cao, J. Fu, T. Tong, Y. Hao, P. Gu, H. Hao, L. Peng, Intermediate-temperature creep deformation and microstructural evolution of an equiatomic FCC-structured CoCrFeNiMn high-entropy alloy, Entropy 20(12) (2018).

[10]   M. Zhang, E.P. George, J.C. Gibeling, Tensile creep properties of a CrMnFeCoNi high-entropy alloy, Scripta Materialia 194 (2021).

[11] J.Y. He, H. Wang, H.L. Huang, X.D. Xu, M.W. Chen, Y. Wu, X.J. Liu, T.G. Nieh, K. An, Z.P. Lu, A precipitation-hardened high-entropy alloy with outstanding tensile properties, Acta Materialia 102 (2016) 187-196.

[12] H. Shahmir, M. Nili-Ahmadabadi, A. Shafiee, T.G. Langdon, Effect of a minor titanium addition on the superplastic properties of a CoCrFeNiMn high-entropy alloy processed by high-pressure torsion, Materials Science & Engineering A 718 (2018) 468-476.

[13] Z. Fu, L. Jiang, J.L. Wardini, B. MacDonald, H. Wen, W. Xiong, D. Zhang, Y. Zhou, T.J. Rupert, W. Chen, E.J. Lavernia, A high-entropy alloy with hierarchical nanoprecipitates and ultrahigh strength, Science Advances 4 (2018).

[14] A. Hoffman, L. He, M. Luebbe, H. Pommerenke, J. Duan, P. Cao, K. Sridharan, Z. Lu, H. Wen, Effects of Al and Ti additions on irradiation behavior of FeMnNiCr multi-principal-element alloy, JOM 72 (2020) 150-159.

[15] D.A. Santana, K.R. Santos, C.S. Kiminami, F.G. Coury, Design, phase equilibria, and coarsening kinetics of a new γ/γ' precipitation-hardened multi-principal element alloy, Journal of Alloys and Compounds 882 (2021).

[16] H. Hadraba, Z. Chlup, A. Dlouhy, F. Dobes, P. Roupcova, M. Vilemova, J. Matejicek, Oxide dispersion strengthened CoCrFeNiMn high-entropy alloy, Materials Science & Engineering A 689 (2017) 252-256.

[17] T.M. Smith, A.C. Thompson, T.P. Gabb, C.L. Bowman, C.A. Kantzos, Efficient production of a high-performance dispersion strengthened, multi-principal element alloy, Scientific Reports (2020).

[18] D. Yang, Y. Liu, N. Qu, T. Han, M. Liao, Z. Lai, J. Zhu, Effect of fabrication methods on microstructures, mechanical properties and strengthening mechanisms of Fe0.25CrNiAl medium-entropy alloy, Journal of Alloys and Compounds 888 (2021).

[19] F. Otto, N.L. Hanold, E.P. George, Microstructural evolution after thermomechanical processing in an equiatomic, single-phase CoCrFeMnNi high-entropy alloy with special focus on twin boundaries, Intermetallics 54 (2014) 39-48.

[20] S.E. Broyles, M. Zhang, J.C. Gibeling, Influence of annealing on the creep behavior of GlidCop Al-15, Materials Science & Engineering A 779 (2020).

[21] M. Schneider, E.P. George, T.J. Manescau, T. Zalezak, J. Hunfeld, A. Dlouhy, G. Eggeler, G. Laplanche, Analysis of strengthening due to grain boundaries and annealing twin boundaries in the CrCoNi medium-entropy alloy, International Journal of Plasticity 124 (2020) 155-169.

[22] M.W. Decker, J.R. Groza, J.C. Gibeling, Creep properties of an extruded copper-8% chromium-4% niobium alloy, Mat Sci Eng a-Struct 369(1-2) (2004) 101-111.

[23] C.E. Slone, J. Miao, E.P. George, M.J. Mills, Achieving ultra-high strength and ductility in equiatomic CrCoNi with partially recrystallized microstructures, Acta Materialia 165(15) (2019) 496-507.

[24] S. Liu, D. Wan, S. Guan, Y. Fu, X. Ren, Z. Zhang, J. He, Microstructure and nanomechanical behavior of an additively manufactured (CrCoNiFe)94Ti2Al4 high-entropy alloy, Materials Science & Engineering A 823(17) (2021).

[25] G.D. Sathiaraj, W. Skrotzki, A. Pukenas, R. Schaarschuch, R.J. Immanuel, S.K. Panigrahl, J.A. Chelvan, S.S.S. Kumar, Effect of annealing on the microstructure and texture of cold rolled CrCoNi medium-entropy alloy, Intermetallics 101 (2018) 87-98.

[26] M. Schneider, E.P. George, T.J. Manescau, T. Zalezak, J. Hunfeld, A. Dlouhy, G. Eggeler, G. Laplanche, Analysis of strengthening due to grain boundaries and annealing

twin boundaries in the CrCoNi medium-entropy alloy, Internation Journal of Plasticity 124 (2020) 155-169.

[27] O.D. Sherby, P.M. Burke, Mechanical behavior of crystalline solids at elevated temperature, Progress in Materials Science 13 (1968) 323-390.

[28] K. Jin, C. Zhang, F. Zhang, H. Bei, Influence of compositional complexity on interdiffusion in Ni-containing concentrated solid-solution alloys, Materials Research Letters (2018).

[29] S. Sun, W. Zai, Y. Chen, G. Sun, J. Hu, S. Han, J. Lian, Effects of cold-rolling and subsequent annealing on the nano-mechanical and creep behaviors of CrCoNi medium-entropy alloy, Materials Science & Engineering A 839 (2022).

[30] S. Chen, Q. Yu, The role of low angle grain boundary in deformation of titanium and its size effect, Scripta Materialia 163 (2019) 148-151.

[31] F. Habiyaremye, A. Guitton, F. Schafer, F. Scholz, M. Schneider, J. Frenzel, G. Laplanche, N. Maloufi, Plasticity induced by nanoindentation in a CrCoNi medium-entropy alloy studied by accurate electron channeling contrast imaging revealing dislocation-low angle grain boundary interactions, Materials Science & Engineering A 817 (2021).

[32] J. Silcox, P.B. Hirsch, Direct observations of defects in quenched gold, Philos Mag 4(37) (1959) 72-89.

[33] O.D. Sherby, R.H. Klundt, A.K. Miller, Flow stress, subgrain size, and subgrain stability at elevated temperature, Metallurgical Transactions A 8 (1977) 843-850.

[34] G. Laplanche, A. Kostka, C. Reinhart, J. Hunfeld, G. Eggele, E.P. George, Reasons for the superior mechanical properties of medium-entropy CrCoNi compared to high-entropy CrMnFeCoNi, Acta Materialia 128 (2017) 292-303.

[35] H. Huang, X. Li, Z. Dong, W. Li, S. Huang, D. Meng, X. Lai, T. Liu, S. Zhu, L. Vitos, Critical stress for twinning nucleation in CrCoNi-based medium and high entropy alloys, Acta Materialia 149 (2018) 388-396.

[36] D. Xie, R. Feng, P.K. Liaw, H. Bei, Y. Gao, Tensile creep behavior of an equiatomic CoCrNi medium entropy alloy, Intermetallics 121 (2020).

[37] M.P. Agustianingrum, U. Lee, N. Park, High-temperature oxidation behaviour of CoCrNi medium-entropy alloy, Corrosion Science 173 (2020).

[38] K. Saeidi, X. Gao, Y. Zhong, Z.J. Shen, Hardened austenite steel with columnar sub-grain structure formed by laser melting, Materials Science & Engineering A 625 (2015) 221-229.

[39] R. Lagneborg, Bypassing of dislocations past particles by a climb mechanism, Scripta Metallurgica 7(6) (1973) 605-614.

[40] W. Blum, B. Reppich, Creep of particle-strengthened alloys, in: B. Wilshire, R.W. Evan (Eds.) Creep Behavior of Crystalline Solids, Pineridge Press Ltd, Swansea, 1985.

[41] J. Rösler, E. Arzt, A new model-based creep equation for dispersion strengthened materials, Acta Metallurgica et Materialia 38(4) (1990) 671-683.

[42] M. Zhang, J.C. Gibeling, Understanding creep mechanisms of a Cu-Cr-Nb alloy by testing under constant structure conditions, Scripta Materialia 190 (2021) 131-135.

[43] L.M. Brown, G.R. Woolhouse, The loss of coherency of precipitates and the generation of dislocations, The Philosophical Magazine: A Journal of Theoretical Experimental and Applied Physics 8 (1970) 329-345.

[44] F.A. McClintok, A criterion for ductile fracture by the growth of holes, Journal of Applied Mechanics 35(2) (1968) 363-371.

[45] R. Lombard, H. Vehoff, Nucleation and growth of cavities at defined grain boundaries in bicrystals, Scripta Metallurgica 24(3) (1990) 581-586.

[46] E.P. George, R.L. Kennedy, D.P. Pope, Review of trace element effects on high-temperature fracture of Fe- and Ni-base alloys, Physica Status Solidi A 167(2) (1998) 313-333.

[47] Y.S. Lee, J. Yu, Effect of matrix hardness on the creep properties of a 12CrMoVNb steel, Metallurgical and Materials Transactions A 30A (1999) 2331-2339.

[48] M.E. Kassner, T.A. Hayes, Creep cavitation in metals, International Journal of Plasticity 19(10) (2003) 1715-1748.

[49] B.F. Dyson, Continuous cavity nucleation and creep fracture, Scripta Metallurgica 17(1) (1983) 31-37.

[50] M. Hillert, On the theory of normal and abnormal grain growth, Acta Metallurgica 13(3) (1965) 227-238.

[51] H.V. Atkinson, Overview no. 65: Theories of normal grain growth in pure single phase systems, Acta Metallurgica 36(3) (1988) 469-491.

[52] S.H. Hong, K.H. Chung, High temperature creep behavior of SiC/2124Al metal matrix composites, Key Engineering Materials 104-107 (1995) 757-764.

[53] V.C. Nardone, K.M. Prewo, On the strength of discontinuous silicon carbide reinforced aluminum composites, Scripta Metallurgica 20 (1986) 43-48.

[54] M. Zhang, R.J. Lewis, J.C. Gibeling, Mechanisms of creep deformation in a rapidly solidified Al–Fe–V–Si alloy, Materials Science & Engineering A 805 (2021).

[55] V.C. Nardone, J.K. Tien, On the creep rate stress dependence of particle strengthened alloys, Scripta Metallurgica 20 (1986) 797-802.

[56] S.E. Broyles, K.R. Anderson, J.R. Groza, J.C. Gibeling, Creep deformation of dispersion-strengthened copper, Metallurgical and Materials Transactions A 27 (1996) 1217-1227.

[57] R.W. Lund, W.D. Nix, High temperature creep of Ni-20Cr-2ThO2 single crystals, Acta Metallurgica 24(5) (1976) 469-481.

Chapter 3. Superior Tensile Creep Behavior of a Novel Oxide Dispersion Strengthened CrCoNi Multi-Principal Element Alloy[2]

3.1 Introduction

Multi-principal element alloys (MPEA), often referred to as high entropy alloys or compositionally complex alloys, are materials in which high proportions of three to five elements are present, typically with a minimum threshold of 10 at% of each element. FCC MPEAs such as equiatomic CrMnFeCoNi (Cantor alloy) and a ternary derivative, CrCoNi, have been studied extensively and exhibit excellent strength and ductility at cryogenic and room temperatures [1-4]. Of the Cantor alloy derivatives, CrMnCoNi has the highest yield strength while the Cantor alloy itself achieves the highest ductility, although CrCoNi generally displays the best combination of strength, ductility, and damage tolerance [5, 6]. The formation of nanotwin-HCP lamellae in CrCoNi at moderate temperatures partitions grains into much smaller structural units that can sustain large lattice rotations, which contributes to extensive strain hardening and to which the superb combination of properties in this material is ascribed [4]. However, poor strength at elevated temperatures has limited the range of applications of MPEAs in areas such as gas turbine engines and thermal energy conversion systems [7, 8].

To overcome this limitation, several investigators have added Ti, Al, and other elements to enhance high temperature strength and other material properties of MPEAs and have essentially created high entropy superalloys [9-13]. However, the addition of these elements alters the MPEA matrix and thus does not take advantage of its unique attributes. Other investigators have used oxide dispersion strengthening (ODS) to increase the high temperature strength and

---

compression creep resistance of MPEAs. For example, Hadraba, et al. added O_2 gas, Y, and Ti to a blend of pure Cantor alloy powders during mechanical alloying with subsequent spark plasma sintering (SPS) of the alloyed powders [14]. Through this process, they demonstrated that it is possible to retain the MPEA matrix with the addition of dispersoids that interact with low angle dislocation boundaries and individual dislocation to improve creep resistance [15]. Smith, et al. have also successfully manufactured an ODS MPEA by laser powder bed fusion (L-PBF) of acoustically mixed yttria-coated CrCoNi particles followed by a hot isostatic pressing (HIP) cycle to cost effectively create additively manufactured (AM) ODS CrCoNi with minimal residual stress [16]. The addition of yttria to the CrCoNi matrix significantly increased the room and high temperature tensile strength of this alloy after HIPing.

Materials manufactured via different processing methods commonly have dissimilar mechanical properties. Substantial differences in microstructure, mechanical properties, and strengthening mechanisms were found by Yang, et al. for an FeCrNiAl medium entropy alloy fabricated by vacuum arc melting, SPS, and hot-press sintering [17]. Sahragard-Monfared, et al. investigated the effect of processing methods on tensile creep properties of wrought and additive manufacturing (AM) CrCoNi and found the latter exhibited higher creep resistance and lower creep ductility than the former. This difference was attributed to the higher volume fraction of Cr-rich oxides and fewer low angle grain boundaries (LAGB) in the AM material. It was also found that the CrCoNi MPEA in both the wrought and AM forms exhibited superior creep resistance compared to the wrought Cantor alloy [8]. With the advancement of AM as a novel, economically viable method for introducing dispersoids into a metal matrix, the new feasibility of ODS makes it an excellent option for overcoming the high temperature strength limitations of FCC MPEAs. Although the elevated temperature strength of BCC MPEAs is currently of great

interest, the superior oxidation resistance of FCC MPEAs makes them more suitable for certain applications without requiring high temperature coatings [18-20]. Additionally, the tensile ductility of FCC MPEAs is significantly greater than that of BCC MPEAs [21]. In order to more fully explore the opportunities afforded by the addition of ceramic dispersoids, this study focuses on the creep properties of AM ODS CrCoNi produced by additive manufacturing.

3.2 Experimental Methods

The AM ODS CrCoNi was fabricated by L-PBF of acoustically mixed pre-alloyed equiatomic CrCoNi and 1 wt% of Y_2O_3 powder with a diameter sizes ranging between 10-45 μm and 100-200 nm, respectively, as described by Smith, et al. [16]. However, even though 1 wt% of oxide was used to coat the powder, the volume fraction of yttria in the final material is 0.6 vol% [16]. Two blanks of AM ODS CrCoNi with a geometry of 88.9 (L) x 15.875 (W) x 15.875 (T) mm were fabricated as a single build and then HIPed at 1458 K to relieve residual stress and densify the material, resulting in 99.9% dense builds. The use of acoustic mixing as opposed to mechanical alloying processes such as high energy ball milling was chosen to ensure the powders did not deform and retained flow properties amenable to AM. A secondary benefit of this approach is its lower cost compared to conventional mechanical alloying processes [16]. Specimens were electrical discharge machined from the build such that their creep tensile axis (Z-direction) is parallel to the build direction. Fig. 3-1 illustrates an isometric view of a tensile creep specimen with gage section dimensions of 35.56 (L) x 2.54(W) x 1.00(T) mm. The surfaces and edges of the gage sections of each specimen were polished using 600 grit SiC paper to minimize the risk of surface defects influencing creep properties.
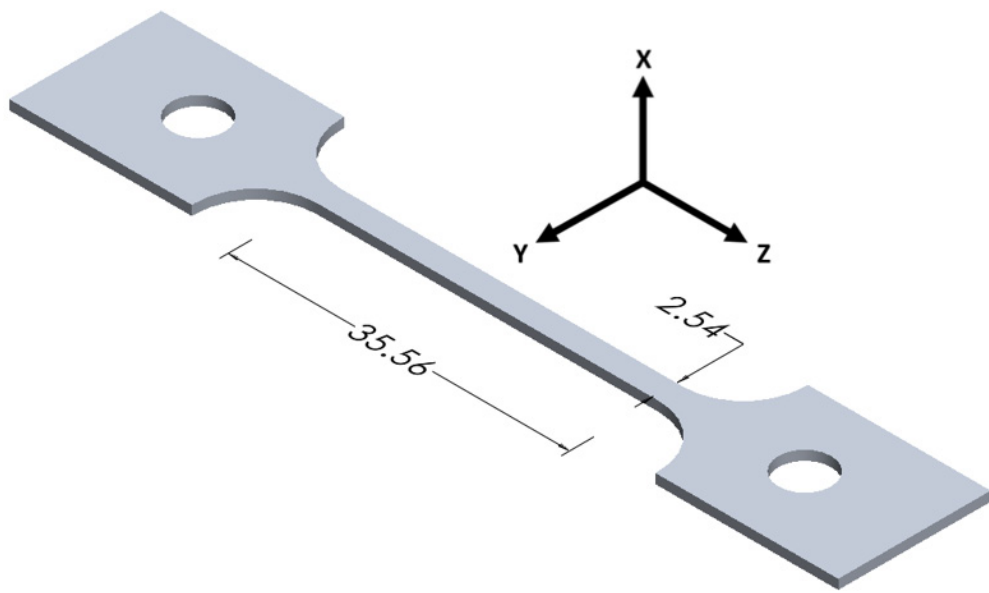
Fig. 3-1 Isometric view of a creep specimen. All dimensions are in mm.

Scanning electron microscopy (SEM) was performed on a Thermo Fisher Quattro S ESEM and an FEI Scios Dual Beam FIB/SEM equipped with energy dispersive x-ray spectroscopy (EDS) and electron backscatter diffraction (EBSD) detectors. All microscopy samples were prepared by grinding and polishing to 0.3 μm with an alumina suspension and then vibropolishing with 0.05 μm colloidal silica for 4 hours. The Quattro ESEM was used in backscatter electron mode to characterize the fractured specimens. The Scios FIB/SEM was used to characterize atomic composition via energy EDS and the grain orientations and boundary misorientations via EBSD. EDS was performed at an operating voltage of 30 kV and EBSD was performed at an operating voltage of 15 kV and step size of 0.8 μm. The EBSD data were post-processed with MTEX (version 5.7.0) in MATLAB following a procedure similar to that employed of Broyles, et al. such that unreasonably small grains are removed and unindexed data points are filled based on the orientations of their neighbors [22]. Average grain size was determined from the boundary misorientation maps using the line intercept method.

Diffraction contrast imaging (DCI)-STEM was performed on an FEI monochromated F20 UT Tecnai S/TEM at an accelerating voltage of 200 kV to observe the dislocation structure of HIPed, annealed, and crept specimens and determine the character of dislocations interacting with particles through $g \cdot b$ analyses. STEM-EDS was carried out on an FEI TitanX 60-300 at an accelerating voltage of 300 kV to identify the composition of particles. TEM specimens from creep samples before deformation and interrupted at steady state deformation were prepared by grinding and polishing the specimen gage surface to 1200 grit and less than 100 μm thickness. The TEM samples were then twin-jet electropolished at -20 ºC using a Fischione Model 110 Automatic Twin-Jet Electropolisher in a 70% methanol, 20% glycerol, and 10% perchloric acid solution.

Constant stress tensile creep tests were performed under vacuum ($\leq 3 \times 10^{-5}$ torr) to avoid oxidation, following the procedures described in previous studies [8, 23]. Tests were performed in the ranges of 1023-1173 K and 40-200 MPa and were conducted until fracture to clearly identify the steady state creep rate except for those terminated after steady state for TEM. The dislocation structure of those samples was preserved by furnace cooling the specimen under the same creep load.

3.3 Results and Discussion

3.3.1 Characterization of Initial Microstructure

Although a uniform distribution of elements has previously been observed in AM CrCoNi, it is important to examine the distribution of elements in this ODS material to confirm this uniformity after the addition of yttria [8, 24, 25]. Fig. 3-2 illustrates the initial chemical composition of AM ODS CrCoNi as determined by SEM-EDS and shows an equiatomic composition with a uniform distribution of the three principal elements. Yttrium and oxygen are not included in Fig. 3-2 due to resolution limitations of the FEI Scios Dual Beam FIB/SEM and the small amount of yttria. However, Smith, et al. have demonstrated that the yttria is well distributed in the microstructure of this material [16].
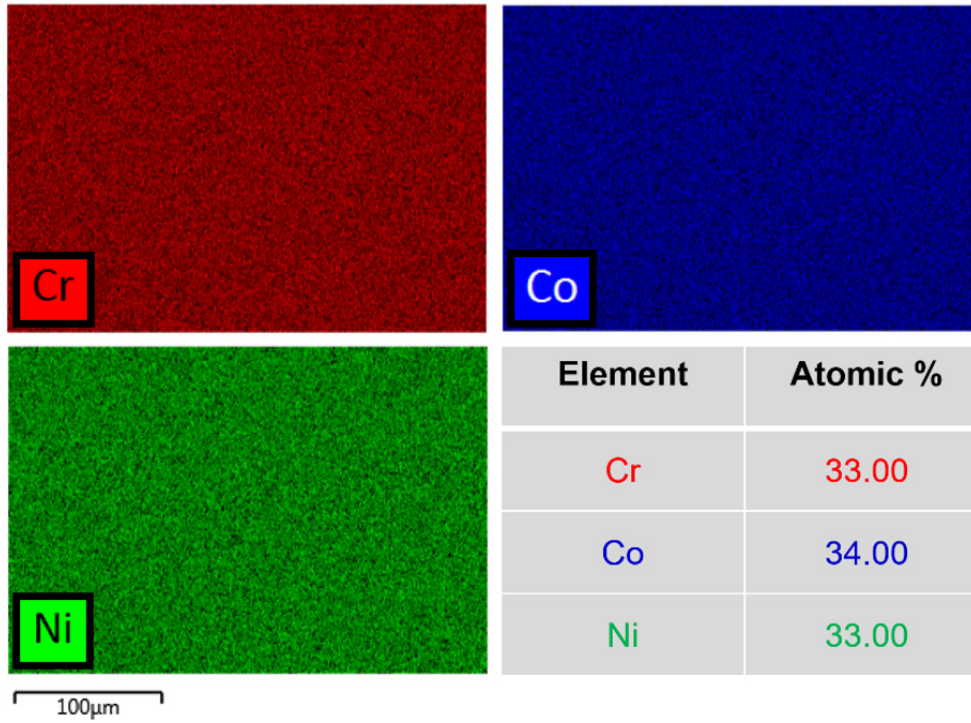
Fig. 3-2 SEM-EDS maps of AM ODS CrCoNi with corresponding atomic percentage.

The EBSD inverse pole figure (IPF) color maps and contour plots displayed in Fig. 3-3 illustrate that there is slight texture favorable to the [111] direction in the YZ plane and the [001] direction in the XZ plane, although the XY plane shows no texture. However, the intensities of these observed textures are low at a maximum value of three for the YZ plane while heavily textured materials exhibit much higher values. Additionally, the calculated Taylor factors for each of these EBSD maps are within 5% of each other and thus the texture observed is not expected to significantly affect the creep properties of AM ODS CrCoNi. As noted by Smith, et al., the formation of annealing twins was suppressed in this material, which is unusual for CrCoNi [8, 16, 26, 27]. The lack of twin boundaries (TB) in AM ODS CrCoNi versus its wrought and non-ODS counterparts is likely due to the pinning of grain boundaries (GB) by the yttria particles, which suppresses recrystallization.
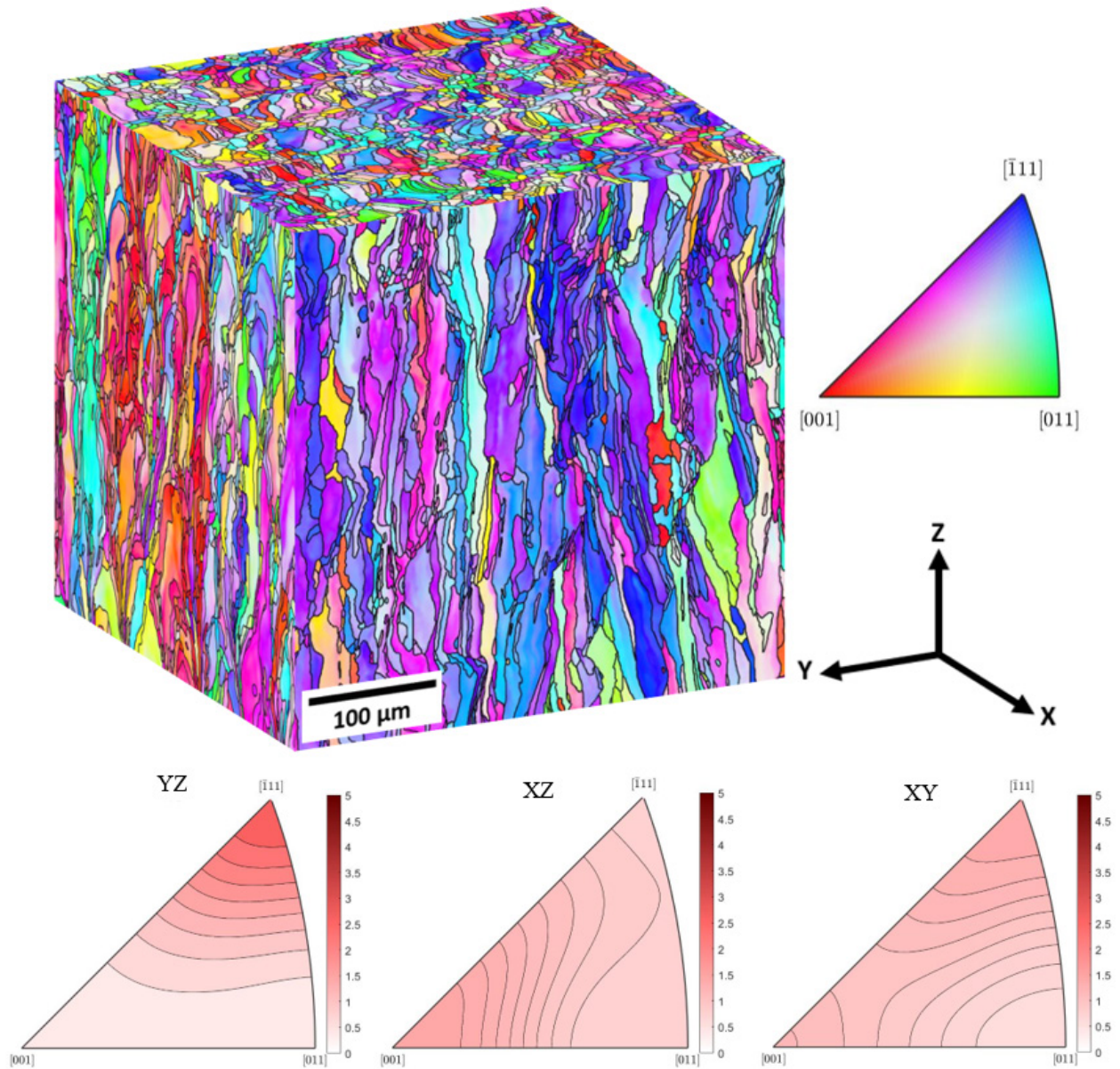
Fig. 3-3 EBSD-IPF color cube and IPF contour plots of AM ODS CrCoNi.

Fig. 3-4 shows boundary misorientation plots of the XY and YZ planes of AM ODS CrCoNi

from which grain sizes were determined. The AM ODS CrCoNi grains are elongated in the build

direction with an aspect ratio of approximately 4:1 such that the grain size is 23.8 ± 1.8 μm in the

Z-direction of the YZ plane and 6.5 ± 1.8 μm in the Y-direction of the YZ plane. As noted by

Smith, et al., the yttria suppressed recrystallization and grain growth during the L-PBF build

process and subsequent HIP cycle by pinning the grain boundaries. Fig. 3-4 illustrates the large

percentage of LAGBs in the AM ODS CrCoNi; the distributions of misorientation angles for the

YZ and XY planes are plotted on histograms in Fig. 3-5. Table 3-1 lists the percentages of

LAGBs, high angle grain boundaries (HAGB), and TBs with these boundaries being defined as

follows: $1\text{-}15°$ (LAGBs), greater than $15°$ excluding TBs (HAGBs), and $60 \pm 3°$ (TBs).
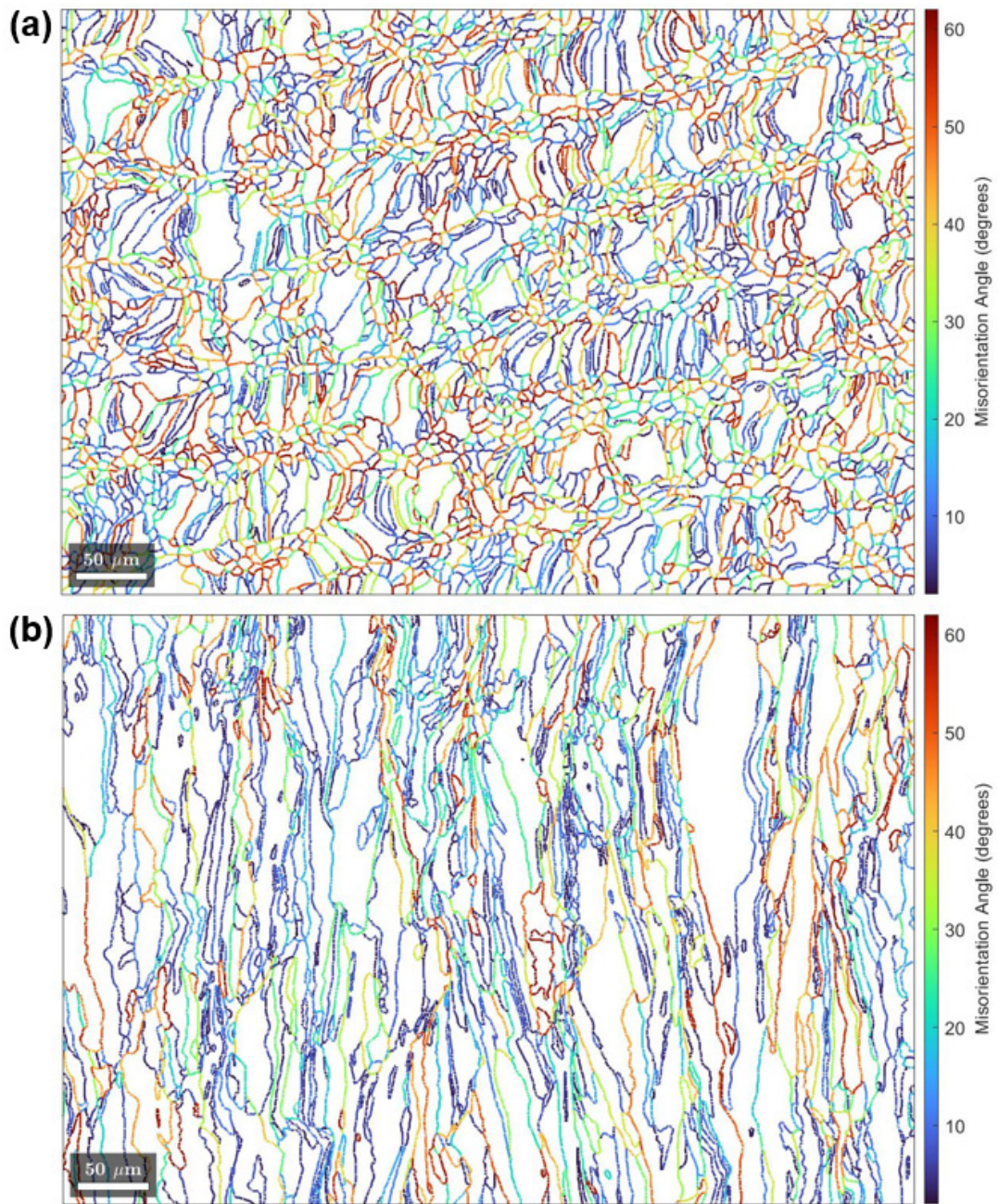
Fig. 3-4 Boundary misorientation plots of (a) XY plane (b) YZ plane of AM ODS CrCoNi.
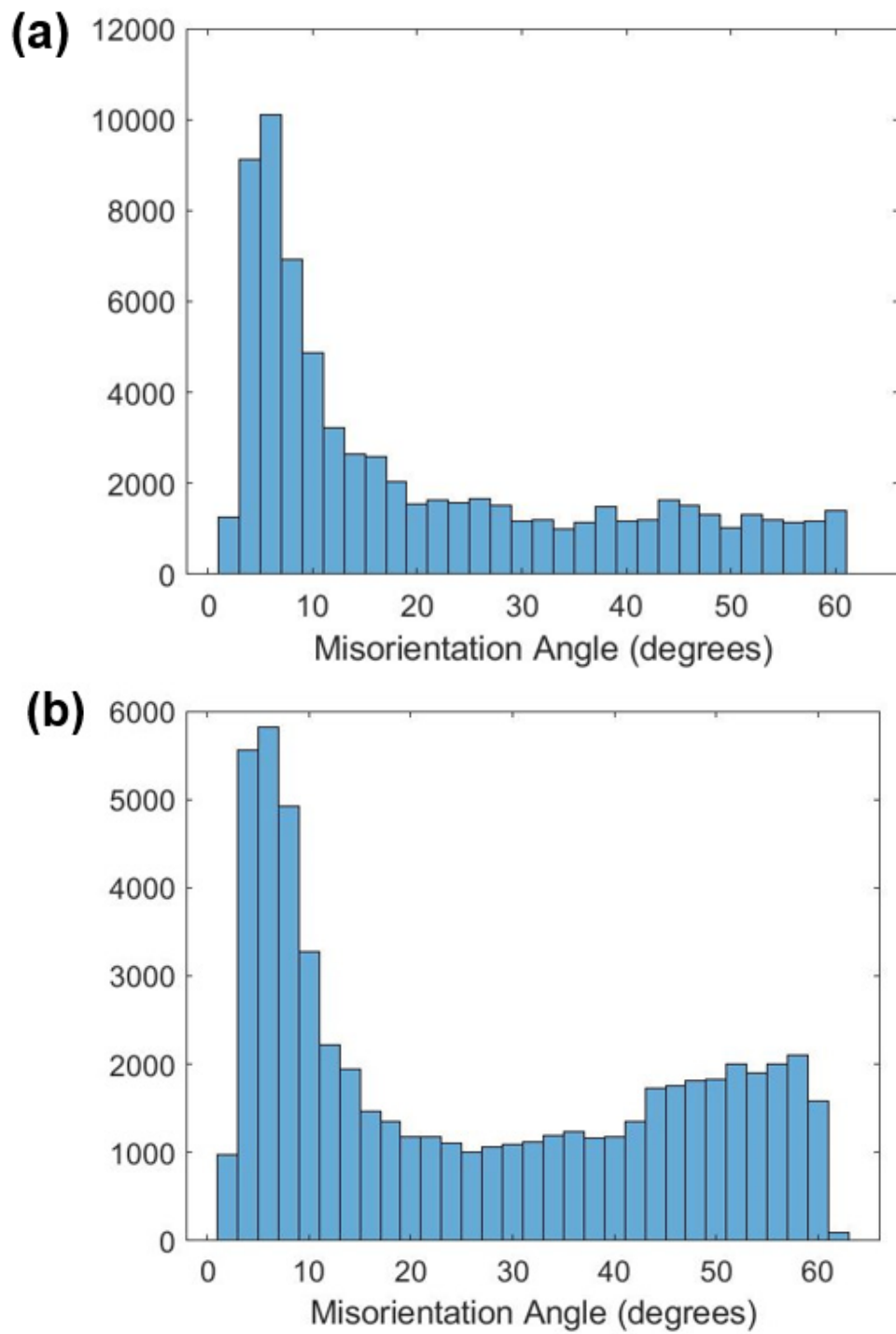
Fig. 3-5 Distributions of misorientation angles for the YZ and XY planes of AM ODS CrCoNi.

Table 3-1 Percentages of low angle grain boundaries, high angle grain boundaries, and twin boundaries.

Material	LAGB	HAGB	TB
AM ODS CrCoNi (YZ)	57.6%	38.8%	3.6%
AM ODS CrCoNi (XY)	45.0%	48.5%	6.5%

3.3.2 Creep Results

Creep curves for representative temperatures and applied stresses are presented in Fig. 3-6, illustrating the effects of these testing conditions. The AM ODS CrCoNi exhibits creep behavior typical of pure metals and alloys that behave like pure metals with distinct normal primary, secondary, and tertiary regions. However, the tertiary regime is significantly shorter in AM ODS CrCoNi compared to its non-ODS counterpart, indicating a rapid failure after cracks have formed [8]. Additionally, it is noted that the creep ductility is substantially higher at an applied stress of 200 MPa.
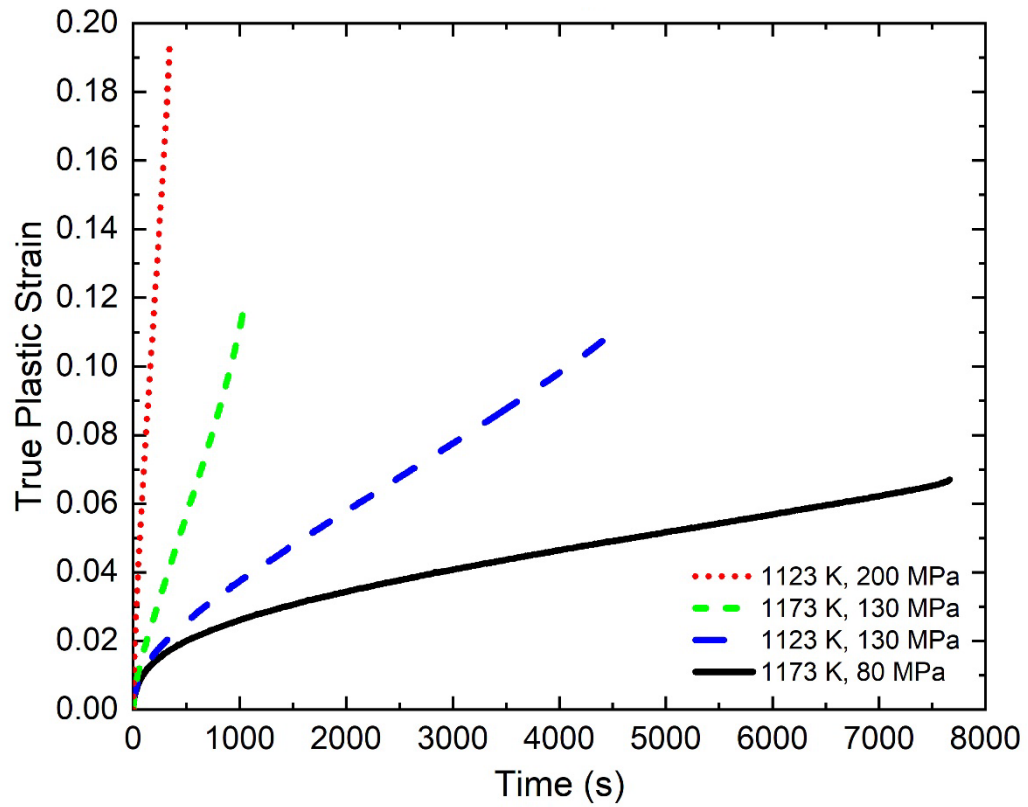
Fig. 3-6 Representative creep curves of AM ODS CrCoNi.

Steady-state creep rates were calculated from the slopes of the secondary region of the creep curves and plotted as a function of applied stress to determine the stress exponents for each material; this relationship is shown on double logarithmic plots in Fig. 3-7. The power law equation (Eq. (3.1)) describes the relationship between steady state creep rate, $\dot{\varepsilon}_{SS}$, and applied stress, σ, where A is a material constant that includes dislocation structure, Q_C represents the creep activation energy, R is the gas constant, T is temperature, and n is the stress exponent [28].

$$\dot{\varepsilon}_{SS} = A\sigma^n \exp\left(-\frac{Q_C}{RT}\right) \tag{3.1}$$

An average stress exponent of 6.5 ± 0.1 was found for AM ODS CrCoNi. This value is slightly above the range commonly associated with the dislocation climb mechanism of creep deformation in subgrain forming metals and below the range for ODS alloys in which dislocation/particle interactions control the deformation. Stress exponents for ODS alloys typically range from 10-50, reaching as high as 75 for single crystal ODS alloys [29-31]. Although the alloy in this study is oxide dispersion strengthened, the inclusion of only 0.6 vol% yttria is likely too low to achieve high stress exponents classically associated with this strengthening method. However, this stress exponent is slightly higher than that of non-ODS AM CrCoNi (5.9 ± 0.1) revealing that the addition of yttria changes the stress dependence of the creep behavior [8]. The stronger MPEA matrix compared to a pure matrix leads to synergistic control of dislocation motion by both the matrix and particles.
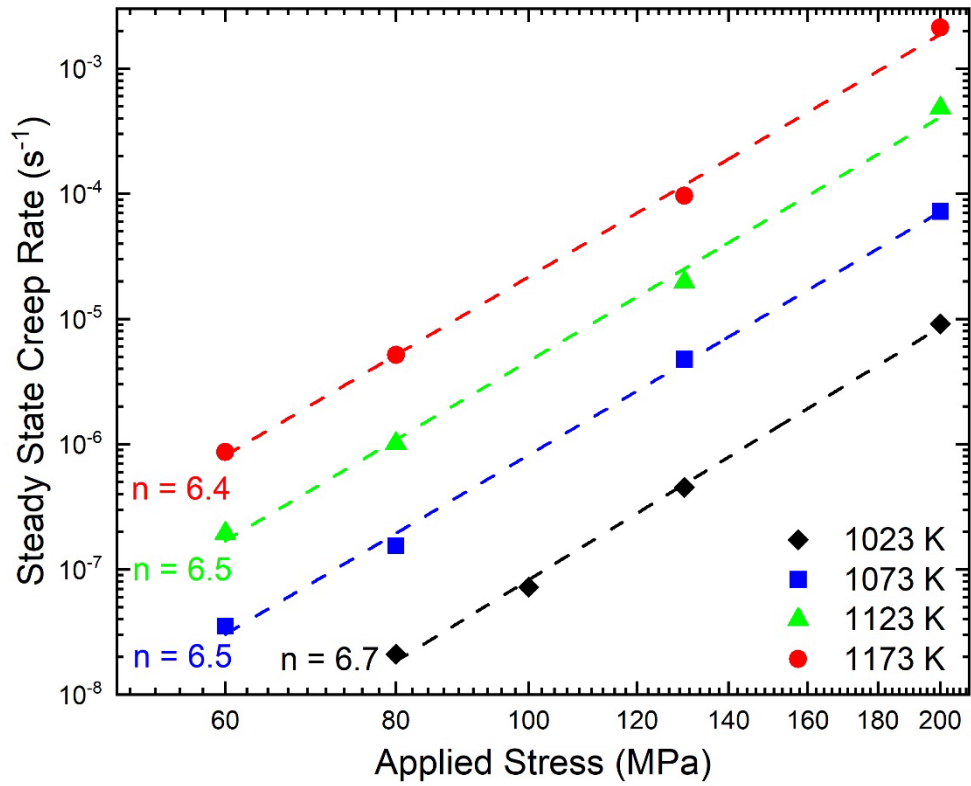
Fig. 3-7 Log-log plot of steady state creep rate vs applied stress for AM ODS CrCoNi.

To visualize the improved creep resistance of AM ODS CrCoNi compared to its non-ODS AM and wrought counterparts and wrought parent (Cantor) alloy, Fig. 3-8(a) illustrates a comparison of the steady-state creep rates and applied stresses of each of these alloys at a single temperature of 1023 K [7, 8]. These data illustrate that AM ODS CrCoNi has better creep resistance than the other alloys. The stress exponent of the AM ODS CrCoNi is also higher than its non-ODS variants and the Cantor alloy when tested under similar conditions, implying different rate-controlling creep deformation mechanisms in these alloys. Fig. 3-8(b) illustrates a comparison of the constant stress tensile creep behavior of AM ODS CrCoNi from the present work to constant load compression creep behavior of SPS ODS Cantor alloy [15]. This comparison shows a significantly improved creep resistance in the AM ODS CrCoNi by three to four orders of magnitude.
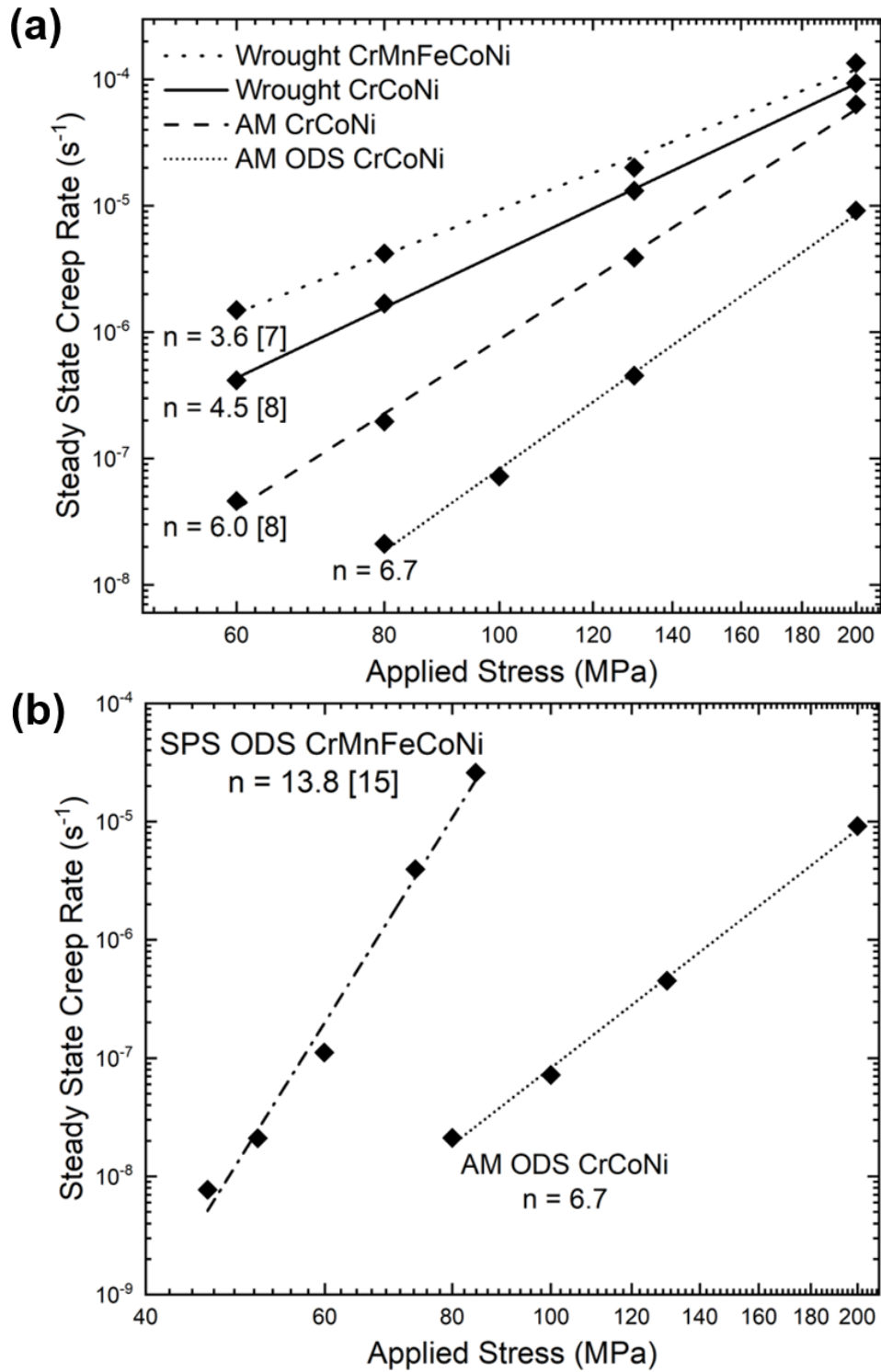
Fig. 3-8 Log-log plot of steady state creep rate vs applied stress for (a) wrought Cantor alloy [7], wrought CrCoNi [8], AM CrCoNi [8], and AM ODS CrCoNi at 1023 K and (b) SPS ODS Cantor alloy [15] and AM ODS CrCoNi at 1023 K.

The activation energy of AM ODS CrCoNi was determined from a semi-log plot of steady state creep rate versus 1/T as shown in Fig. 3-9. The values range from 335-367 kJ/mol for this material. The activation energy of non-ODS AM and wrought CrCoNi have been reported as being lower, ranging from 320-331 kJ/mol for AM and 240-259 kJ/mol for wrought, reflecting the increased temperature resistance provided by the AM process and the addition of yttria in the ODS material [8]. Additionally, the activation energy of the wrought Cantor alloy has been reported as 219-236 kJ/mol, again reflecting the better creep resistance of its derivative alloy [7].
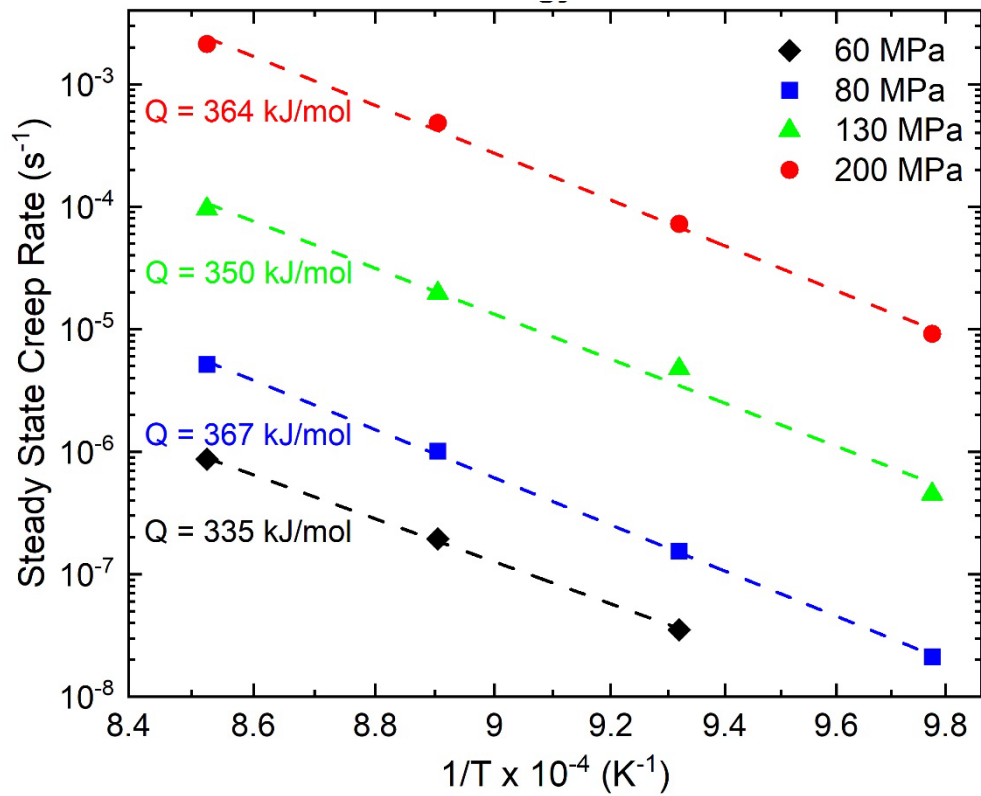
Fig. 3-9 Semi-log plot of state creep rate vs 1/T for AM ODS CrCoNi.

The AM process and addition of oxides also affects the distribution of grain boundary misorientations which have an effect on creep resistance. For a LAGB, grain orientations on each side of the boundary are similar such that a lower stress concentration is required for the propagation of deformation to occur between these grains than those with HAGB [32, 33]. One contributing factor of the lower creep resistance of wrought CrCoNi compared to the AM version is reported to be a smaller percentage of LAGB in the AM material [8]. Although the high percentage of LAGBs in the AM ODS CrCoNi may have a negative impact on its creep resistance, the large number of vertical GBs provides a slight positive resistance to the propagation of strain across grains.

3.3.3 Characterization of Dislocation Structure and Oxides in AM ODS CrCoNi

The AM ODS CrCoNi in the HIPed, annealed, and crept conditions was examined by TEM to understand the evolution of the dislocation structure in this material and characterize the oxides present and their interactions with dislocations. The dislocation structure of the HIPed condition is illustrated in Fig. 3-10, showing a moderate dislocation density, dislocation/oxide interactions, extended nodes, and stacking fault tetrahedra (SFT). Extended nodes are a low energy dislocation configuration and are present in this alloy due to its low stacking fault energy of 22 ± 4 mJ m^{-2} [34]. SFT form as a result of vacancy condensation, which is a process that is assisted by low stacking fault energy. Silcox and Hirsch first observed SFT in quenched gold [35]. The SFT in the AM material likely formed during the rapid cooling associated with the L-PBF process which occurs at rates that are similar to or higher than quenching.
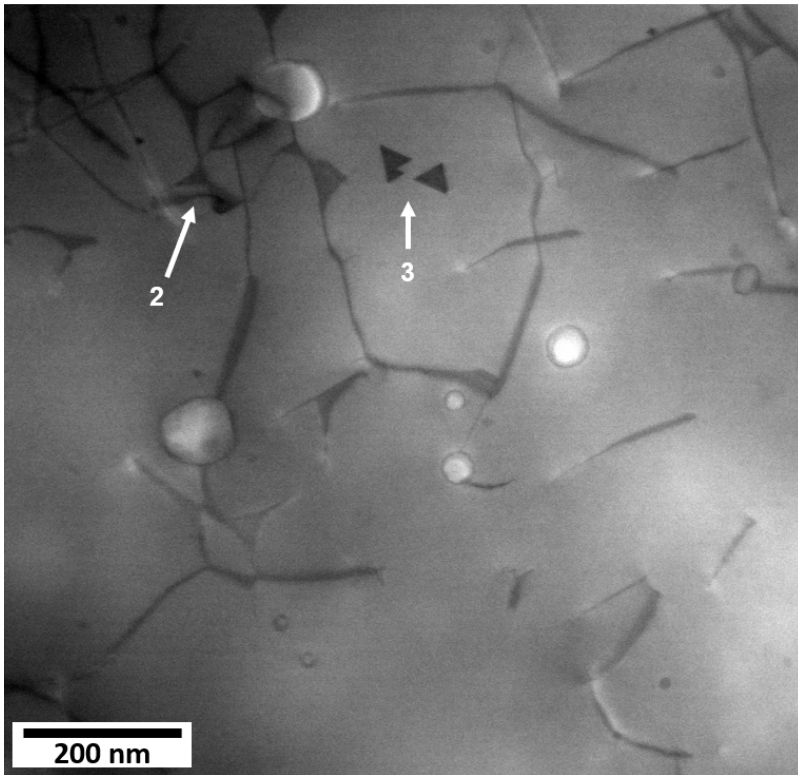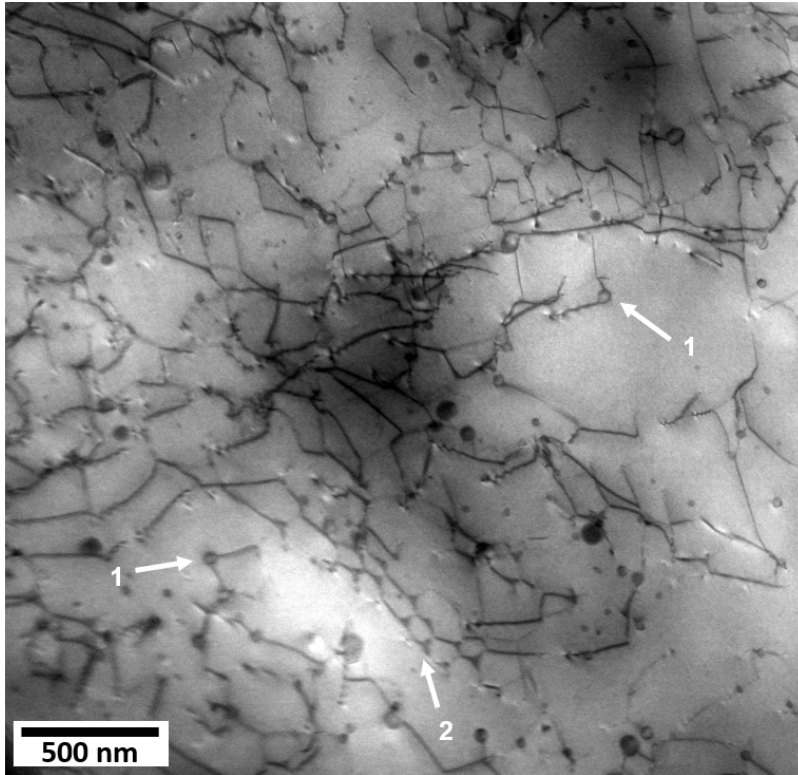
Fig. 3-10 Dislocation structure of HIPed CrCoNi showing dislocation/oxide interactions (arrows 1), extended nodes (arrows 2), and SFT (arrow 3).

The dislocation structure of AM ODS CrCoNi after annealing at 1023 K for 3.5 hours is observed in Fig. 3-11. This annealing temperature and time were chosen to imitate the process that takes place before creep testing in which the furnace temperature is allowed to equilibrate, leading to changes in dislocation structure immediately before creep testing. STEM-EDS of the annealed material revealed yttrium and chromium rich oxides as seen in Fig. 3-12. The latter were also observed in the non-ODS CrCoNi [8]. Annealing the AM ODS CrCoNi resulted in the reduction of stored energy via dislocation network formation since dislocations were pinned at yttria particles and unable to move to annihilate with dislocations of the opposite sign. This mechanism of reducing stored energy during annealing is unlike that of the non-ODS CrCoNi in which dislocations are able to annihilate, leading to a very low dislocation density at the start of the creep tests [8]. Dislocation/oxide interactions, extended nodes, and SFT are present in the annealed material with SFT being more prevalent than in the HIPed material. Fig. 3-13 shows additional STEM-EDS of the annealed material illustrating dislocations that are pinned by yttria.
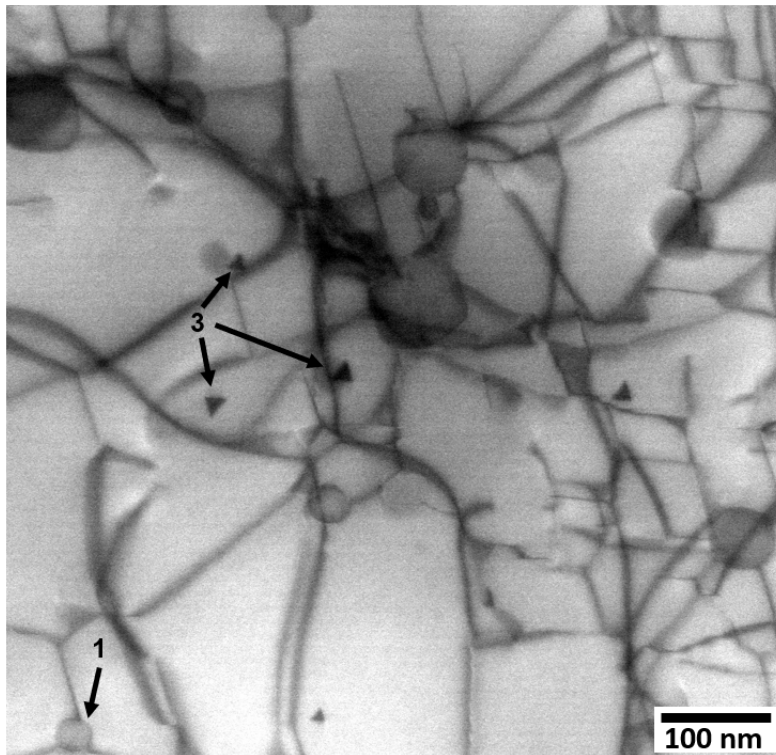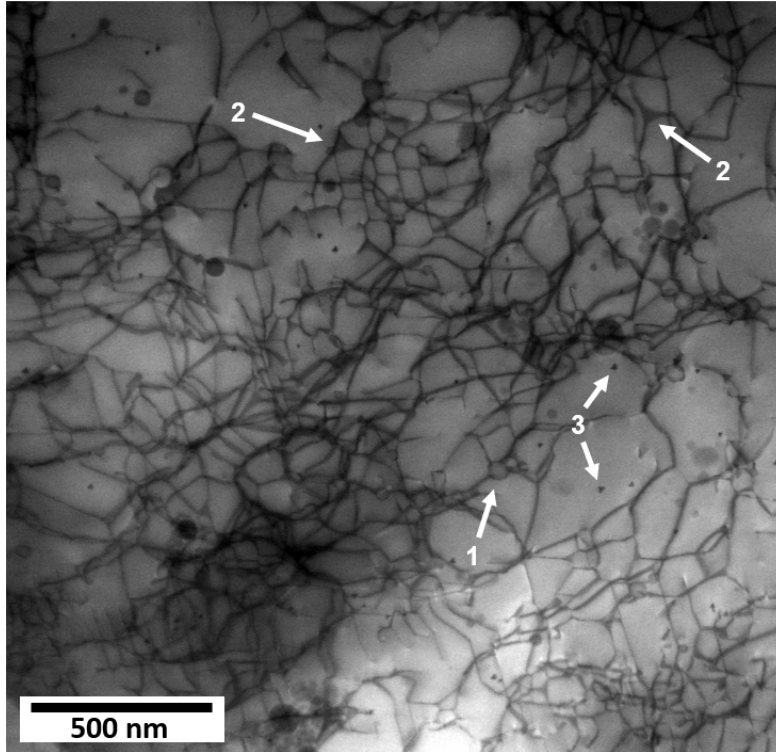
Fig. 3-11 Dislocation structure of annealed CrCoNi showing dislocation/oxide interactions (arrows 1), extended nodes (arrows 2), and SFT (arrows 3).
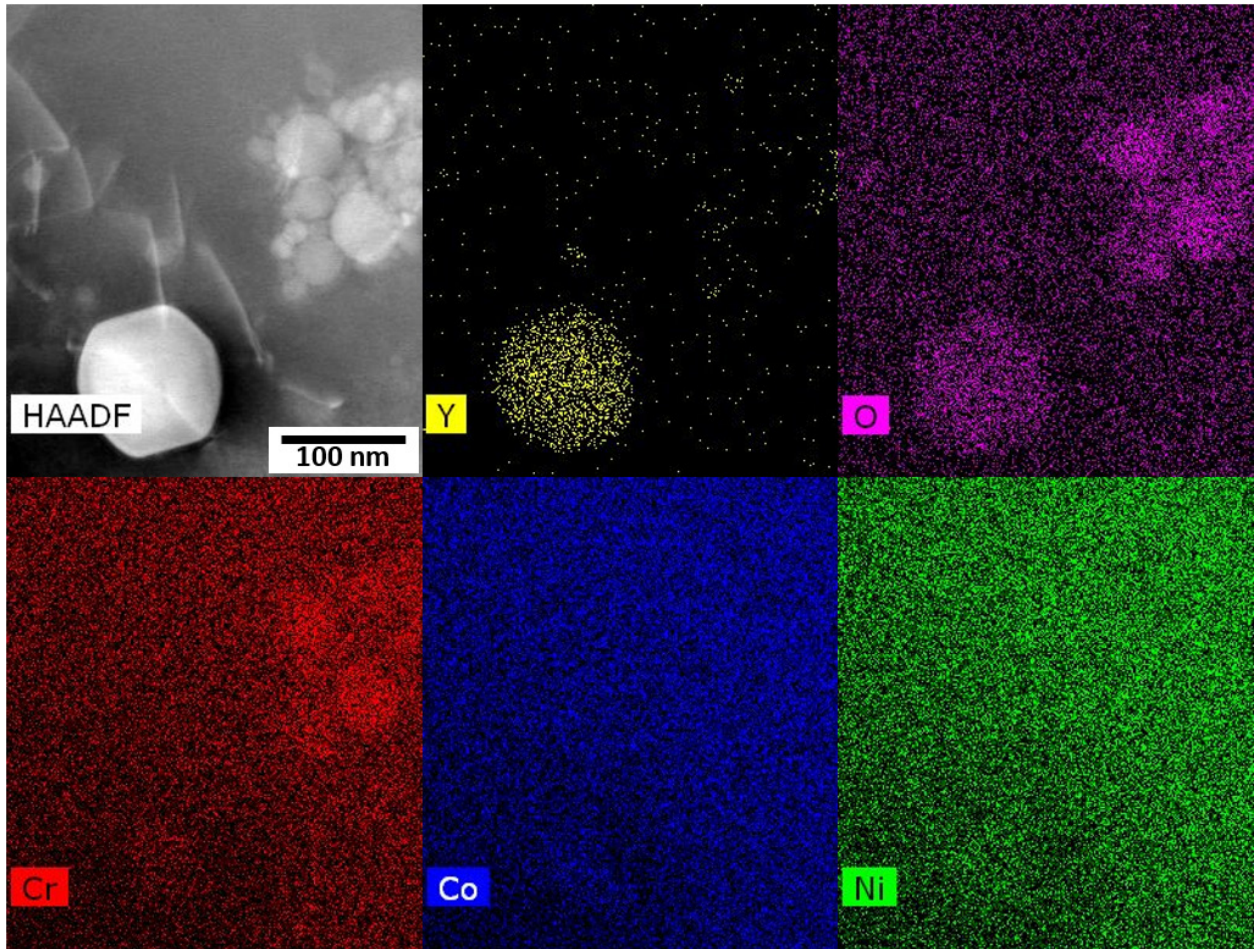
Fig. 3-12 High angle annular dark field (HAADF) and STEM-EDS of annealed AM ODS CrCoNi revealing yttrium and chromium rich oxides.
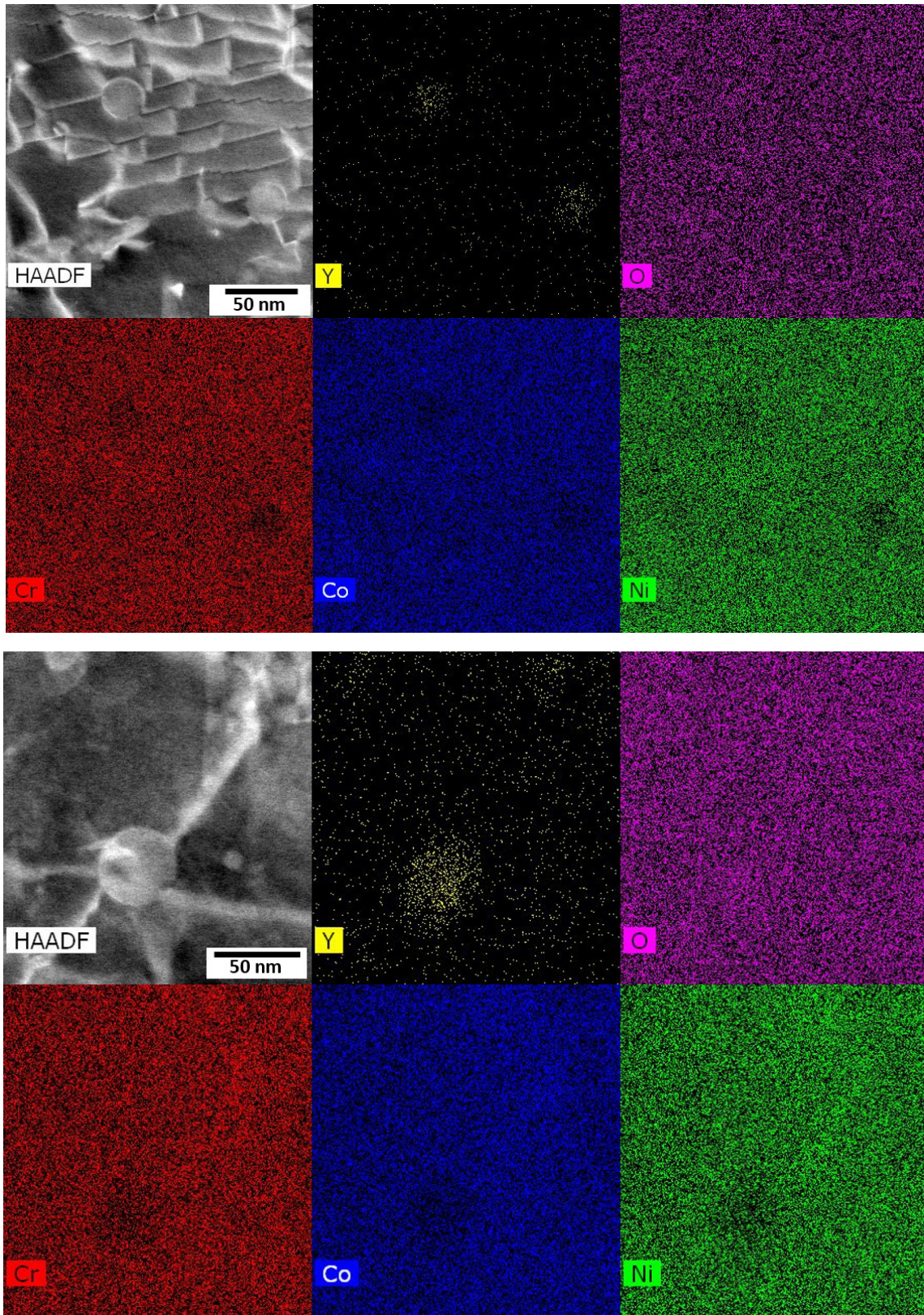
Fig. 3-13 High angle annular dark field (HAADF) and STEM-EDS of annealed AM ODS
CrCoNi illustrating dislocations interacting with yttria.

The dislocation structure of AM ODS CrCoNi at steady state for a temperature of 1023 K and a stress of 80 MPa is shown in Fig. 3-14 and displays a high dislocation density. Long arrays of relatively straight dislocations are observed in the crept material, which is significantly different from the lower density of individual curved dislocations observed in non-ODS CrCoNi [8]. The presence of dislocation arrays that are perpendicular suggests that they may represent incipient subgrain formation. STEM-EDS of the specimen crept to steady state at 1023 K and 80 MPa, as seen in Fig. 3-15, illustrates a dislocation interaction with an yttria particle. To determine the character of dislocations interacting with oxides, $g \cdot b$ analysis was implemented as illustrated in Fig. 3-16. Dislocation/oxide interactions were imaged from seven different g vectors. Burgers vectors resulting in $g \cdot b = 0$ for g vectors in which dislocations were not visible were projected onto the TEM images to determine if the dislocation line vectors and Burgers vectors were parallel (screw dislocation), perpendicular (edge dislocation), or at an intermediate angle (mixed dislocation). The character of these dislocations is mixed, necessitating that they interact with and climb over oxides rather than cross slipping to another glide plane.
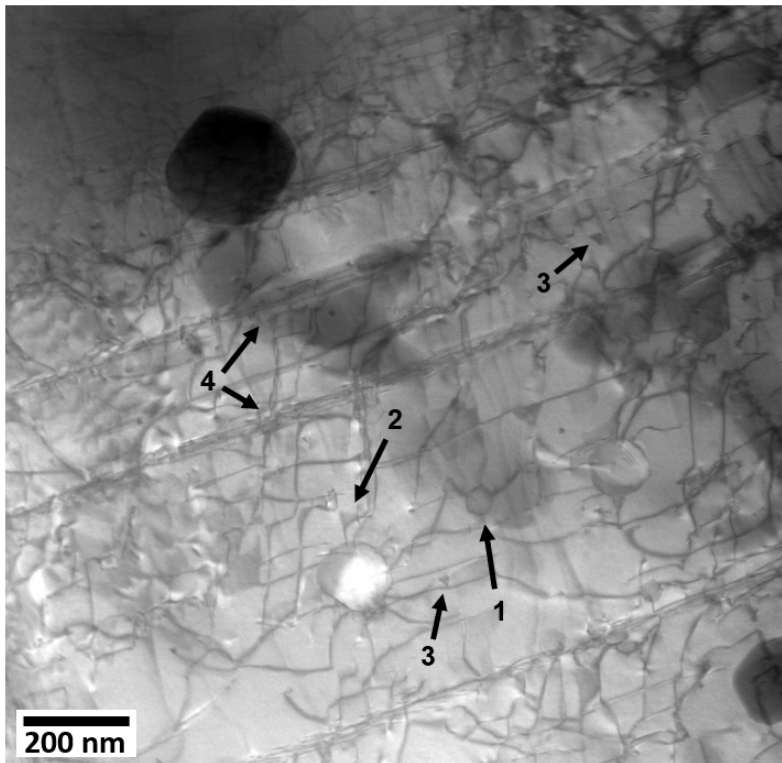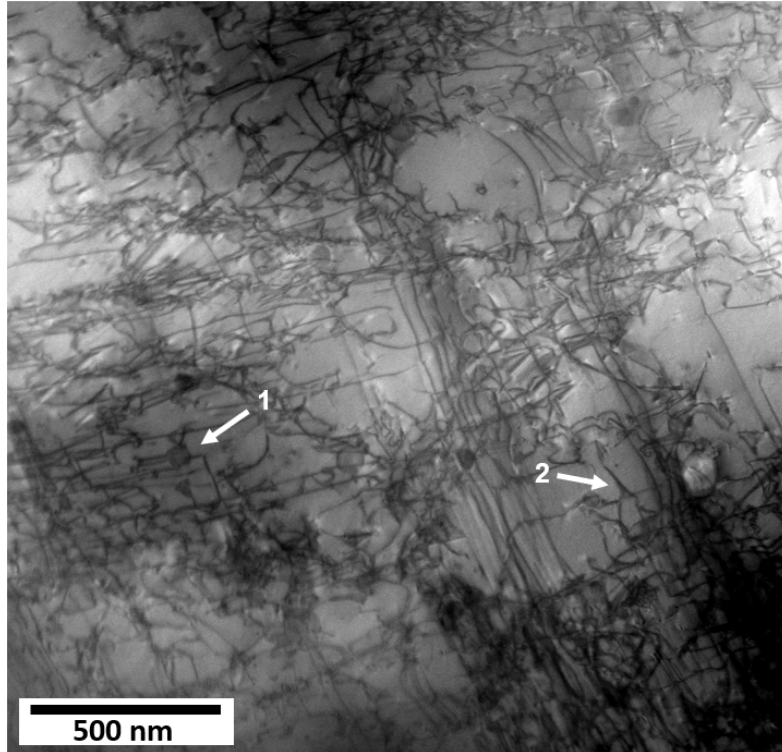
Fig. 3-14 Dislocation structure of AM ODS CrCoNi crept to steady state at 1023 K and 80 MPa showing forest dislocations, dislocation/oxide interactions (arrows 1), extended nodes (arrows 2), SFT (arrows 3), and slip traces (arrows 4).
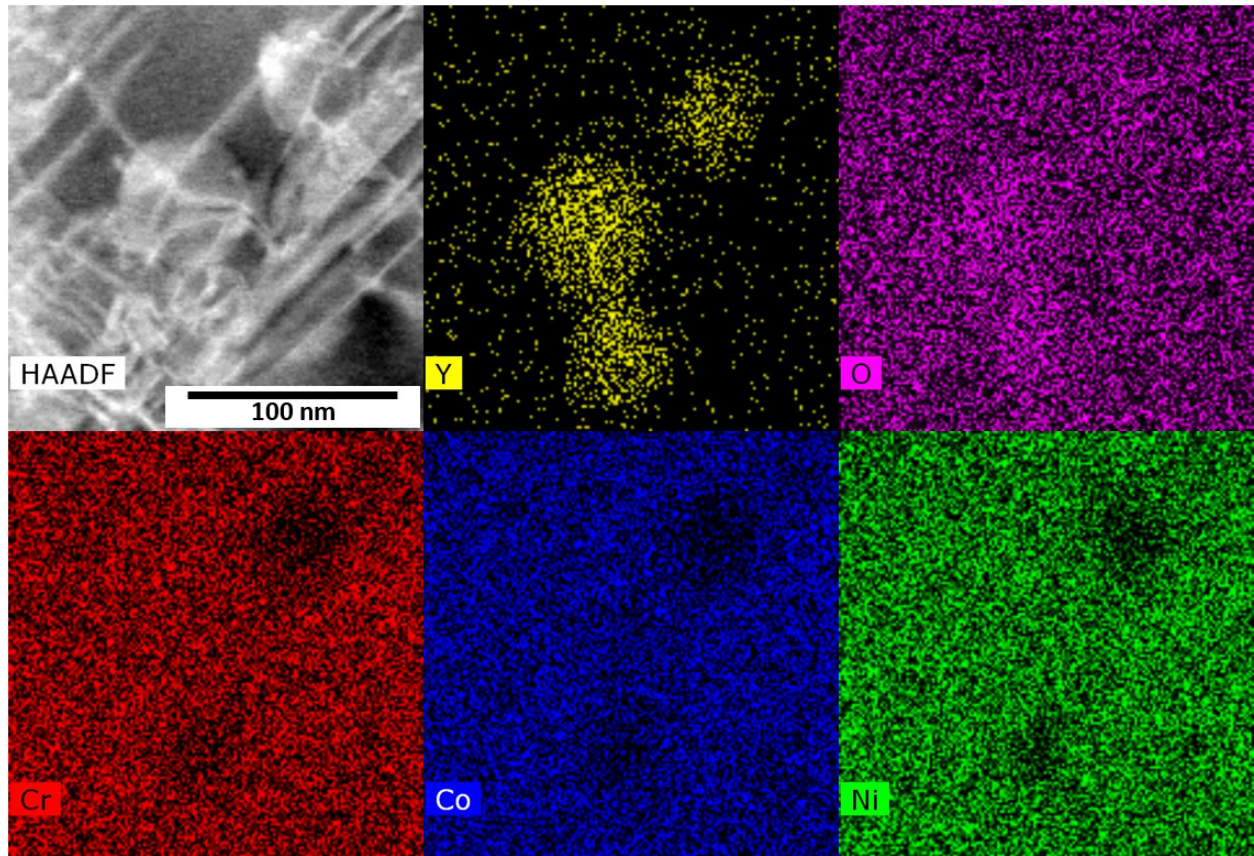
Fig. 3-15 HAADF and STEM-EDS of AM ODS CrCoNi crept to steady state at 1023 K and 80 MPa illustrating dislocation/oxide interactions.
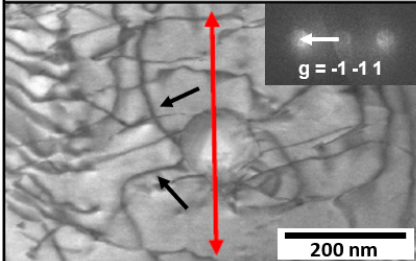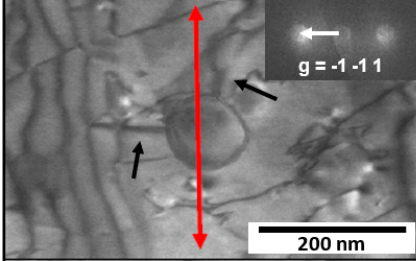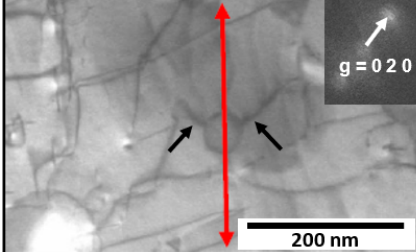
Dislocation/Oxide Interaction	g Vector	Visible or Not Visible	Possible Burgers Vectors
	[1,-1,-1]	Visible	N/A
	[-1,-1,1]	Visible	N/A
	[0,2,0]	Not Visible	[1,0,1], [1,0,-1]
	[2,0,-2]	Visible	N/A
	[-1,3,1]	Not Visible	[1,0,1]
	[-2,2,0]	Visible	N/A
	[-1,3,-1]	Visible	N/A
	[1,-1,-1]	Not Visible	[1,1,0], [1,0,1], [0,1,-1]
	[-1,-1,1]	Visible	N/A
	[0,2,0]	Visible	N/A
	[2,0,-2]	Visible	N/A
	[-1,3,1]	Not Visible	[1,0,1]
	[-2,2,0]	Visible	N/A
	[-1,3,-1]	Visible	N/A
	[1,-1,-1]	Not Visible	[1,0,1], [0,1,1], [1,-1,0]
	[-1,-1,1]	Visible	N/A
	[0,2,0]	Not Visible	[1,0,1]
	[2,0,-2]	Visible	N/A
	[-1,3,1]	Visible	N/A
	[-2,2,0]	Visible	N/A
	[-1,3,-1]	Visible	N/A

Fig. 3-16 g · b analysis of dislocation/oxide interaction dislocations in AM ODS CrCoNi with red arrows representing Burgers vector projections and black arrows pointing to the relevant dislocations on each side of the oxides with which they are interacting.

3.3.4 Post Creep Fracture Characteristics of AM ODS CrCoNi

The creep ductilities of AM ODS CrCoNi over the range of tested applied stresses are shown in Fig. 3-17. The overall average creep ductility of this material was found to be 11.1 ± 5.0%. The large standard deviation associated with this creep ductility stems from a significantly greater value at an applied stress of 200 MPa, shown in Fig. 3-17. For tests at 130 MPa and lower, the average creep ductility is 8.5 ± 2.0% which is slightly higher than the average creep ductility reported for the non-ODS material (7.1 ± 1.2%) tested in the same range of applied stress and temperature [8]. For comparison, the creep ductilities of wrought CrCoNi and Cantor alloy have been reported as 17.6 ± 1.6% and 30.7 ± 2.6%, respectively [7, 8], which reveals that the AM process decreases creep ductility.

Creep ductility is generally related to stress concentrations on GB triple points due to GB sliding, dislocation pile-ups against GBs (Zener-Stroh mechanism), and hard particles on GBs that lead to the nucleation of voids which coalesce and result in intergranular fracture [36-40]. The fracture surface of AM ODS CrCoNi is shown in Fig. 3-18 illustrating the cavities that have nucleated around oxides. The addition of yttria in the AM ODS CrCoNi provides a larger number of hard particles in this material compared to its non-ODS counterpart leading to the expectation that its creep ductility will be lower. This interpretation is supported by a study conducted by Dyson demonstrating that creep ductility decreases as the rate of cavity production increases [41]. However, non-ODS AM CrCoNi has a lower creep ductility than AM ODS CrCoNi [8]. Thus, the higher creep ductility of the AM ODS material can be attributed to the higher percentage of LAGBs that enable easy propagation of deformation across grains and the elongated grains along the loading direction. The higher percentage of LAGBs in the AM ODS material reduces the prevalence of the Zener-Stroh mechanism compared to the non-ODS

material. Since dislocation pile-ups are more likely to propagate deformation through LAGBs, Zener-Stroh induced cavities are less likely to nucleate in the ODS material. Additionally, the elongated grain structure resulted in fewer adjacent transverse grain boundaries making the propagation of transverse cracks more difficult. This effect can be observed in Fig. 3-19, which shows the surface of a fractured AM ODS CrCoNi specimen and illustrates the presence of a highly tortuous intergranular crack path.
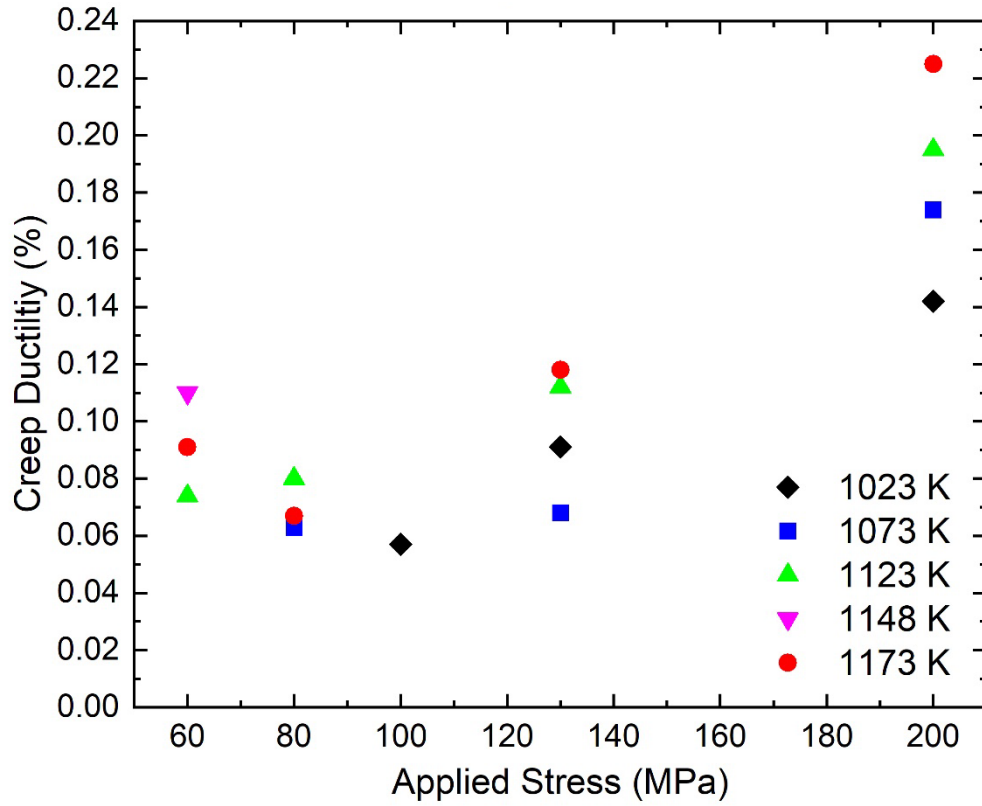
Fig. 3-17 Plot illustrating creep ductility of AM ODS CrCoNi showing an increase at an applied stress of 200 MPa.
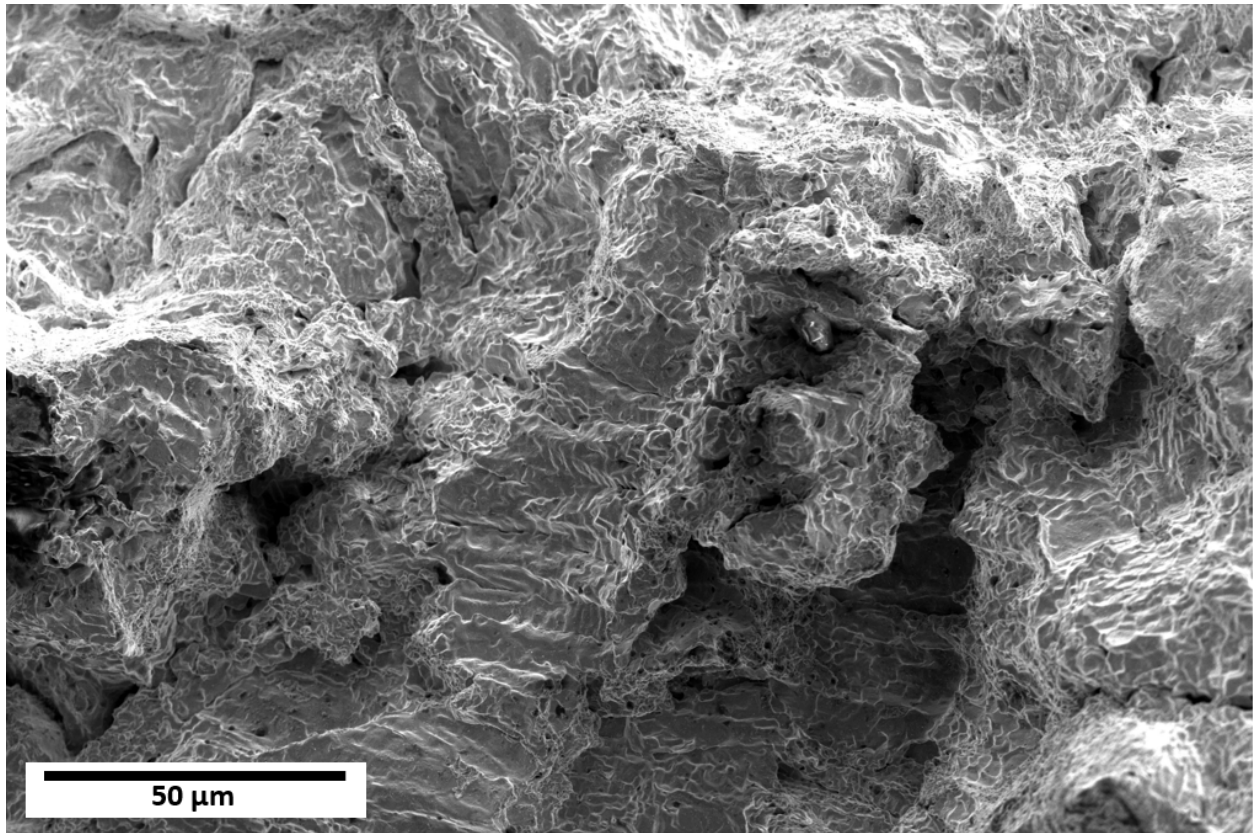
Fig. 3-18 Fracture surfaces of AM ODS CrCoNi following creep rupture at 1023 K and 130 MPa.
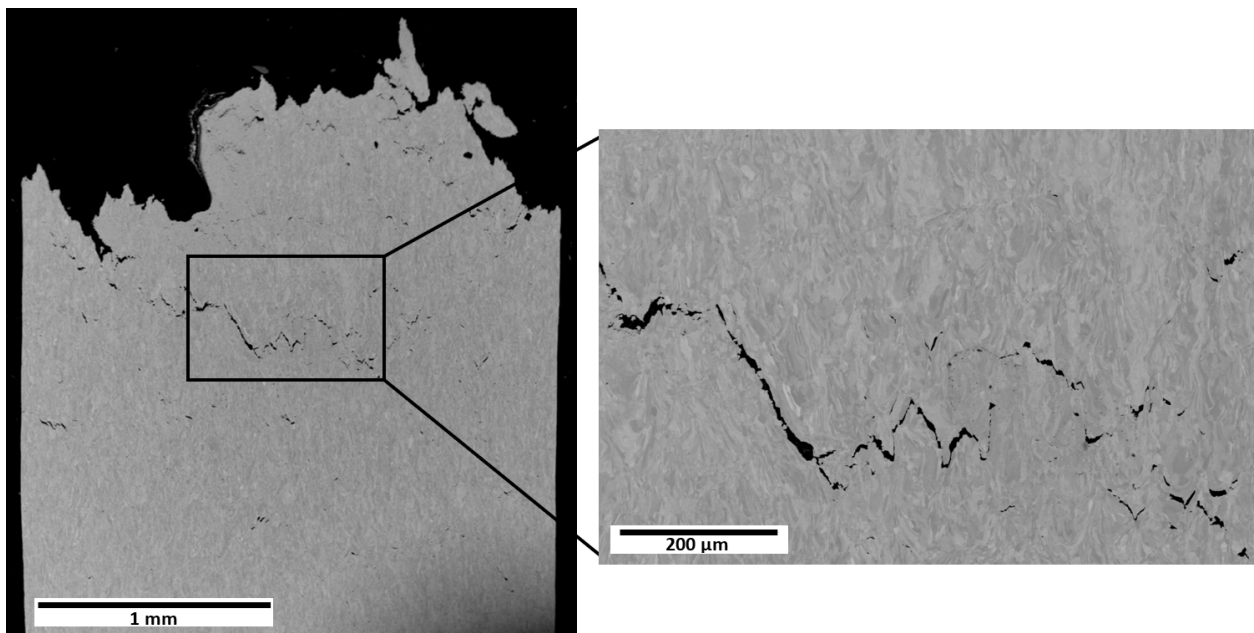
Fig. 3-19 Surface of AM ODS CrCoNi specimen following creep rupture at 1123 K and 80 MPa.

3.4 Conclusions

Constant stress creep tests in the ranges of 1023-1173 K and 60-200 MPa were conducted on an additively manufactured (AM) oxide dispersion strengthened (ODS) CrCoNi multi-principal element alloy to determine its creep behavior. SEM and TEM were used to observe the initial microstructure and dislocation structure, steady state dislocation structure, and fracture surface after rupture to understand the underlying creep deformation mechanisms of this material.

1. A stress exponent of 6.5 ± 0.1 and activation energies in the range of 335-367 kJ/mol were measured. This stress exponent is below the value of 10+ normally associated with ODS materials suggesting the 0.6 vol% of yttria is most likely too low to cause significant dislocation/oxide interactions typical of ODS materials. However, the AM ODS CrCoNi did exhibit an 84% lower steady state creep rate than its non-ODS counterpart at similar stresses and temperatures.

2. The average creep ductility of tests with an applied stress of less than 130 MPa was $8.5 \pm 2.0\%$. Creep ductility is significantly greater at an applied stress of 200 MPa. The yttria and Cr-rich oxides act as cavity nucleation sites leading to void coalescence which is expected to decrease creep ductility while the high percentage of LAGBs allow easy propagation of deformation across grain boundaries avoiding the Zener-Stroh mechanism of cavity formation, which should increase creep ductility. The dynamic balance of these two mechanisms appears to favor the easy propagation of slip across LAGB at the highest applied stress leading to higher ductility.

3. The steady state dislocation structure of AM ODS CrCoNi consists of long arrays of relatively straight dislocations with numerous dislocation/oxide interactions, extended nodes, and SFT. This dislocation structure is significantly different than its non-ODS

counterpart which exhibits individual curved dislocations with dislocation multijunctions and jogs.

Acknowledgements

References

[1]   F. Otto, A. Dlouhy, C. Somsen, H. Bei, G. Eggeler, E.P. George, The influences of temperature and microstructure on the tensile properties of a CoCrFeMnNi high-entropy alloy, Acta Materialia 61 (2013) 5743-5755.

[2]   B. Gludovatz, A. Hohenwarter, K.V.S. Thurston, H. Bei, Z. Wu, E.P. George, R.O. Ritchie, Exceptional damage-tolerance of a medium-entropy alloy CrCoNi at cryogenic temperatures, Nature Communications 7 (2016).

[3]   G. Laplanche, A. Kostka, O.M. Horst, G. Eggeler, E.P. George, Microstructure evolution and critical stress for twinning in the CrMnFeCoNi high-entropy alloy, Acta Materialia 118 (2016) 152-163.

[4]   J. Miao, C.E. Slone, T.M. Smith, C. Niu, H. Bei, M. Ghazisaeidi, G.M. Pharr, M. M.J, The evolution of the deformation substructure in a Ni-Co-Cr equiatomic solid solution alloy, Acta Materialia 132 (2017) 35-48.

[5]   F.D.G. Filho, R.O. Ritchie, M.A. Meyers, M. S.N, Cantor-derived medium-entropy alloys: bridging the gap between traditional metallic and high-entropy alloys, Journal of Materials Research and Technology 17 (2022) 1868-1895.

[6]   Z. Wu, H. Bei, G.M. Pharr, E.P. George, Recovery, recrystallization, grain growth and phase stability of a family of FCC-structured multi-component equiatomic solid solution alloys, Intermetallics 46 (2014) 131-140.

[7]   M. Zhang, E.P. George, J.C. Gibeling, Tensile creep properties of a CrMnFeCoNi high-entropy alloy, Scripta Materialia 194 (2021).

[8] G. Sahragard-Monfared, M. Zhang, T.M. Smith, A.M. Minor, E.P. George, J.C. Gibeling, The influence of processing methods on creep of wrought and additively manufactured CrCoNi multi-principal element alloys, submitted to Acta Materialia.

[9] J.Y. He, H. Wang, H.L. Huang, X.D. Xu, M.W. Chen, Y. Wu, X.J. Liu, T.G. Nieh, K. An, Z.P. Lu, A precipitation-hardened high-entropy alloy with outstanding tensile properties, Acta Materialia 102 (2016) 187-196.

[10] H. Shahmir, M. Nili-Ahmadabadi, A. Shafiee, T.G. Langdon, Effect of a minor titanium addition on the superplastic properties of a CoCrFeNiMn high-entropy alloy processed by high-pressure torsion, Materials Science & Engineering A 718 (2018) 468-476.

[11] Z. Fu, L. Jiang, J.L. Wardini, B. MacDonald, H. Wen, W. Xiong, D. Zhang, Y. Zhou, T.J. Rupert, W. Chen, E.J. Lavernia, A high-entropy alloy with hierarchical nanoprecipitates and ultrahigh strength, Science Advances 4 (2018).

[12] A. Hoffman, L. He, M. Luebbe, H. Pommerenke, J. Duan, P. Cao, K. Sridharan, Z. Lu, H. Wen, Effects of Al and Ti additions on irradiation behavior of FeMnNiCr multi-principal-element alloy, JOM 72 (2020) 150-159.

[13] D.A. Santana, K.R. Santos, C.S. Kiminami, F.G. Coury, Design, phase equilibria, and coarsening kinetics of a new γ/γ' precipitation-hardened multi-principal element alloy, Journal of Alloys and Compounds 882 (2021).

[14] H. Hadraba, Z. Chlup, A. Dlouhy, F. Dobes, P. Roupcova, M. Vilemova, J. Matejicek, Oxide dispersion strengthened CoCrFeNiMn high-entropy alloy, Materials Science & Engineering A 689 (2017) 252-256.

[15] F. Dobes, H. Hadraba, Z. Chlup, A. Dlouhy, M. Vilemova, J. Matejicek, Compressive creep behavior of an oxide-dispersion-strengthened CoCrFeMnNi high-entropy alloy, Mat Sci Eng a-Struct 732 (2018) 99-104.

[16] T.M. Smith, A.C. Thompson, T.P. Gabb, C.L. Bowman, C.A. Kantzos, Efficient production of a high-performance dispersion strengthened, multi-principal element alloy, Scientific Reports (2020).

[17] D. Yang, Y. Liu, N. Qu, T. Han, M. Liao, Z. Lai, J. Zhu, Effect of fabrication methods on microstructures, mechanical properties and strengthening mechanisms of Fe0.25CrNiAl medium-entropy alloy, Journal of Alloys and Compounds 888 (2021).

[18] O.N. Senkov, D.B. Miracle, K.J. Chaput, J. Couzinie, Development and exploration of refractory high entropy alloys—A review, Journal of Materials Research 33(19) (2018) 3092-3128.

[19] C. Liu, C. Gadelmeier, S. Lu, J. Yeh, H. Yen, S. Gorsse, U. Glatzel, A. Yeh, Tensile creep behavior of HfNbTaTiZr refractory high entropy alloy at elevated temperatures, Acta Materialia 237 (2022).

[20] C. Gadelmeier, Y. Yang, U. Glatzel, E.P. George, Creep strength of refractory high-entropy alloy TiZrHfNbTa and comparison with Ni-base superalloy CMSX-4, Cell Reports Physical Science 3(8) (2022).

[21] P. Kumar, S.J. Kim, Q. Yu, J. Ell, M. Zhang, Y. Yang, J.Y. Kim, H.-K. Park, A.M. Minor, E.S. Park, R.O. Ritchie, Compressive vs. tensile yield and fracture toughness behavior of a body-centered cubic refractory high-entropy superalloy Al0.5Nb1.25Ta1.25TiZr at temperatures from ambient to 1200°C, Acta Materialia 245 (2023).

[22] S.E. Broyles, M. Zhang, J.C. Gibeling, Influence of annealing on the creep behavior of GlidCop Al-15, Materials Science & Engineering A 779 (2020).

[23] M.W. Decker, J.R. Groza, J.C. Gibeling, Creep properties of an extruded copper-8% chromium-4% niobium alloy, Mat Sci Eng a-Struct 369(1-2) (2004) 101-111.

[24] C.E. Slone, J. Miao, E.P. George, M.J. Mills, Achieving ultra-high strength and ductility in equiatomic CrCoNi with partially recrystallized microstructures, Acta Materialia 165(15) (2019) 496-507.

[25] S. Liu, D. Wan, S. Guan, Y. Fu, X. Ren, Z. Zhang, J. He, Microstructure and nanomechanical behavior of an additively manufactured (CrCoNiFe)94Ti2Al4 high-entropy alloy, Materials Science & Engineering A 823(17) (2021).

[26] G.D. Sathiaraj, W. Skrotzki, A. Pukenas, R. Schaarschuch, R.J. Immanuel, S.K. Panigrahl, J.A. Chelvan, S.S.S. Kumar, Effect of annealing on the microstructure and texture of cold rolled CrCoNi medium-entropy alloy, Intermetallics 101 (2018) 87-98.

[27] M. Schneider, E.P. George, T.J. Manescau, T. Zalezak, J. Hunfeld, A. Dlouhy, G. Eggeler, G. Laplanche, Analysis of strengthening due to grain boundaries and annealing twin boundaries in the CrCoNi medium-entropy alloy, International Journal of Plasticity 124 (2020) 155-169.

[28] O.D. Sherby, P.M. Burke, Mechanical behavior of crystalline solids at elevated temperature, Progress in Materials Science 13 (1968) 323-390.

[29] V.C. Nardone, J.K. Tien, On the creep rate stress dependence of particle strengthened alloys, Scripta Metallurgica 20 (1986) 797-802.

[30] S.E. Broyles, K.R. Anderson, J.R. Groza, J.C. Gibeling, Creep deformation of dispersion-strengthened copper, Metallurgical and Materials Transactions A 27 (1996) 1217-1227.

[31] R.W. Lund, W.D. Nix, High temperature creep of Ni-20Cr-2ThO2 single crystals, Acta Metallurgica 24(5) (1976) 469-481.

[32] S. Chen, Q. Yu, The role of low angle grain boundary in deformation of titanium and its size effect, Scripta Materialia 163 (2019) 148-151.

[33] F. Habiyaremye, A. Guitton, F. Schafer, F. Scholz, M. Schneider, J. Frenzel, G. Laplanche, N. Maloufi, Plasticity induced by nanoindentation in a CrCoNi medium-entropy alloy studied by accurate electron channeling contrast imaging revealing dislocation-low angle grain boundary interactions, Materials Science & Engineering A 817 (2021).

[34] G. Laplanche, A. Kostka, C. Reinhart, J. Hunfeld, G. Eggele, E.P. George, Reasons for the superior mechanical properties of medium-entropy CrCoNi compared to high-entropy CrMnFeCoNi, Acta Materialia 128 (2017) 292-303.

[35] J. Silcox, P.B. Hirsch, Direct observations of defects in quenched gold, Philos Mag 4(37) (1959) 72-89.

[36] F.A. McClintok, A criterion for ductile fracture by the growth of holes, Journal of Applied Mechanics 35(2) (1968) 363-371.

[37] R. Lombard, H. Vehoff, Nucleation and growth of cavities at defined grain boundaries in bicrystals, Scripta Metallurgica 24(3) (1990) 581-586.

[38] E.P. George, R.L. Kennedy, D.P. Pope, Review of trace element effects on high-temperature fracture of Fe- and Ni-base alloys, Physica Status Solidi A 167(2) (1998) 313-333.

[39] Y.S. Lee, J. Yu, Effect of matrix hardness on the creep properties of a 12CrMoVNb steel, Metallurgical and Materials Transactions A 30A (1999) 2331-2339.

[40] M.E. Kassner, T.A. Hayes, Creep cavitation in metals, International Journal of Plasticity 19(10) (2003) 1715-1748.

[41]   B.F. Dyson, Continuous cavity nucleation and creep fracture, Scripta Metallurgica 17(1) (1983) 31-37.

Chapter 4. Creep Deformation Mechanisms of an Additively Manufactured

Oxide Dispersion Strengthened CrCoNi Multi-Principal Element Alloy[3]

4.1 Introduction

The recent development of multi-principal element alloys (MPEA) has expanded the potential

design space of alloys for high temperature applications [1-3]. Although several high

temperature tensile creep studies of MPEAs have been performed, a consensus regarding the

underlying mechanisms of steady state creep deformation in MPEAs has not been reached. When

applied to high temperature deformation, the thermally-activated dislocation glide model

described by Kocks, Argon, and Ashby shown in Eq. 4.1 indicates that the thermal release of

glide dislocations from obstacles controls the creep rate, $\dot{\varepsilon}$ [4].

$$\dot{\varepsilon} = \dot{\varepsilon}_0 \exp\left[-\frac{\Delta G}{RT}\right]_{\hat{\sigma}} \tag{4.1}$$

where $\dot{\varepsilon}_0$ is a pre-exponential constant, R is the gas constant, T is temperature, and ΔG is the

Gibbs free energy of activation which is a function of the applied stress and the maximum glide

resistance provided by the microstructure, represented here by the structure parameter $\hat{\sigma}$. The

concepts inherent in this model can be used in conjunction with stress reduction creep tests

performed at constant temperature to probe the mechanisms controlling steady state creep. The

success of this approach is contingent on the microstructure remaining constant before and after

the stress reduction to avoid any change in strain rate resulting from microstructural evolution.

Utilizing this framework, Zhang, et al. conducted stress reduction tests to investigate the high

temperature steady state tensile creep deformation of wrought CrMnFeCoNi (Cantor alloy) and

found the rate controlling mechanism to be a combination of solid solution strengthening and

---

[3] To be submitted as G. Sahragard-Monfared, T. M. Smith, and J. C. Gibeling. Scripta Materialia. (2023)

forest dislocation strengthening [5]. Similarly, Dobeš, et al. examined the high temperature compressive creep behavior of spark plasma sintered Cantor alloy and determined that forest dislocation strengthening is the sole rate controlling mechanism, however, this study was based only on steady state creep rates obtained from high temperature uniaxial compression tests and did not utilize the concept of constant structure [6].

Recent efforts to improve the high temperature strength of MPEAs have led to studies on the effect of oxide dispersion strengthening (ODS) on high temperature mechanical properties of MPEAs [6, 7]. Sahragard-Monfared, et al. and Dobeš, et al. have found that oxide dispersion strengthening of MPEAs significantly increases creep resistance [6, 7]. However, the mechanisms controlling steady state creep of oxide dispersion strengthened MPEAs, as revealed through the high temperature operational activation area, have not yet been investigated. Therefore, this study examines how oxide dispersion strengthening affects the mechanisms controlling steady state creep in MPEAs while also being the first study to measure the operational activation area and consequently determine the rate controlling mechanisms of steady state creep of additively manufactured (AM) CrCoNi and AM ODS CrCoNi MPEAs.

4.2 Experimental Methods

The AM CrCoNi and AM ODS CrCoNi alloys were fabricated by laser powder bed fusion (L-PBF) of pre-alloyed equiatomic CrCoNi powder with diameters ranging between 10-45 μm. An addition of 1 wt% of Y_2O_3 powder with diameters ranging between 100-200 nm was acoustically mixed with the CrCoNi powder to make the AM ODS CrCoNi, as described by Smith, et al. [8]. The final material contains approximately 0.6 vol% Y_2O_3 [8]. After L-PBF, the builds were subsequently HIPed at 1458 K to relieve residual stress, remove defects caused from the AM process, and form a more equiaxed grain structure. Tensile creep specimens with gage

dimensions of 19.05 (L) x 2.54(W) x 0.60(T) mm were electrical discharge machined from the build such that their creep tensile axis is parallel to the build direction. The same specimen dimensions were used in the Zhang, et al. Cantor alloy study [5]. The gage section surfaces and edges were polished using 600 grit SiC paper to reduce the risk of surface defects influencing creep properties. Grain sizes of these MPEAs have been reported in previous studies [7, 9]. The AM CrCoNi grains are slightly elongated in the build direction with an aspect ratio of approximately 1.8:1 such that the grain size is 74.3 ± 2.6 μm parallel to the tensile (build) direction and 41.4 ± 2.4 μm perpendicular to the tensile direction. Grains of the AM ODS CrCoNi are more elongated in the build direction with an aspect ratio of approximately 4:1 such that the grain size is 23.8 ± 1.8 μm parallel to the tensile (build) axis and 6.5 ± 1.8 μm perpendicular to the tensile axis.

Stress reduction tensile creep tests were performed on a constant stress testing system utilizing an Andrade-Chalmers lever arm and under vacuum of less than 2×10^{-5} torr to avoid oxidation following the procedures and using the system described in more detail by Broyles and Gibeling [10] and Zhang, et al. [5]. Tests were performed at a temperature of 1073 K and an initial stress of 130 MPa with stress reductions to 100, 80, and 60 MPa. Creep strain was measured using a Schaevitz 250 MHR linear variable differential transformer in conjunction with a custom quartz tube and rod inside the furnace mounted to the specimen grips as described by Mills, et al. [11]. The resolution of the measurement system used is 0.02 seconds and 8×10^{-8} for time and strain, respectively. Stress reductions were performed after steady state creep had been reached by quickly removing a portion of the applied load from the Andrade-Chalmers lever arm in order to probe the constant structure creep rate and thus determine the mechanisms controlling creep.

4.3 Results and Discussion

Creep curves following stress reductions from 130 MPa to 100 MPa are illustrated in Fig. 4-1 for both materials. It is noted that the creep ductility of AM ODS CrCoNi tested in this study is significantly lower than reported in a previous study [7] due to an AM process control issue that led to a reduction in the density of the builds used in this work. However, steady state creep rates obtained in this study are comparable to those previously published [7]. Since the stress reductions were conducted at the relatively small strains needed to reach steady state creep, the low ductility of this material is not of concern here. Three relevant creep rates are identified following the notation used by Biberger and Gibeling to describe the creep rates before and after the stress reduction [12]. The creep rate denoted $\dot{\varepsilon}_A$ is representative of the steady state creep rate before the stress reduction. Immediately after the stress reduction, a period of apparent zero creep rate is observed due to the simultaneous anelastic backflow caused by the stress reduction and the continued forward flow under the reduced stress [13]. The interval during which backflow occurs is not directly relevant to the study of constant structure creep, however, it has been reported in pure metals, conventional alloys, and oxide dispersion strengthened alloys with the anelastic backflow being attributed to either the unbowing of dislocations or the relaxation of grain/subgrain boundary dislocation pile ups due to the stress reduction [13-17]. Previous studies by Sahragard-Monfared, et al. have shown that the materials examined in this work do not form subgrains and, although dislocation pile ups at grain boundaries have been observed, they are not widely prevalent [7, 9]. Therefore, the anelastic backflow in these materials can be attributed to the unbowing of pinned dislocations. The creep rate denoted $\dot{\varepsilon}_C$ is representative of the creep rate immediately after the region of apparent zero creep rate and is identified as the constant structure creep rate because the dislocation structure where this rate is measured is similar to the

97

dislocation structure before the stress reduction [18, 19]. Finally, $\dot{\varepsilon}_D$ is the creep rate of the

second steady state under the action of the reduced stress.
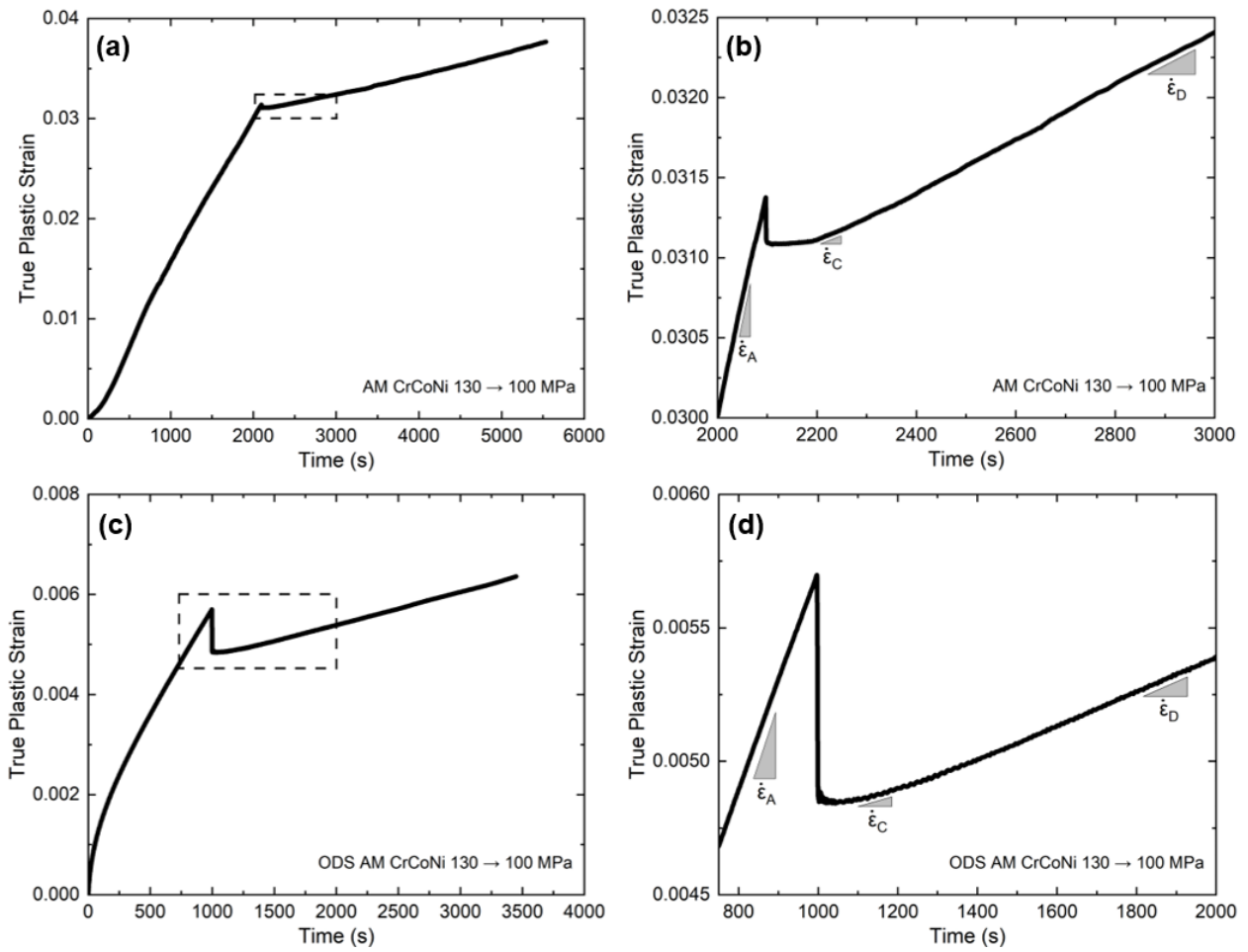
Fig. 4-1 Stress reduction creep curves for a stress reduction of 130 MPa to 100 MPa for (a,b) AM CrCoNi and (c,d) AM ODS CrCoNi.

Fig. 4-2 shows the stress reduction creep curves for a large stress reduction from 130 MPa to 60 MPa for both materials. Unlike the curves in Fig. 4-1, continuous deceleration of the creep rate is observed after the period of apparent zero creep rate. This behavior has been described previously for solid solution strengthened alloys and dispersion strengthened alloys and is attributed to the inability of the mobile dislocation density to adjust to an appropriate value for the reduced stress due to dislocation pinning by solute atoms and oxides [20, 21]. The constant structure creep rate that occurs after the stress reduction is caused by mobile dislocations moving while all other aspects of the microstructure are assumed to remain constant. The presence of solute atoms and oxides limits the mobility of these dislocations. It is noted that this behavior is also observed for pure metals, with the initial forward creep rate after the stress reduction being termed the anomalous creep rate due to microstructural observations showing significant changes in the dislocation density prior to this region such that it does not correspond to a constant dislocation structure [18, 19, 22]. Instead, the constant structure creep rate in the case of large stress reductions in pure metals occurs once the deceleration of the creep rate ends before continuing to accelerate to a second steady state [18, 23-25]. However, this description is strictly correct for subgrain forming materials and AM CrCoNi and AM ODS CrCoNi do not form subgrains. Therefore, the deceleration of the creep rate in these materials after large stress reductions is attributed to dislocations being pinned by solute atoms and oxides and thus hindering the adjustment of the mobile dislocation density to the reduced stress. It is inferred that the volume fraction of oxides in these alloys is so low that after small stress reductions the oxides do not hinder the adjustment of the mobile dislocation density. Conversely, the volume fraction of oxides is sufficiently large that they hinder the adjustment of the mobile dislocation density at the low reduced stress after large stress reductions. This explanation is consistent with

other studies of dispersion strengthened alloys in which the volume fraction of oxides is

relatively high, and a decreasing creep rate is observed (similar to Fig. 4-2) for both small and

large stress reductions [17, 21].
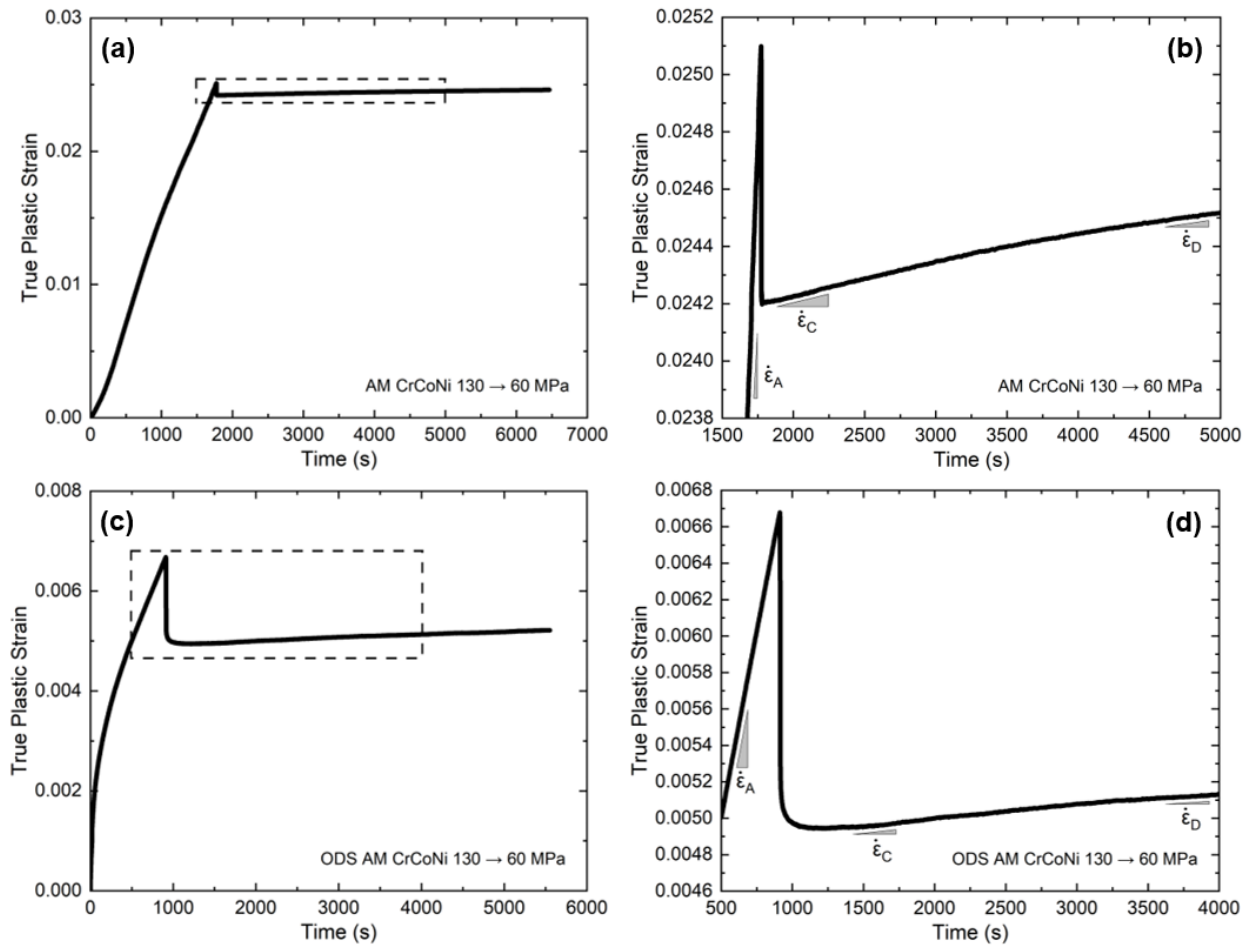
Fig. 4-2 Stress reduction creep curves for a stress reduction of 130 MPa to 60 MPa for (a,b) AM CrCoNi and (c,d) AM ODS CrCoNi.

The importance of the constant structure creep rate is that it can be used to determine the operational activation area, $\Delta a''$, which quantifies the area swept by dislocations during activation events and therefore reveals the mechanism controlling steady state creep. Values of $\Delta a'' \approx 1 - 10\ b^2$ have been reported for alloys in which lattice friction and diffusive processes are rate controlling [26, 27]. For alloys in which the rate controlling mechanism is dislocation interactions with solutes, values of $\Delta a'' \approx 100\ b^2$ have been reported and scale inversely with the concentration of solute in the matrix [5, 28]. For dispersion strengthened alloys, values of $\Delta a'' \approx 320 - 455\ b^2$ have been reported [17]. Values of $\Delta a'' \approx 100 - 1000\ b^2$ have been reported for alloys in which forest dislocations are rate controlling, with this value scaling inversely with applied stress [29, 30]. The value(s) of $\Delta a''$ must be determined under constant dislocation structure governed by features such as forest dislocation spacing, particle spacing, and subgrain size. This is necessary because the partial derivative of the logarithmic strain rate with respect to applied stress must be evaluated at constant temperature and structure as shown in Eq. 4.2.

$$\Delta a'' = \left[\frac{Mk_BT}{b}\right] \cdot \left[\frac{\partial ln\dot{\varepsilon}_C}{\partial \sigma}\right]_{T,\hat{\sigma}} \tag{4.2}$$

Here, $\Delta a''$ is dependent on the Taylor factor, M, which is 3.06 for an FCC crystal structure, the Boltzmann constant, k_B, the temperature, T, the Burgers vector, b, which has been reported as 0.146 nm for equiatomic CrCoNi [31], and the partial derivative of the semi-logarithmic constant structure strain rate, $\dot{\varepsilon}_C$, with respect to applied stress, σ, evaluated at constant temperature and structure, $\hat{\sigma}$. Fig. 4-3 illustrates the partial derivative of $ln\dot{\varepsilon}_C$ with respect to σ, evaluated at 1073 K for the two materials studied in this investigation. These slopes along with the previously mentioned constants were used with Eq. 4.2 to calculate $\Delta a''$ of 900 b^2 for AM ODS CrCoNi and 940 b^2 for AM CrCoNi.
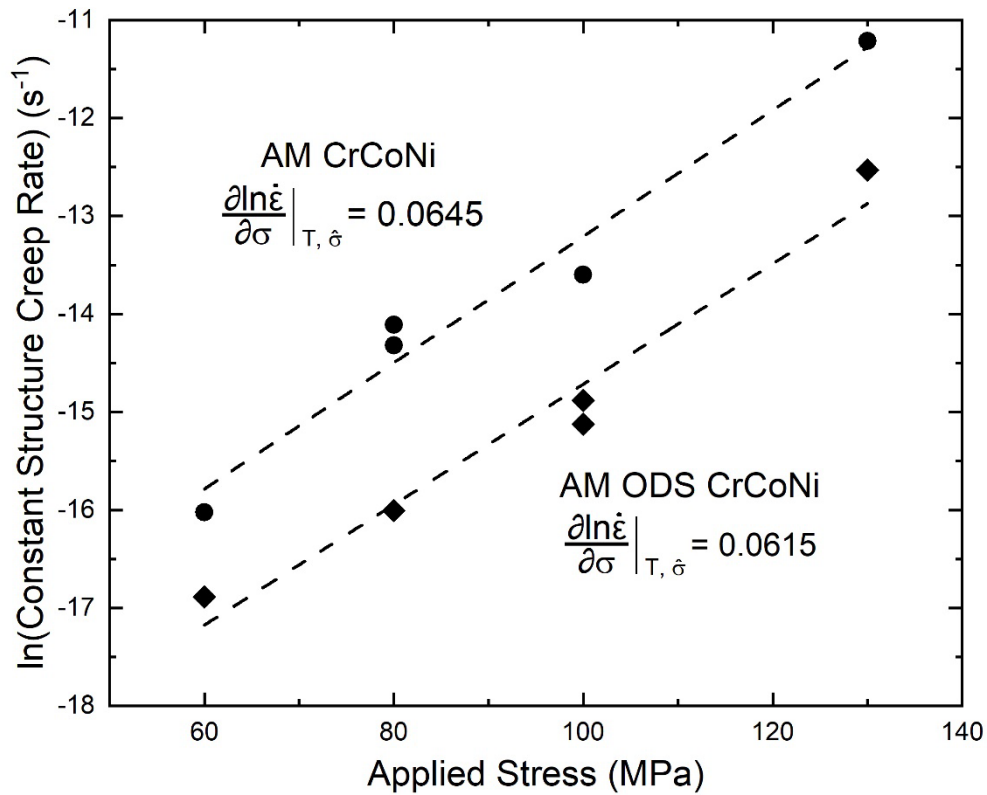
Fig. 4-3 Natural logarithm of constant structure strain rate ($ln\dot{\varepsilon}_C$) versus applied stress (σ) at 1073 K for AM CrCoNi and AM ODS CrCoNi. Data points at 130 MPa are an average of the steady state creep rates immediately before the stress reductions.

The operational activation areas calculated in this study are consistent with steady state creep dislocation structures observed for these alloys [7, 9]. These dislocation structures included multijunctions which are associated with dislocation bowing from forest dislocations and oxides. Despite the addition of 0.6 vol% yttria and the observation of dislocation/oxide interactions, the steady state creep of AM ODS CrCoNi is governed by the same forest dislocation rate controlling mechanism as its non-ODS counterpart. This reveals that the process of overcoming particles is relatively easy in the ODS material due to its low volume fraction of oxides and thus forest dislocation interactions are rate limiting. However, as reported by Sahragard-Monfared, et al. [7, 9] the steady state creep rates of AM ODS CrCoNi are lower than AM CrCoNi at similar temperatures and applied stresses. Because the rate controlling creep mechanisms are the same in these alloys, the rate of activation is the same at any given stress and temperature. The larger volume fraction of oxides in the ODS material results is a smaller area being swept by dislocations per activation event resulting in a smaller amount of strain per event and thus a lower steady state creep rate. This perspective is consistent with the different forms of creep transients following stress reductions of small and large magnitudes.

As noted earlier, Zhang, et al. and Dobeš, et al. reported slightly different mechanisms controlling steady state creep of the Cantor alloy. Zhang, et al. reported a combination of dislocation/solute interactions and forest dislocations interactions with the former contributing the majority of the creep strength while Dobeš, et al. reported forest dislocation strengthening as the only mechanism controlling steady state creep of the Cantor alloy [5, 6]. However, it is noted that when the values of activation volume reported by Dobeš, et al. are converted to $\Delta a''$ ($45 - 86\ b^2$) they align with the values of Zhang, et al. ($114 - 153\ b^2$) and are in the range typically

characteristic of dislocation/solute interactions. This comparison to the Cantor alloy implies that the simplification of the matrix from the quinary alloy to the ternary alloy changes the mechanism controlling steady state creep from being dominated by solid solution strengthening to being dominated by forest dislocation strengthening. Due to the inverse additive nature of activation areas, it can be inferred that the solute effect only contributes minimally to the creep behavior of the ternary alloy.

A difference in composition is not the only relevant comparison between the CrCoNi alloys investigated in this study and the Cantor alloy values reported by Zhang, et al. and Dobeš, et al. It is also important to determine how differences in processing methods affected the constant structure behavior. As reported by Sahragard-Monfared, et al. [9] the AM process introduced Cr-rich oxides into AM CrCoNi, these Cr-rich oxides were also observed alongside yttria in AM ODS CrCoNi [7]. Broyles and Gibeling utilized the results of tensile stress reduction tests in the framework of the Rösler and Artz model and reported that the constant structure creep behavior of ODS copper is controlled by dislocation/oxide interactions [21, 32]. Zhang, et al. continued the work of Broyles and Gibeling and measured operational activation areas ranging from 320 – 455 b^2 for various ODS copper alloys which is consistent with detachment-controlled glide [17]. Zhang, et al. also reported that for ODS alloys it is not the volume fraction of oxides, but instead the oxide size that governs the detachment process [17]. The Cr-rich oxides and yttria in AM CrCoNi and AM ODS CrCoNi both have approximately 100 nm diameters indicating that the dislocation segment sizes detaching from oxides are comparable in both materials and thus contribute similarly to the creep behavior [7, 9]. However, as previously stated, activation areas are inversely additive, therefore dislocation detachment from particles due to oxide dispersion strengthening in AM CrCoNi and AM ODS CrCoNi does not affect the creep behavior of these

alloys as significantly as forest dislocation strengthening. Furthermore, the lack of downward curvature toward a threshold in the log-log plot of steady state strain rate versus applied stress for these alloys as shown in previous work [7, 9] implies that dislocation climb over particles is not rate controlling, although dislocation/oxide interactions were observed. Additionally, the transients following stress reductions in the work of Zhang, et al. and Broyles and Gibeling were observed to be similar to solid solution strengthened alloys which has also been observed in this study for large stress reductions in AM CrCoNi and AM ODS CrCoNi [17, 21]. This observation implies that, as previously described, the volume fraction of oxides in these alloys is so low that there exists a stress reduction limit above which the mobile dislocation density is able to adjust to the reduced stress and below which the mobile dislocation density is unable to adequately adjust due to dislocation pinning by solute atoms and oxides.

4.4 Conclusions

Stress reduction creep tests were performed on AM CrCoNi and AM ODS CrCoNi to probe creep mechanisms as revealed through operational activation areas ($\Delta a''$) at 1073 K.

1. Values of $\Delta a'' = 900 \, b^2$ and $\Delta a'' = 940 \, b^2$ were determined for AM ODS CrCoNi and AM CrCoNi, respectively. These $\Delta a''$ values indicate that forest dislocation interactions control steady state creep deformation in these alloys.

2. Simplifying the composition from CrMnFeCoNi to CrCoNi results in a change from solute/dislocation interaction dominated to forest dislocation controlled steady state creep at 1073 K.

3. The operational activation areas of both materials are nearly identical revealing that the addition of 0.6 vol% yttria does not affect the mechanism controlling the rate of thermally activated dislocation glide during steady state creep in this alloy. However, the

lower steady state creep rates of AM ODS CrCoNi are due to the higher volume fraction

of particles limiting the area swept by gliding dislocations resulting in less strain per

activation event.

4. Large stress reductions in AM CrCoNi and AM ODS CrCoNi result in continuously

decreasing creep rates while smaller stress reductions result in creep rates that increase

until fracture. This behavior suggests that there is a stress reduction limit above which the

mobile dislocation density is prevented from adjusting to the reduced stress due to

dislocation/oxide interactions.

References

[1]   D.B. Miracle, O.N. Senkov, A critical review of high entropy alloys and related concepts, Acta Materialia 122 (2017) 448-511.

[2]   F.G. Coury, G. Zepon, C. Bolfarini, Multi-principal element alloys from the CrCoNi family: outlook and perspectives, J Mater Res Technol 15 (2021) 3461-3480.

[3]   Y. Chen, B.B. Xie, B. Liu, Y.K. Cao, J. Li, Q.H. Fang, P.K. Liaw, A focused review on engineering application of multi-principal element alloy, Front Mater 8 (2022).

[4]   U.F. Kocks, A.S. Argon, M.F. Ashby, Thermodynamics and kinetics of slip, Progress in Materials Science 19 (1975).

[5]   M. Zhang, E.P. George, J.C. Gibeling, Elevated-temperature deformation mechanisms in a CrMnFeCoNi high-entropy alloy, Acta Materialia 218 (2021).

[6]   F. Dobeš, H. Hadraba, Z. Chlup, A. Dlouhý, M. Vilémová, J. Matějíček, Compressive creep behavior of an oxide-dispersion-strengthened CoCrFeMnNi high-entropy alloy, Materials Science and Engineering: A 732 (2018) 99-104.

[7]   G. Sahragard-Monfared, M. Zhang, T.M. Smith, A.M. Minor, J.C. Gibeling, Superior tensile creep behavior of a novel oxide dispersion strengthened CrCoNi multi-principal element alloy, submitted to Acta Materialia.

[8]   T.M. Smith, A.C. Thompson, T.P. Gabb, C.L. Bowman, C.A. Kantzos, Efficient production of a high-performance dispersion strengthened, multi-principal element alloy, Scientific Reports (2020).

[9]   G. Sahragard-Monfared, M. Zhang, T.M. Smith, A.M. Minor, E.P. George, J.C. Gibeling, The influence of processing methods on creep of wrought and additively manufactured CrCoNi multi-principal element alloys, submitted to Acta Materialia.

[10]   S.E. Broyles, J.C. Gibeling, Constant structure creep of copper at 973K, Scripta Metallurgica et Materialia 33(5) (1995) 767-772.

[11]   M.J. Mills, J.C. Gibeling, W.D. Nix, A dislocation loop model for creep of solid-solutions based on the steady-state and transient creep-properties of A1-5.5 at percent-Mg, Acta Metall 33(8) (1985) 1503-1514.

[12]   M. Biberger, J.C. Gibeling, Analysis of creep transients in pure metals following stress changes, Acta Metallurgica et Materialia 43(9) (1995) 3247-3260.

[13]   J.C. Gibeling, W.D. Nix, Observations of anelastic backflow following stress reductions during creep of pure metals, Acta Metall 29(10) (1981) 1769-1784.

[14]   G.J. Lloyd, R.J. McElroy, A model for the quantitative interpretation of high-temperature stress relaxation phenomena The effect of anelasticity, The Philosophical Magazine: A Journal of Theoretical Experimental and Applied Physics 32(1) (1975) 231-244.

[15]   L.O. Bueno, R.L. Bell, Anelastic creep behaviour of RR-58 aluminum alloy at 180°C: Phenomenological aspects and analysis based on the unbowing of dislocation segments, Materials Science and Engineering: A 410-411 (2005) 72-78.

[16]   F. Mompiou, D. Caillard, M. Legros, H. Mughrabi, In situ TEM observations of reverse dislocation motion upon unloading in tensile-deformed UFG aluminium, Acta Materialia 60(8) (2012) 3402-3414.

[17]   M. Zhang, S.E. Broyles, J.C. Gibeling, An improved description of creep in dispersion-strengthened metals, Acta Materialia 196 (2020) 384-395.

[18]   O.D. Sherby, R.H. Klundt, A.K. Miller, Flow stress, subgrain size, and subgrain stability at elevated temperature, Metallurgical Transactions A 8 (1977) 843-850.

[19]   W. Muller, M. Biberger, W. Blum, Subgrain-boundary migration during creep of Lif .3. stress reduction experiments, Philos Mag A 66(5) (1992) 717-728.

[20]   O.D. Sherby, T.A. Trozera, J.E. Dorn, Effects of creep stress history at high temperatures on the creep of aluminum alloys, In Proc. ASTM 56 (1956) 789-806.

[21]   S.E. Broyles, J.C. Gibeling, Constant structure creep studies of dispersion-strengthened copper, Johannes Weertman Symposium (1996) 93-101.

[22]   W. Blum, E. Weckert, On the interpretation of the internal-stress determined from dip tests during creep of Al-5at percent-Mg, Mater Sci Eng 86 (1987) 145-158.

[23]   J.C. Gibeling, W.D. Nix, Anomalous and constant substructure creep transients in pure aluminum, in: R.C. Gifkins (Ed.), International Conference on the Strength of Metals and Alloys (ICSMA 6), Pergamon Press, Oxford, 1982, pp. 613-618.

[24]   G.S. Nakayama, J.C. Gibeling, Creep of copper under constant structure conditions, Scripta Metallurgica et Materialia 24(11) (1990) 2031-2035.

[25]   G.S. Nakayama, J.C. Gibeling, Experimental investigation of the kinetic law for high-temperature deformation, Modeling the Deformation of Crystalline Solids (1991) 589-600.

[26]   O.D. Sherby, J.L. Robbins, A. Goldberg, Calculation of activation volumes for self-diffusion and creep at high temperature, J Appl Physi 41(10) (1970) 3961-3968.

[27]   M.Z. Butt, Kinetics of flow stress in crystals with high intrinsic lattice friction, Philosophical Magazine 87(24) (2007) 3595-3614.

[28]   B.J. Diak, S. Saimoto, The determination of solute clusters in dilute aluminum alloys using strain rate sensitivity, Materials Science and Engineering: A 234-236 (1997) 1019-1022.

[29]   Z.S. Basinski, Thermally activated glide in face-centred cubic metals and its application to the theory of strain hardening, The Philosophical Magazine: A Journal of Theoretical Experimental and Applied Physics 4(40) (1959) 393-432.

[30]   G.S. Murthy, D.H. Sastry, Impression creep of zinc and the rate-controlling dislocation mechanism of plastic-flow at high-temperatures, Phys Status Solidi A 70(1) (1982) 63-71.

[31]   G. Laplanche, A. Kostka, C. Reinhart, J. Hunfeld, G. Eggele, E.P. George, Reasons for the superior mechanical properties of medium-entropy CrCoNi compared to high-entropy CrMnFeCoNi, Acta Materialia 128 (2017) 292-303.

[32]   J. Rösler, E. Arzt, A new model-based creep equation for dispersion strengthened materials, Acta Metallurgica et Materialia 38(4) (1990) 671-683.

Chapter 5. Excellent High Stress Tensile Creep Behavior of the Refractory Multi-Principal Element Alloy Nb$_{45}$Ta$_{25}$Ti$_{15}$Hf$_{15}$[4]

5.1 Introduction

Multi-principal element alloys (MPEA) are composed of three to five elements, typically with a minimum threshold of 10 at% of each element. MPEAs have been of interest to the structural materials community since Yeh, et al. and Cantor, et al. investigated alloys such as equiatomic CrMnFeCoNi (Cantor alloy) which was found to form a single FCC solid solution [1, 2]. Since then, multiple studies have characterized the cryogenic, room temperature, and high temperature properties of the Cantor alloy and other FCC MPEAs [3]. These FCC MPEAs have been found to exhibit excellent mechanical properties at cryogenic temperatures [4]. However, their high temperature properties have not surpassed those of conventional Ni-based superalloys [5, 6].

Senkov, et al. applied the concept of MPEAs to BCC refractory metals and studied alloys such as equiatomic TaNbHfZrTi (commonly referred to as the Senkov alloy) which forms a single-phase BCC structure [7, 8]. Notably, the high ductility of the Senkov alloy at cryogenic, room temperature, and high temperature while maintaining high strength in both tension and compression sets it apart from other conventional BCC alloys [8, 9]. The mechanical properties of the Senkov alloy and various other BCC MPEAs have since been investigated with a focus on high temperature properties for energy conversion systems and other applications in extreme environments [10, 11]. However, the creep properties of BCC refractory MPEAs (RMPEA) have only recently been reported in two studies by Liu, et al. and Gadelmeier, et al. [12, 13]. These creep studies of RMPEAs both investigated the Senkov alloy over different stress and

---

temperature ranges and found solute drag controlled dislocation creep at low stress and a stress exponent typical of dislocation climb controlled creep at high stresses [12, 13]. These results are consistent with the creep behavior of other refractory alloys such as Ta - 2.5 wt% W reported by Lin, et al. [14]. To broaden the understanding of creep in RMPEAs through the first constant tensile stress creep study, this investigation focuses on the tensile creep properties of an $Nb_{45}Ta_{25}Ti_{15}Hf_{15}$ RMPEA. This composition is chosen based on published reports regarding the roles of various elements in refractory alloys [15] and is a modified version of an RMPEA designed by Zhang, et al. [16]. A high at% of Nb was used because it has a low ductile to brittle transition temperature, a relatively low density, and good oxidation resistance among refractory metals. Ta and Ti were included to promote solid solution strengthening which is critically important for stable creep strength at high temperatures and Hf is utilized for grain boundary strengthening.

5.2 Experimental Methods

The $Nb_{45}Ta_{25}Ti_{15}Hf_{15}$ RMPEA was fabricated by arc-melting 45 at% Nb, 25 at% Ta, 15 at% Ti, and 15 at% Hf. Oxidation during the arc-melting process was limited by pulling a vacuum of 1 x 10^{-5} torr on the chamber and then backfilling it with ultra high purity Ar. Additionally, a Ti getter was melted in the chamber before melting the $Nb_{45}Ta_{25}Ti_{15}Hf_{15}$. The arc-melted buttons were flipped and remelted five times to promote homogeneity. The material then underwent a 90% thickness reduction via cold rolling to a final thickness of 0.6 mm and the rolled sheets were annealed at 1373 K for 1 hour. Two specimens were then electrical discharge machined from each of the six rolled sheets. Fig. 5-1 illustrates an isometric view of a tensile creep specimen with gage section dimensions of 35.56 (L) x 2.54(W) x 0.6(T) mm. All surfaces and edges of the

gage sections were polished using 600 grit SiC paper to minimize the possibility of surface

defects influencing creep properties.
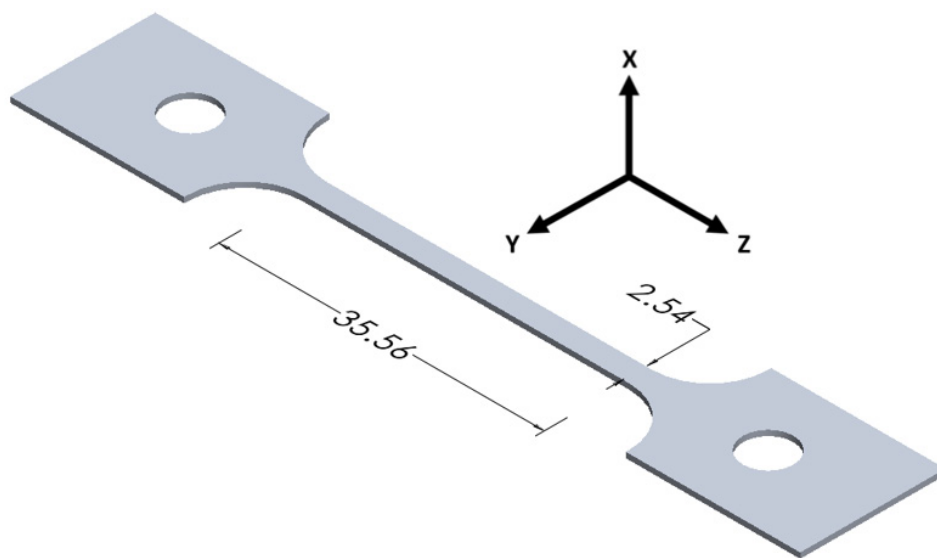
Fig. 5-1 Isometric view of a creep specimen. All dimensions are in mm.

Constant stress tensile creep tests were performed at a temperature of 1173 K and stress range of 50-300 MPa with additional tests performed at temperatures of 1123 K and 1223 K and stresses of 100 MPa and 250 MPa to determine activation energies. All tests were conducted until fracture to clearly identify the steady state creep rate. To minimize oxidation during testing, a vacuum of 3×10^{-5} torr was pulled on the furnace chamber which was subsequently backfilled with a constant flow of ultra high purity Ar maintaining a positive pressure above atmospheric to prevent oxygen from entering the chamber. Additionally, the specimens were surrounded by Ti foil to getter any residual oxygen. Furnace heat up and stabilization took approximately 3.5 hours. The testing procedures described for this study are a modified version of those described in previous studies of FCC materials which are less prone to oxidation [6, 17, 18].

Scanning electron microscopy (SEM) was performed on a Thermo Fisher Quattro S ESEM and an FEI Scios Dual Beam FIB/SEM equipped with energy dispersive x-ray spectroscopy (EDS) and electron backscatter diffraction (EBSD) detectors. All microscopy samples were prepared by grinding and polishing to 0.3 μm with an alumina suspension and then vibropolishing with 0.05 μm colloidal silica for 4 to 7 hours. The Quattro ESEM was used in backscatter electron mode to characterize the fractured specimens. The Scios FIB/SEM was used to characterize atomic composition via EDS at an operating voltage of 30 kV and the grain orientations and boundary misorientations via EBSD at an operating voltage of 15 kV and step size of 0.3 μm. The EBSD data were post-processed in MATLAB with MTEX (version 5.7.0) following a procedure similar to that employed in previous studies such that unreasonably small grains are removed and unindexed data points are filled based on the orientations of their neighbors [6, 18, 19]. Average grain size was determined from the EBSD grain boundary maps using the line intercept method.

5.3 Results and Discussion

5.3.1 Characterization of Initial Microstructure

Many RMPEAs have been observed to form a single BCC phase, however, some compositions result in two-phase BCC structures or dual-phase alloys consisting of BCC regions and intermetallic regions such as Laves, $L1_2$, B2, and sigma [10]. However, previous studies by Zhang, et al. of similar alloys such as $Nb_{55}Ta_{25}Ti_{15}Hf_5$ [16] and $Nb_{40}Ta_{25}Ti_{15}Hf_{15}Zr_5$ [20] have used X-ray diffraction to determine a single-phase BCC structure is present in these alloys. As-cast RMPEAs are susceptible to elemental segregation formed during the solidification processes [7, 21]. However, multiple studies, including those by Zhang, et al., have determined that relatively low annealing temperatures and times can be used to homogenize RMPEAs that have had significant thickness reductions from the as-cast state [16, 20, 21]. Conversely, as-cast RMPEA specimens require relatively high annealing temperatures and times for elemental homogenization due to extremely low diffusion rates of the refractory constituents [16, 20, 21]. Therefore, SEM-EDS was used to verify a uniform distribution of the four principal elements in $Nb_{45}Ta_{25}Ti_{15}Hf_{15}$ as illustrated in Fig. 5-2 The EBSD images and inverse pole figure (IPF) contour plots displayed in Fig. 5-3 illustrate that there is minimal texture in this material, however, there is slight misorientation within a few grains which has been observed in other MPEAs as well [5, 6, 18]. Grain boundary misorientation maps (not shown) revealed a uniform distribution of misorientations in this material. A grain size of 10.9 ± 2.1 μm was determined by applying the line intercept method to the EBSD map in Fig. 5-3.
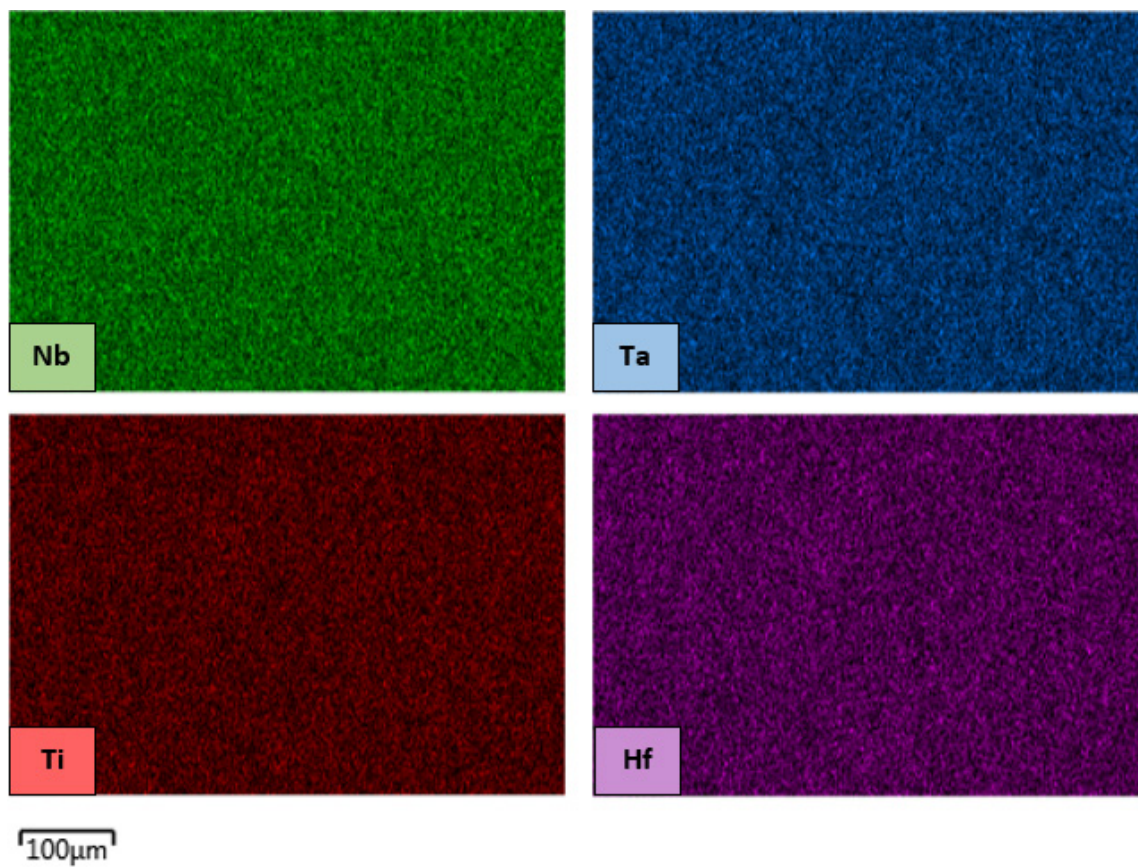
Fig. 5-2 SEM-EDS composition maps of $Nb_{45}Ta_{25}Ti_{15}Hf_{15}$ illustrating a uniform distribution of elements.
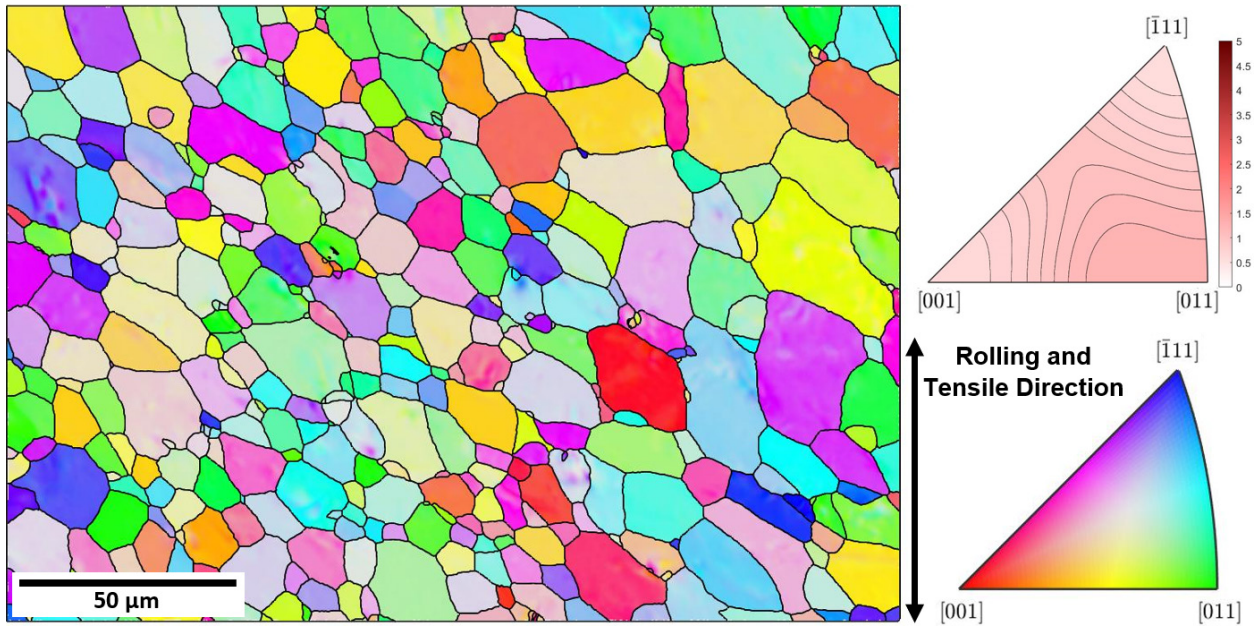
Fig. 5-3 EBSD-IPF color map and IPF contour plot of $Nb_{45}Ta_{25}Ti_{15}Hf_{15}$.

5.3.2 Creep Results and Comparison of MPEA Creep Behavior

Representative creep curves illustrating the effect of variations in temperature and applied stress on $Nb_{45}Ta_{25}Ti_{15}Hf_{15}$ are presented in Fig. 5-4. Distinct normal primary, secondary, and tertiary regions are observed in the creep curves which is typical of pure metals and alloys that behave like pure metals. However, this material exhibits a relatively brief secondary regime and an exceptionally long tertiary regime representative of its excellent damage tolerance. It is noted that two specimens, including the one tested at 1123 K and 250 MPa, ruptured before extensive tertiary creep occurred. As shown below, premature rupture occurred due to pre-existing voids in the creep specimens from the casting process; however, these voids did not affect the steady state creep rate, $\dot{\varepsilon}_{SS}$ which was measured at low strains (typically less than 3%).

The power law equation (Eq. (5.1)) is commonly used to describe the relationship between $\dot{\varepsilon}_{SS}$ and applied stress, σ, where A is a material constant that includes dislocation structure, Q_C represents the creep activation energy, R is the gas constant, and T is temperature [22].
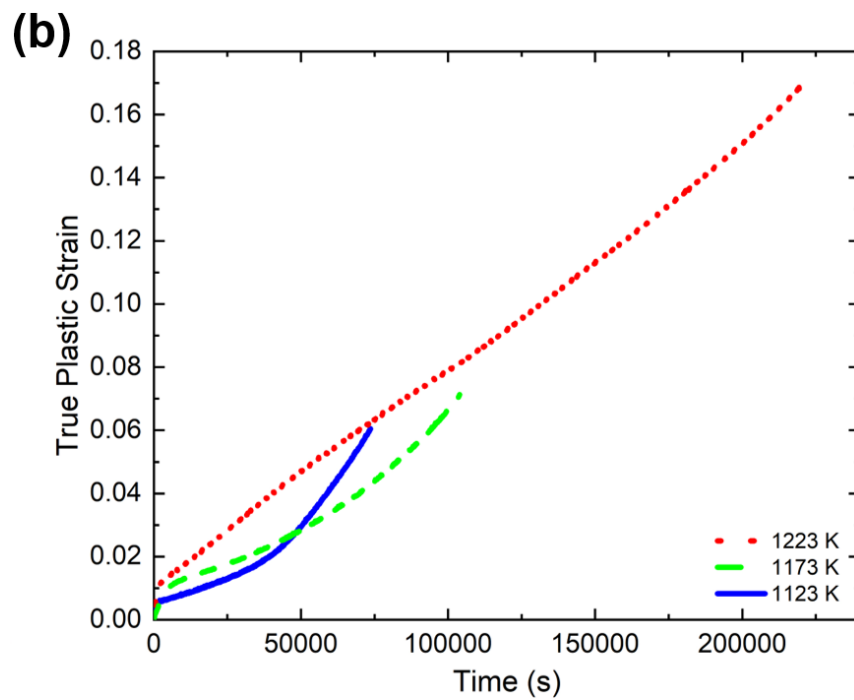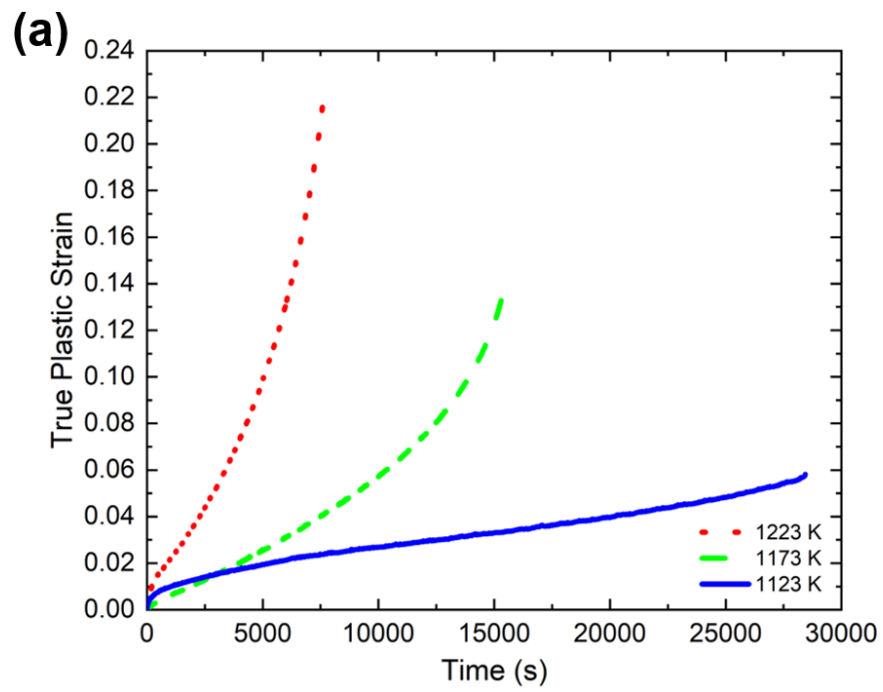
Fig. 5-4 Representative creep curves of Nb$_{45}$Ta$_{25}$Ti$_{15}$Hf$_{15}$ at (a) 250 MPa (b) 100 MPa.

$$\dot{\varepsilon}_{SS} = A\sigma^n \exp\left(-\frac{Q_C}{RT}\right) \tag{5.1}$$

A double logarithmic plot of the relationship between steady-state creep rates at 1173 K, which were calculated from the slopes of the secondary region of the creep curves, and applied stresses is illustrated in Fig. 5-5 to determine the stress exponent of this material in the tested stress range. Bilinear fits with two stress exponents are observed, suggesting different creep deformation mechanisms at low and high applied stress. A stress exponent of 1.2 was found for the low applied stress region of 50-150 MPa while a stress exponent of 5.7 was observed for the high applied stress region of 200-300 MPa. In the framework of the power law creep model, the stress exponent of 1.2 is typically associated with creep deformation controlled by diffusion (n = 1) and the stress exponent of 5.7 is in the range commonly associated with the dislocation climb mechanism of creep deformation (n = 4-6) in subgrain forming metals. However, the testing temperature is too low to expect diffusion-controlled creep in this refractory alloy. This bilinear stress exponent behavior was also observed by Gadelmeier, et al. in a constant tensile load creep study of the Senkov alloy, with an exponent in the typical range for grain boundary sliding controlled creep (n = 2) at low applied stress and an exponent in the range associated with dislocation climb controlled creep at high applied stress [13]. Liu, et al. also conducted a constant tensile load creep study of the Senkov alloy for small applied stresses and found an average stress exponent of n = 2.6 ± 0.1, which is between the common ranges for grain boundary sliding and solute drag controlled creep (n = 3) according to the power law creep model [12]. It is important to note that the grain size in the work of Liu, et al. is much larger than in the study by Gadelmeier, et al. However, with a stress exponent between the typical values for grain boundary sliding and solute drag controlled creep, it is difficult to determine if the larger

grain size caused this difference from the grain boundary sliding reported by Gadelmeier, et al. [12, 13].

These conflicting reports of stress exponents can be rationalized by adopting the thermally activated glide model of creep deformation based on the work of Kocks, Argon, and Ashby [23] and applied to creep deformation by Nix and Gibeling [24] as shown in Eq. (5.2):

$$\dot{\varepsilon} = \dot{\varepsilon}_0 \exp\left(-\frac{\Delta G}{k_B T}\right) \qquad (5.2)$$

where $\dot{\varepsilon}$ is the plastic strain rate, $\dot{\varepsilon}_0$ is the reference strain rate, k_B is the Boltzmann constant, T is temperature, and ΔG is the Gibbs free energy of activation which can be defined as given by:

$$\Delta G = \Delta F - \left(\frac{\sigma b \Delta a''}{M}\right) \qquad (5.3)$$

where ΔF is the Helmholtz free energy of activation, σ is the applied normal stress, b is the magnitude of the Burgers vector, $\Delta a''$ is the operational activation area, and M is the Taylor factor. As observed in Eqs. (5.2 and 5.3), the rate of deformation in the thermally activated glide model is controlled by the rate at which dislocations overcome obstacles by thermal activation. This model has previously been used to describe the creep behavior in the Cantor alloy [25]. It is also noted that the thermally activated glide model is directly related to physical aspects of the material while the power law model is purely phenomenological in nature. Since power law breakdown is known to occur at high stress [24, 26], another approach that has been used to describe creep behavior at high stress is a hyperbolic sine model, however, this model is also phenomenological [17]. As such, OriginPro was used to apply an exponential fit consistent with the thermally activated glide model to the data in Fig. 5-5 revealing that the stress assisted and thermally activated glide model can adequately represent the $Nb_{45}Ta_{25}Ti_{15}Hf_{15}$ creep data

without resorting to a description involving different mechanisms at high and low stresses. It is noted that more detailed experiments such as constant structure stress reduction creep tests must be performed to accurately quantify parameters such as ΔF and $\Delta a''$ [27-29].
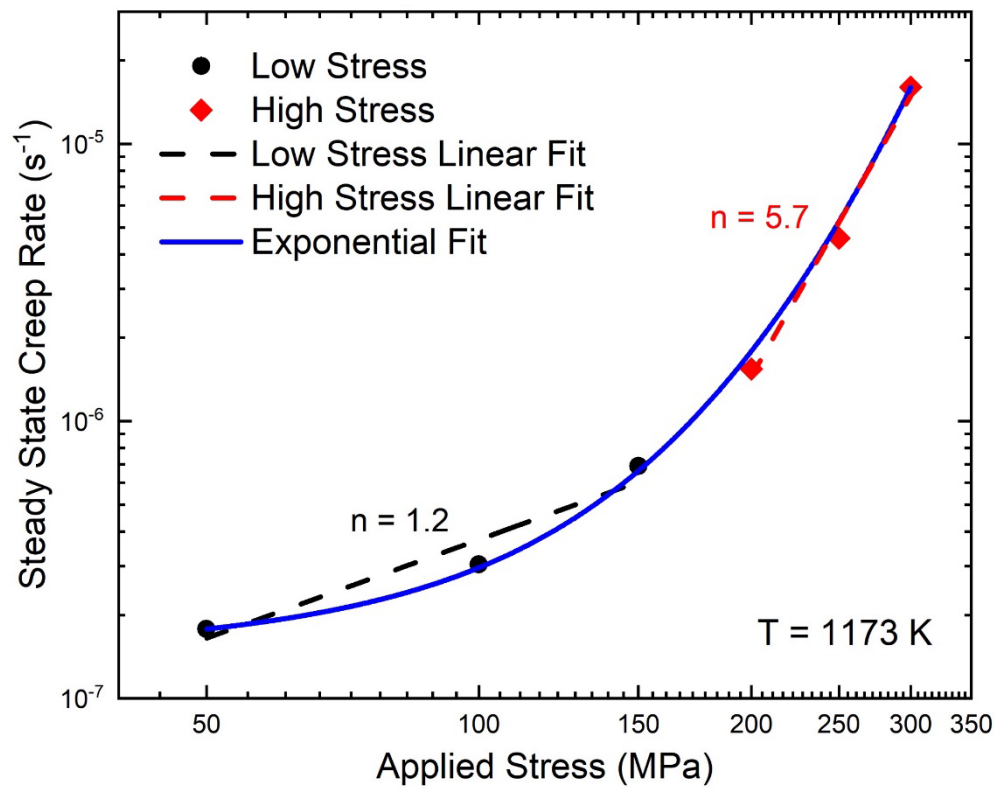
Fig. 5-5 Log-log plot of steady state creep rate vs applied stress at 1173 K for $Nb_{45}Ta_{25}Ti_{15}Hf_{15}$ illustrating a bilinear power law creep fit, and an exponential thermally activated glide fit.

Fig. 5-6 illustrates a comparison of the creep resistance of the $Nb_{45}Ta_{25}Ti_{15}Hf_{15}$ alloy to the most

creep resistant, non-strengthened, FCC MPEA reported to date, CrCoNi, as well as the Senkov

alloy as described above [6, 12, 13]. Creep data for the Senkov alloy have not been published at

1173 K for direct comparison to the present study, therefore the published data at 1253 K [13]

have been used to estimate the creep resistance at 1173 K by adjusting the results using the

published activation energy [12]. Unfortunately, the activation energy has only been published

for the Senkov alloy in the low stress regime resulting in an inability to estimate its high stress

creep resistance at 1173 K [12]. The data presented in Fig. 5-6 demonstrate that the creep rates of

$Nb_{45}Ta_{25}Ti_{15}Hf_{15}$ are more than three orders of magnitude lower than those in CrCoNi in the

high stress regime. However, the exponential nature of the creep data due to stress assisted and

thermally activated dislocation glide results in converging creep resistance at low stress provided

there is no change in slope for the CrCoNi alloy. This result implies that FCC MPEAs are better

suited for applications with applied stresses lower than ~10 MPa due to their superior oxidation

resistance compared to RMPEAs. This observation also highlights the excellent high stress

tensile creep resistance of RMPEAs. Activation energies of $Nb_{45}Ta_{25}Ti_{15}Hf_{15}$ in the high and low

stress regime were determined from a semi-log plot of steady state creep rate versus 1/T as

illustrated in Fig. 5-7. Although the creep resistance of the Senkov alloy at 1173 K could not be

estimated from the published data, the high stress activation energy of $Nb_{45}Ta_{25}Ti_{15}Hf_{15}$ was

used to estimate its creep resistance at 1253 K as shown in Fig. 5-6 for direct comparison to the

Senkov alloy in the high stress regime. As shown by these estimated results, it can be concluded

that $Nb_{45}Ta_{25}Ti_{15}Hf_{15}$ has a superior creep resistance compared to the Senkov alloy at all but the

lowest applied stresses.
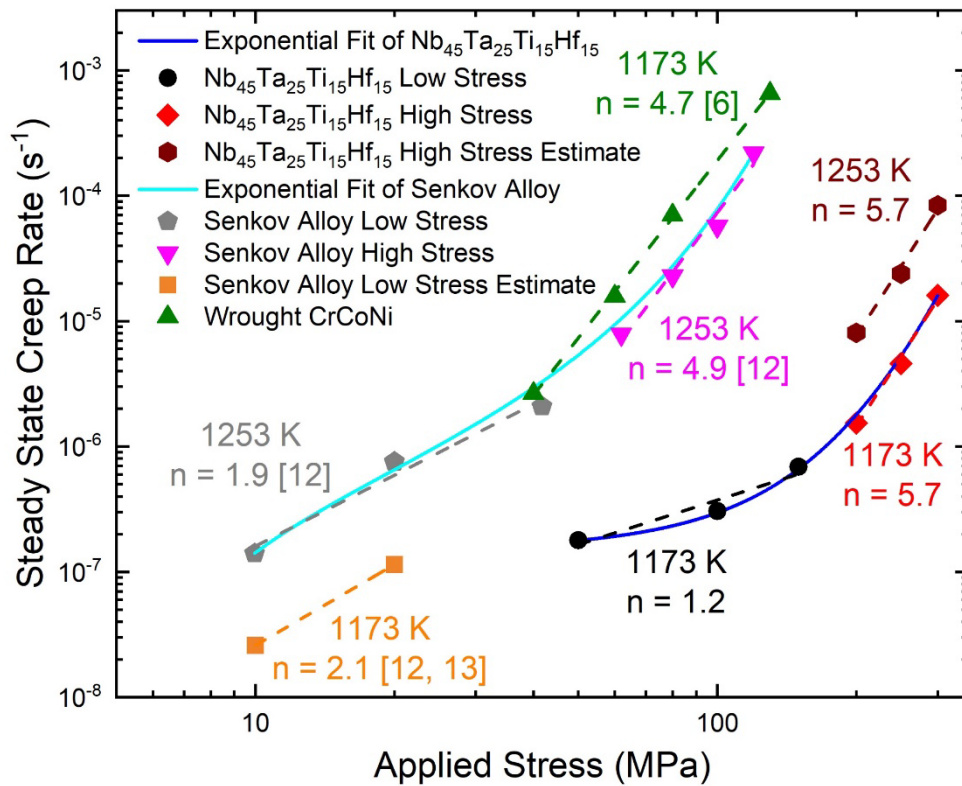
Fig. 5-6 Comparison of creep rate vs applied stress for CrCoNi [6], the Senkov alloy [12, 13], and Nb$_{45}$Ta$_{25}$Ti$_{15}$Hf$_{15}$.
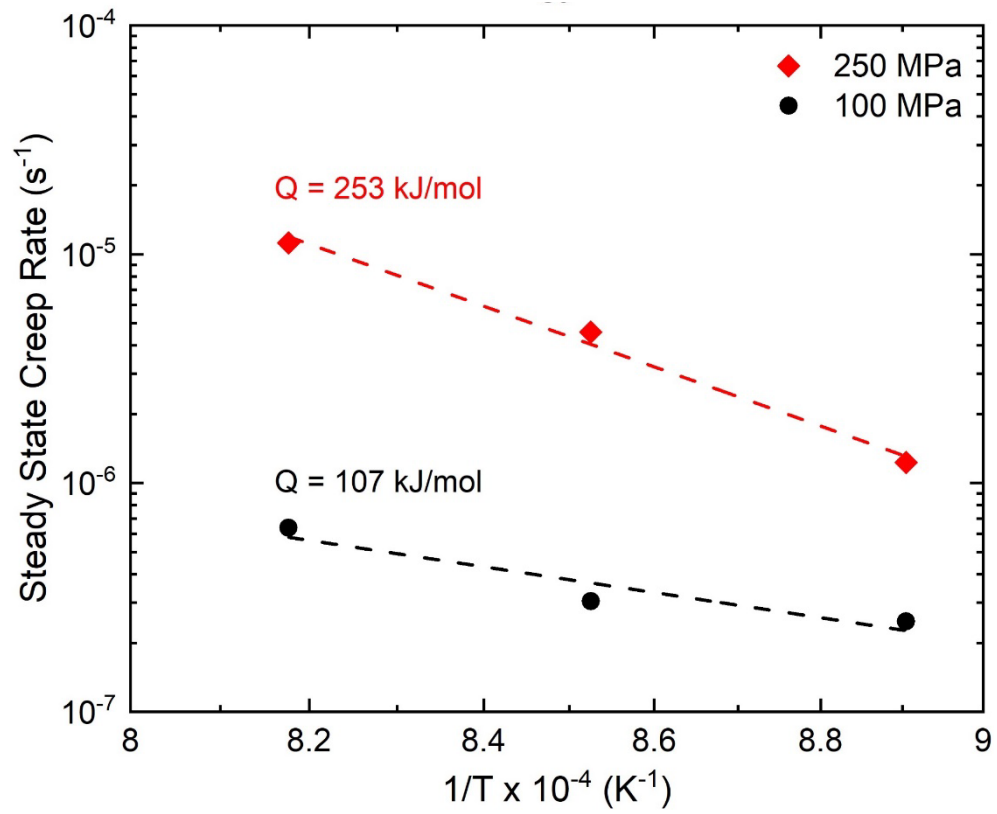
Fig. 5-7 Semi-log plot of steady state creep rate vs 1/T for $Nb_{45}Ta_{25}Ti_{15}Hf_{15}$ illustrating high and low stress activation energies.

5.3.3 Fracture Characteristics of Nb$_{45}$Ta$_{25}$Ti$_{15}$Hf$_{15}$

As observed in Fig. 5-8(a), brittle intergranular fracture as well as ductile fracture due to void nucleation and coalescence are both present in the specimen that was crept at 1173 K and 250 MPa. It is noted that ductile fracture resembling the typical creep rupture mechanism of void nucleation and coalescence due to stress concentrations on grain boundary triple points due to boundary sliding, dislocation pile-ups against boundaries, as well as hard particles on grain boundaries is present in the center of the gage cross-section [30-34]. Conversely, the brittle intergranular fracture is observed in regions adjacent to the specimen surfaces indicating that its cause is correlated to the testing environment. It is also observed in Fig. 5-8(b) that the specimen crept at 1173 K and 100 MPa displays almost entirely brittle intergranular fracture with virtually no typical ductile void nucleation and coalescence fracture in the center. This observation suggests that the brittle intergranular fracture is a time dependent phenomenon as the creep life of the specimen in Fig. 5-8(a) was 4.3 hours and the creep life of the specimen in Fig. 5-8(b) was 28.9 hours.

SEM-EDS of a fractured specimen revealed Hf-oxides at grain boundaries as illustrated in Figs. 5-9 and 5-10. Although precautions such as high vacuum, inert gas, and a Ti getter were used to minimize oxidation, refractory alloys are extremely prone to the effects of oxygen. Conway and Flagella suggested a rigorous operating procedure for creep testing of refractory alloys up to 3273 K [35]. This procedure includes furnace chamber evacuation to 10^{-5} torr, closing off the vacuum system and ensuring a low leak rate, then raising the furnace temperature to 1273 K while the evacuation operation is still in progress to maintain a pressure below 1 x 10^{-3} torr. After reaching 1273 K and a vacuum level of 1 x 10^{-5} torr, the vacuum pumps are isolated from the furnace system and inert gas is introduced. When the pressure reaches atmospheric, the furnace

chamber is again evacuated and backfilled. The temperature is then increased to the testing temperature [35]. Additionally, Conway and Flagella indicate that if inert gas is not used, a vacuum of approximately 1 x 10^{-8} torr is required to effectively minimize contamination in refractory alloys [35]. A single cycle of furnace evacuation and inert gas backfilling was used in this study, however, the test system used is not capable of maintaining a low leak rate, so it is possible that oxygen entered the system in between isolating the vacuum system and backfilling the furnace with argon leading to the brittle intergranular fracture observed in Fig. 5-8. Virtual leaks such as oxygen trapped in threaded surfaces may have also contributed to specimen oxidation. It is noted that Lui, et al. conducted creep tests under vacuum of 1.5 x 10^{-6} torr without inert gas [12], which may also be inadequate to prevent oxidation although this point cannot be verified from the evidence presented in that work. Additionally, the vacuum level was not reported in the study by Gadelmeier, et al. [13]. This discussion of oxidation in refractory alloys suggests that currently published RMPEA creep data, including this study, at low applied stress, commensurate with long creep life, may be compromised due to specimen oxidation.
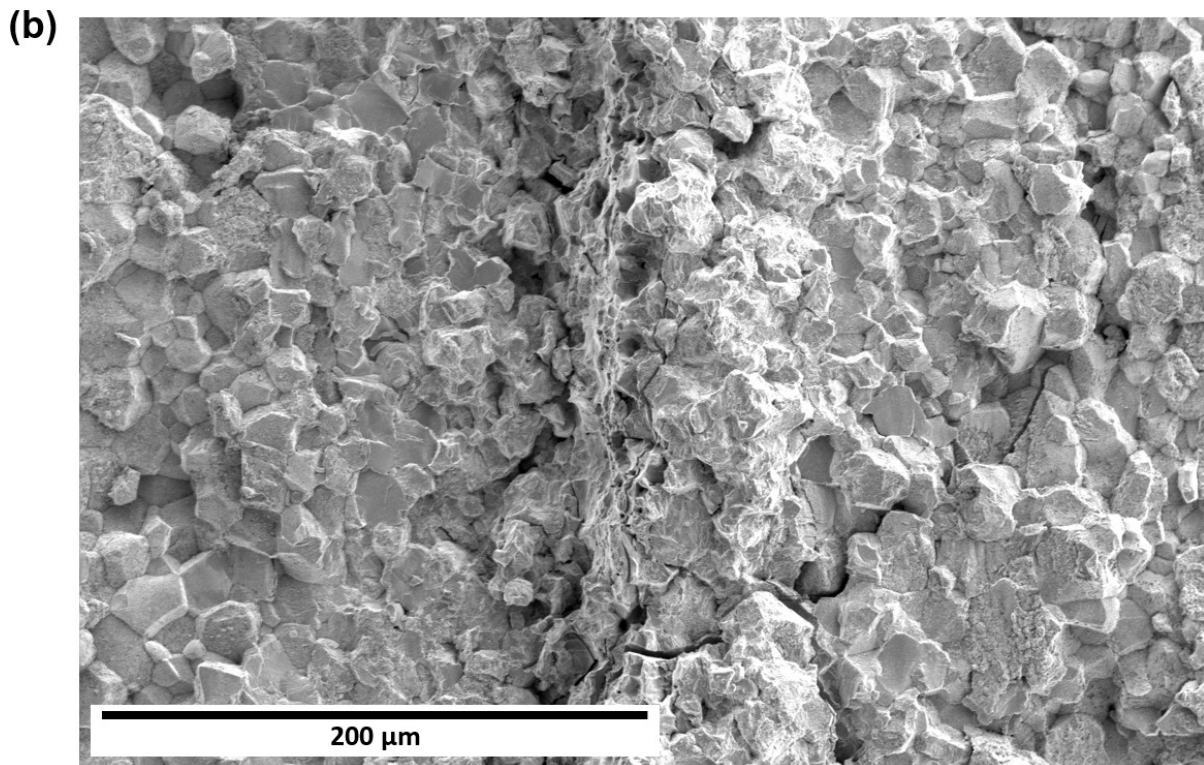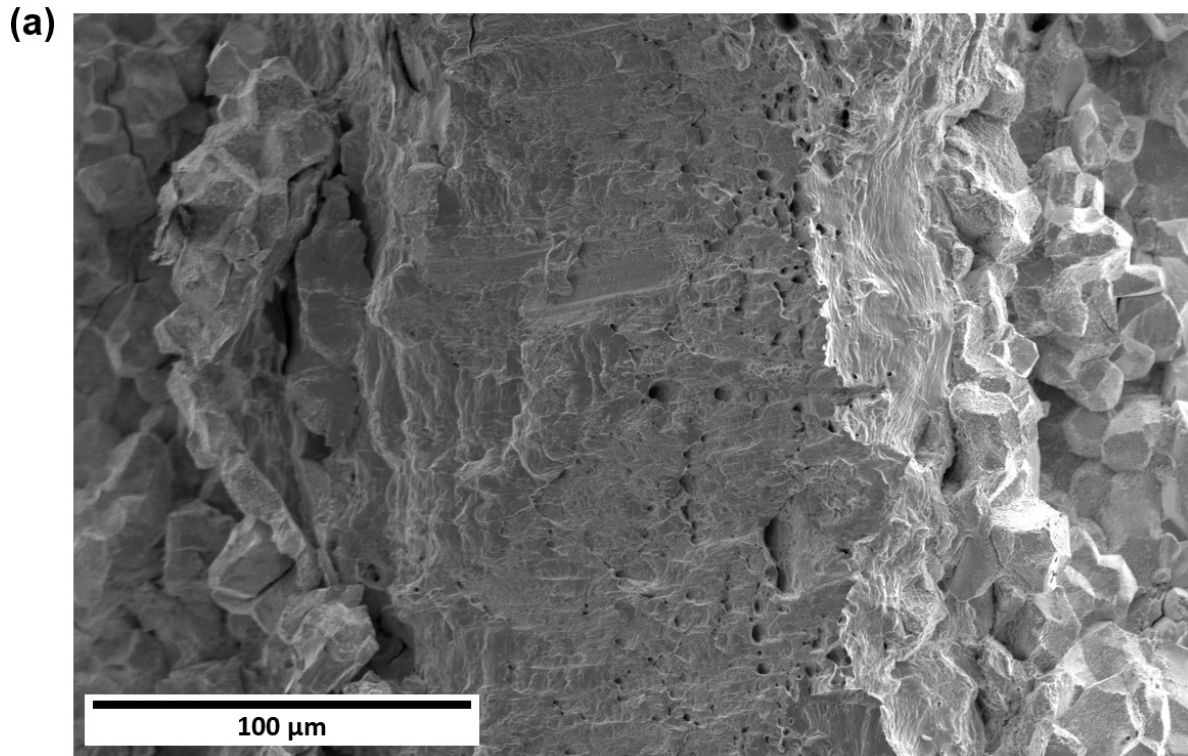
Fig. 5-8 Fracture surface of $Nb_{45}Ta_{25}Ti_{15}Hf_{15}$ ruptured under (a) 1173 K and 250 MPa illustrating intergranular and ductile fracture and (b) 1173 K and 100 MPa showing predominantly intergranular fracture.
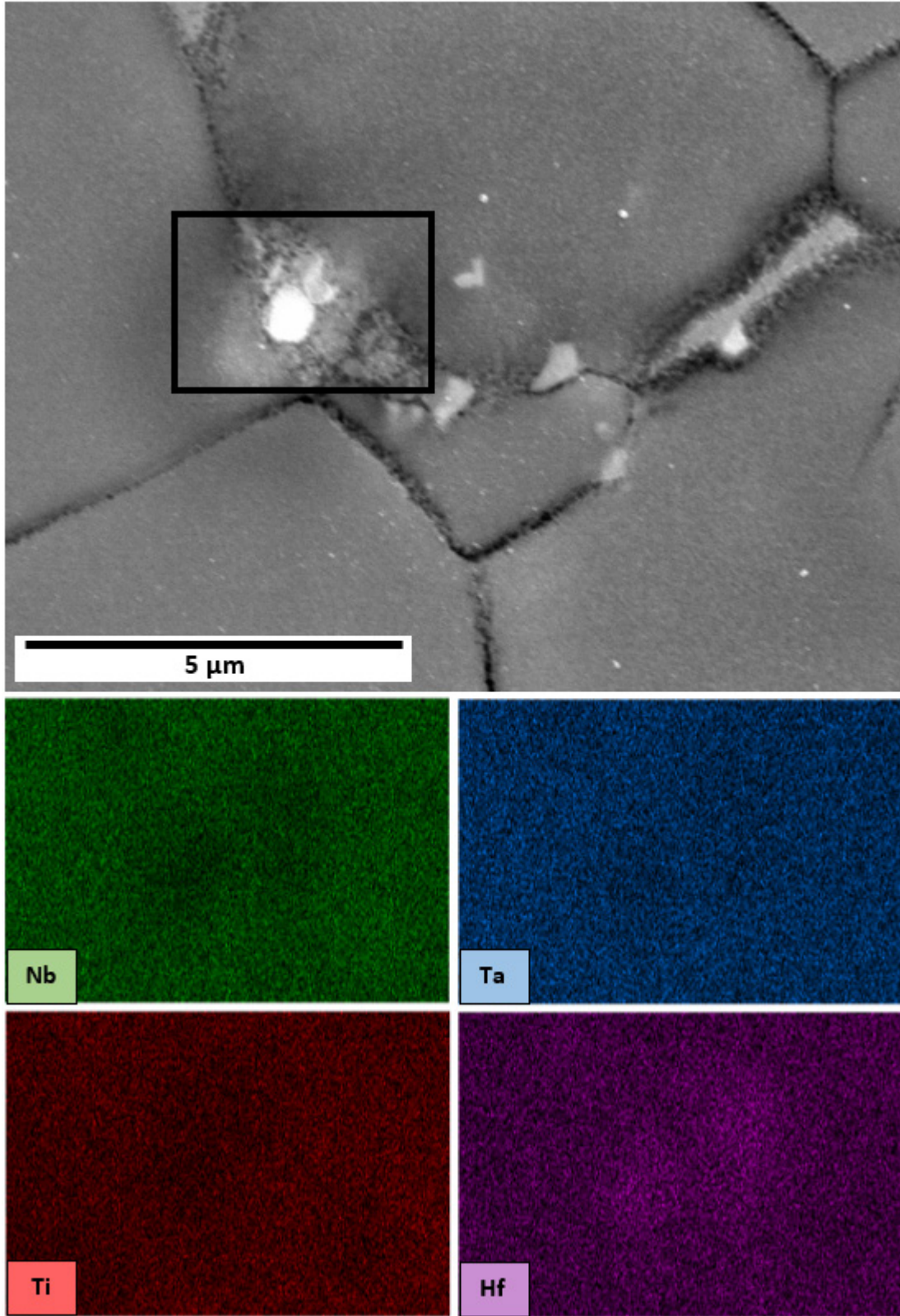
Fig. 5-9 SEM-EDS of a Hf-oxide at a grain boundary in $Nb_{45}Ta_{25}Ti_{15}Hf_{15}$ following creep rupture.
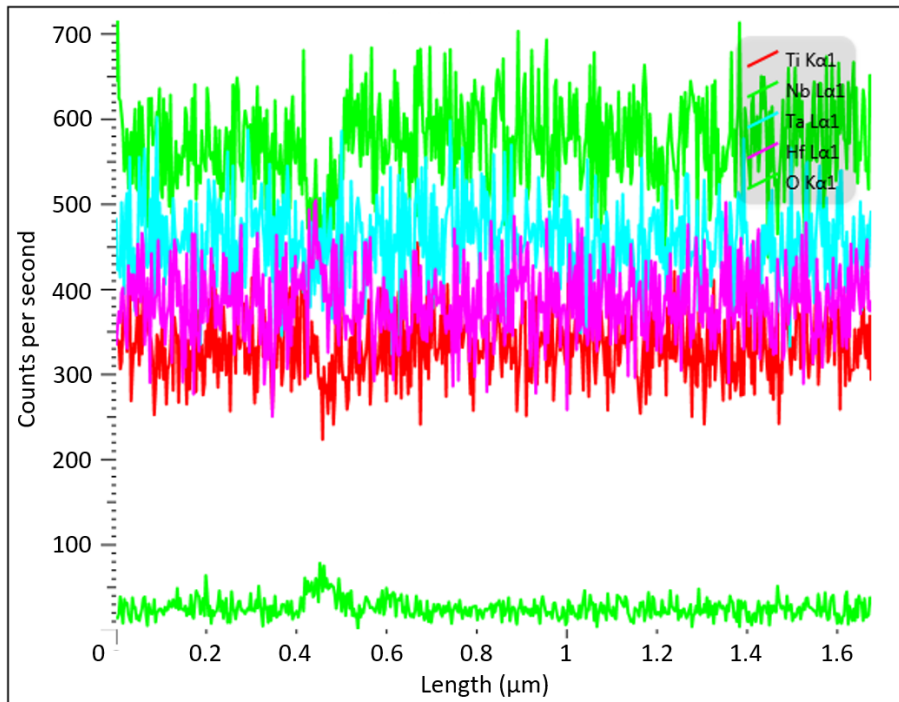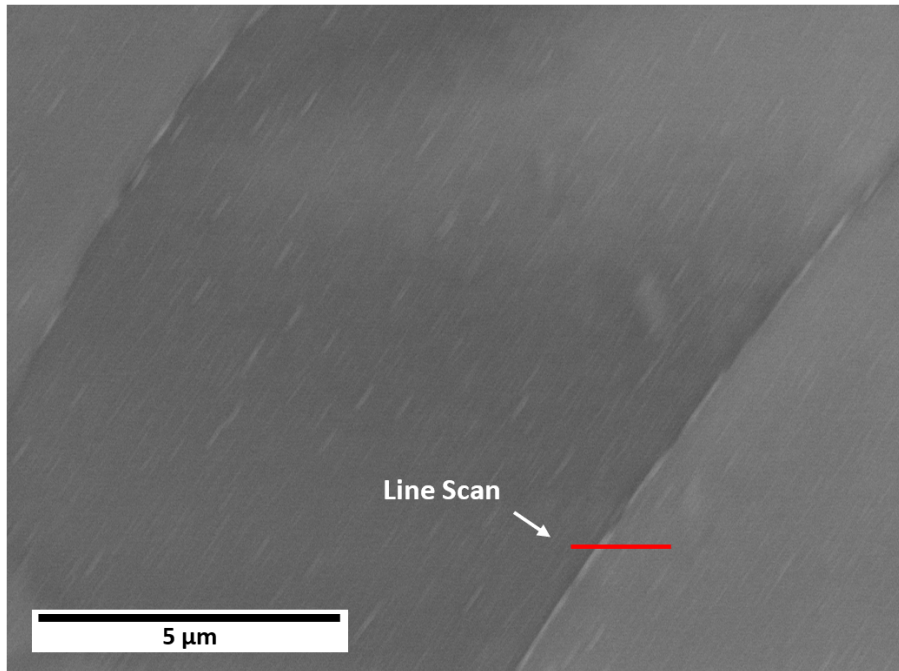
Fig. 5-10 SEM-EDS line scan revealing increased Hf and O at grain boundary of $Nb_{45}Ta_{25}Ti_{15}Hf_{15}$ following creep rupture.

To further explore the relationship between ductility, creep rupture time, and steady state strain rate, a Monkman-Grant plot is presented in Fig. 5-11. A linear fit of all the data reveals that the Monkman-Grant relationship is generally obeyed with a slope of -0.94 ± 0.16. However, the coefficient of determination (R^2) is only 0.8 due to systematically low creep rupture life as a result of oxygen contamination, with this effect becoming more severe with increased time. Despite its presence above the Monkman-Grant fit line, the specimen that was crept at 1223 K and 100 MPa, which exhibited a creep life of over 200,000 seconds, was also affected by oxygen contamination. Fig. 5-12 shows brittle intergranular fracture on the entire fracture surface of this specimen, which is consistent with oxidation over such a long creep life. While the creep life of 61.3 hours and creep ductility of 17% of the specimen crept at 1223 K and 100 MPa are greater than those of the specimen crept at 1173 K and 100 MPa, these values are consistent with the extremely high creep ductilities of the Senkov alloy tested at 1253-1523 K as reported by Liu, et al and Gadelmeier, et al. [12, 13]. These observations support the inference that the creep rates measured in the low stress regime (large lifetimes) may be artificially influenced by oxygen intrusion. Therefore, creep rates in the low stress regime may be artificially high due to a premature transition to tertiary creep. Additional steps to further limit the entry of oxygen into the testing system may lead to even higher creep ductilities and lower creep rates. Additionally, the poor fit of the creep data on the Monkman-Grant plot is influenced by voids in the specimens crept at 1173K and 300 MPa and 1123 K and 250 MPa resulting in artificially low creep rupture times, as described below.
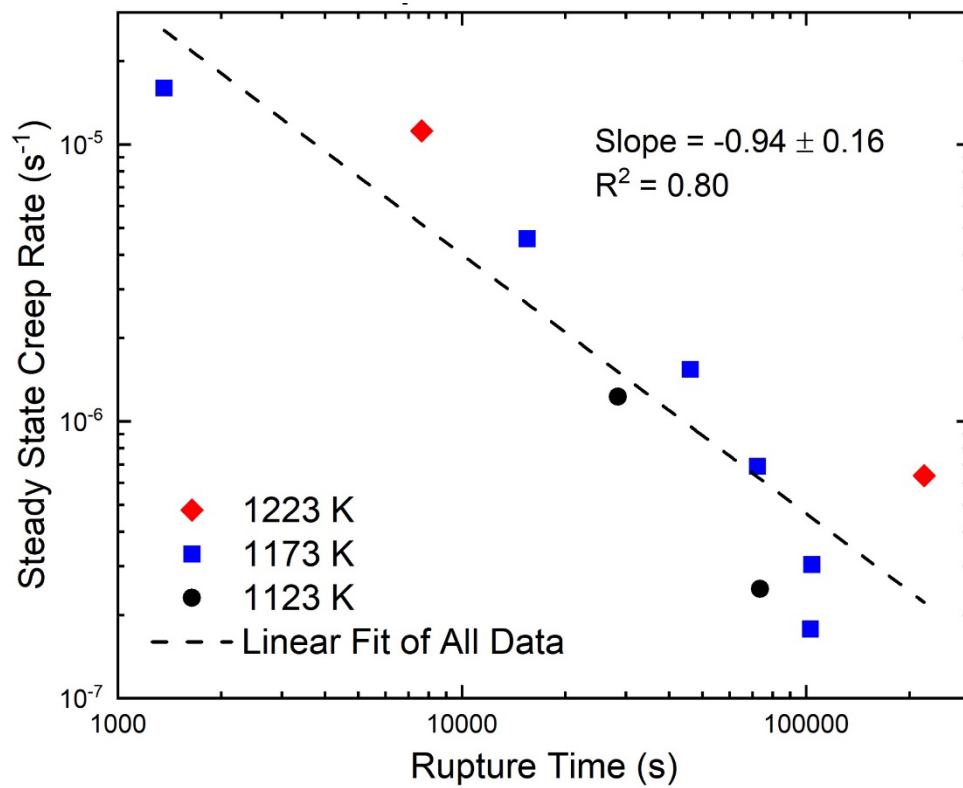
Fig. 5-11 Monkman-Grant plot of $Nb_{45}Ta_{25}Ti_{15}Hf_{15}$ creep data.
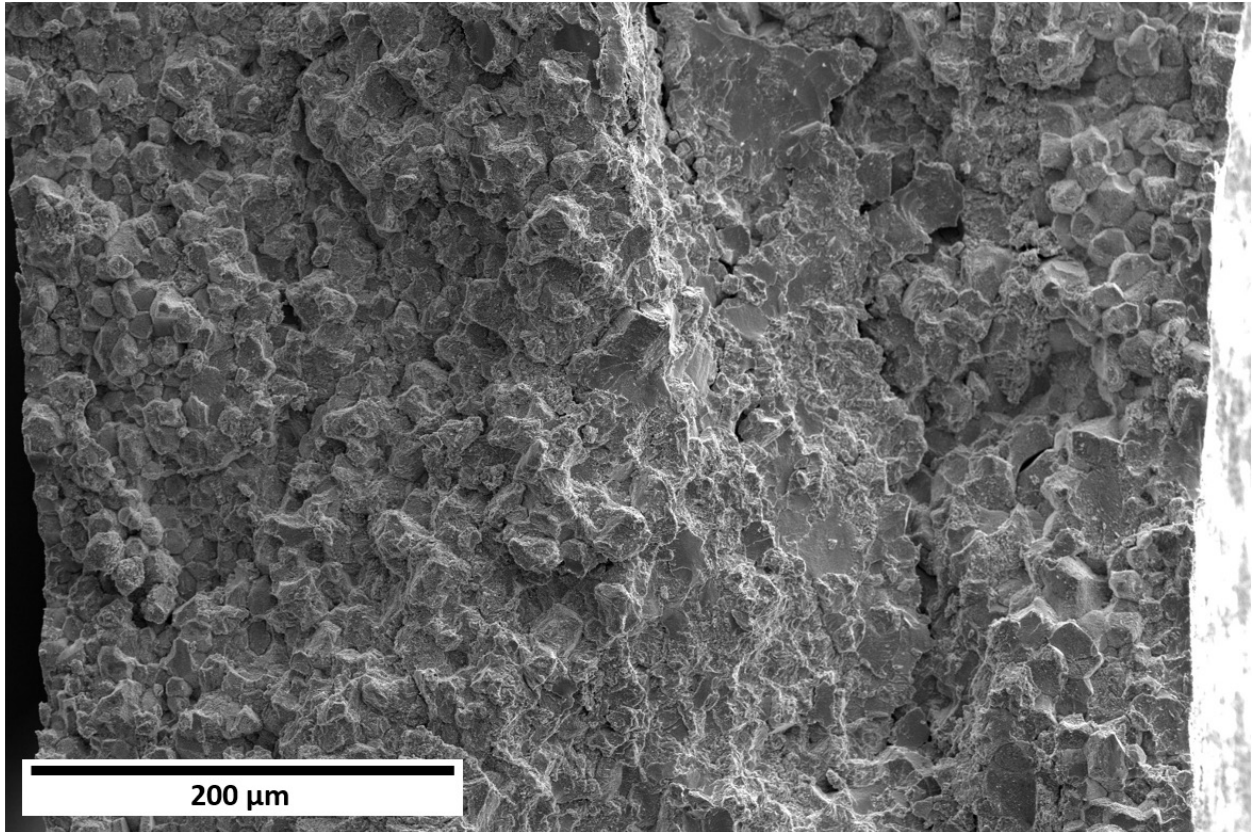
Fig. 5-12 Fracture surface of $Nb_{45}Ta_{25}Ti_{15}Hf_{15}$ ruptured under 1223 K and 100 MPa showing brittle intergranular fracture on the entire fracture surface.

The average creep ductility of specimens that did not have voids and ruptured before extensive brittle intergranular fracture due to oxidation (< 70,000 creep rupture time) was found to be 16.7 ± 3.6%. Fig. 5-13 shows the gage surface of a $Nb_{45}Ta_{25}Ti_{15}Hf_{15}$ creep specimen following rupture at 1173 K and 250 MPa near the fracture surface and at the end of the gage section. Cracking is observed along the entire gage section revealing the excellent damage tolerance of $Nb_{45}Ta_{25}Ti_{15}Hf_{15}$ and reflecting its superb creep ductility compared to conventional BCC alloys. Fig. 5-14 illustrates the gage surface following creep rupture of a specimen tested at 1173 K and 100 MPa. Severe cracking is observed near the fracture surface, but minimal cracking is observed at the end of the gage section. Part of this difference between specimens with short and long creep lives can again be attributed to the effects of oxidation. After the initial onset of cracking in the specimen in Fig. 5-14 with a creep life of 28.9 hours and creep ductility of 7.1%, the cracks provide paths for oxygen to enter the specimen and degrade the grain boundaries over a long period of time leading to more extensive brittle intergranular fracture than in the specimen in Fig. 5-13 with a creep life of 4.3 hours and creep ductility of 13.9%. Fig. 5-15 illustrates the relationship between creep ductility and applied stress, revealing that at a uniform temperature the creep ductility decreases with decreasing applied stress. However, as observed in Figs. 5-8 to 5-14, premature rupture is correlated to more extensive oxidation over longer creep times which occurs as a result of low applied stress. Due to the limited data available in this study, it is not possible to separate the influence of oxygen on ductility and steady state creep rate. As seen in Figs. 5-4, 5-11, and 5-15, specimens tested at 1123 K and 250 MPa and 1173 K and 300 MPa exhibited creep ductilities and creep rupture times lower than expected compared to the rest of the specimens. As observed from the fracture surface of one of these specimens in Fig. 5-16, these low ductilities are due to voids in the specimens from the casting process. A few voids

attributed to the casting process are visible in Fig. 5-8a as well, however, these are smaller and less extensive than in Fig. 5-16. It is also noted again that the creep ductility significantly increases from 1173 K to 1223 K which is similar to the extremely high creep ductility of the Senkov alloy tested at temperatures ranging 1253-1523 K [12, 13].

(a) Fracture surface

(b) 1 mm | End of gage section
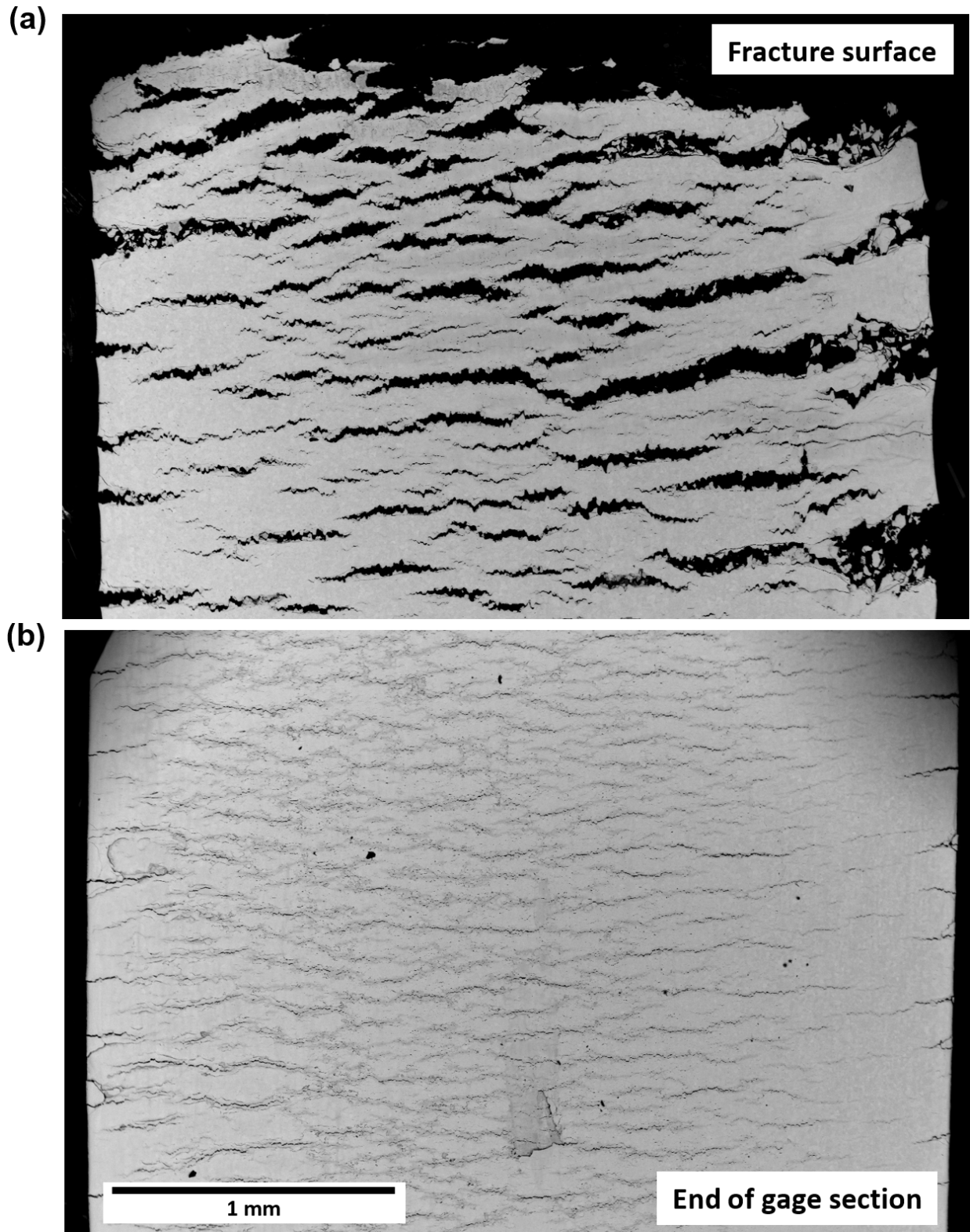
Fig. 5-13 Gage surface of $Nb_{45}Ta_{25}Ti_{15}Hf_{15}$ creep specimen following ruptured at 1173 K and 250 MPa near (a) the fracture surface and (b) the end of the gage section near the grip section.
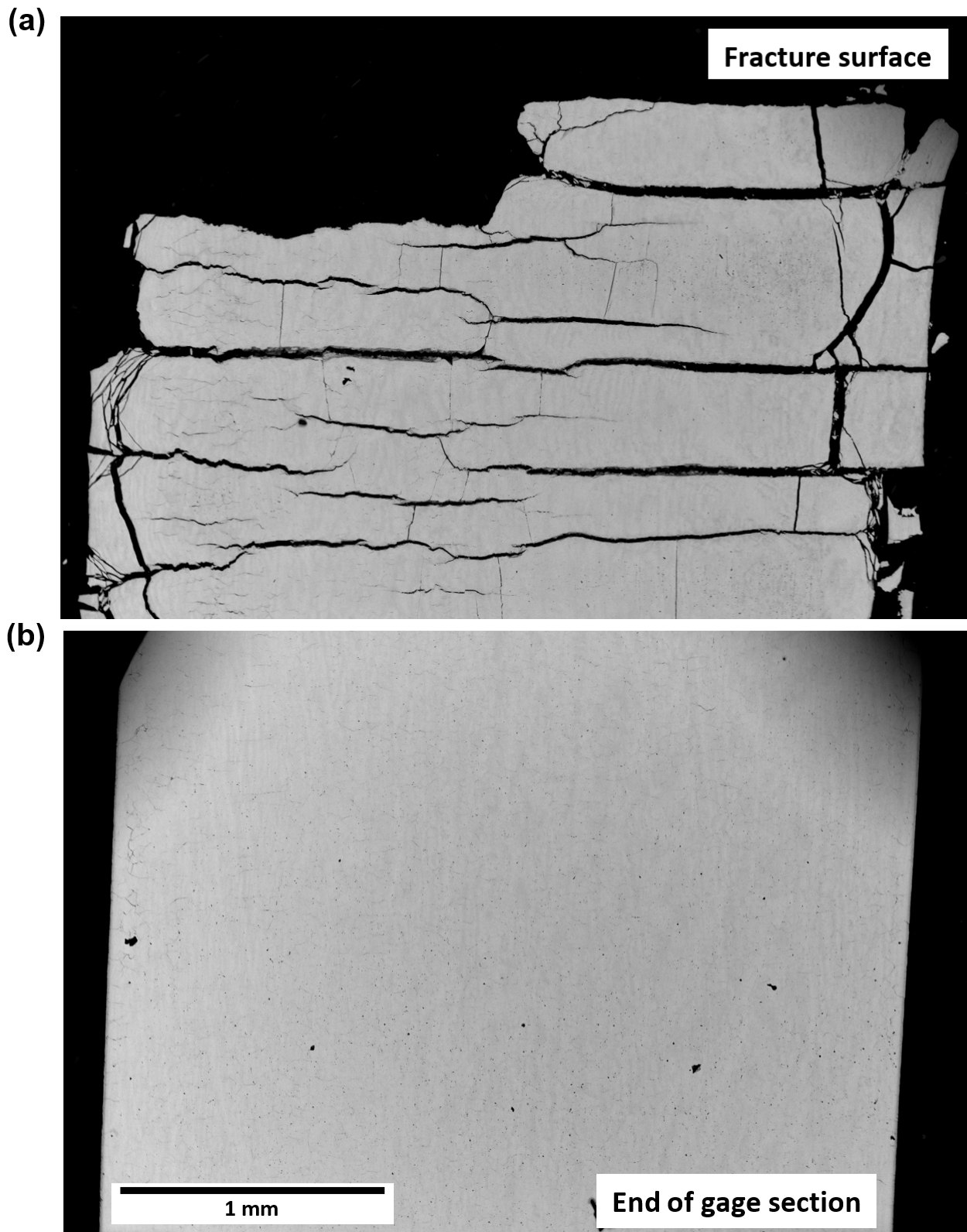
Fig. 5-14 Gage surface of $Nb_{45}Ta_{25}Ti_{15}Hf_{15}$ creep specimen following ruptured at 1173 K and 100 MPa near (a) the fracture surface and (b) the end of the gage section near the grip section.
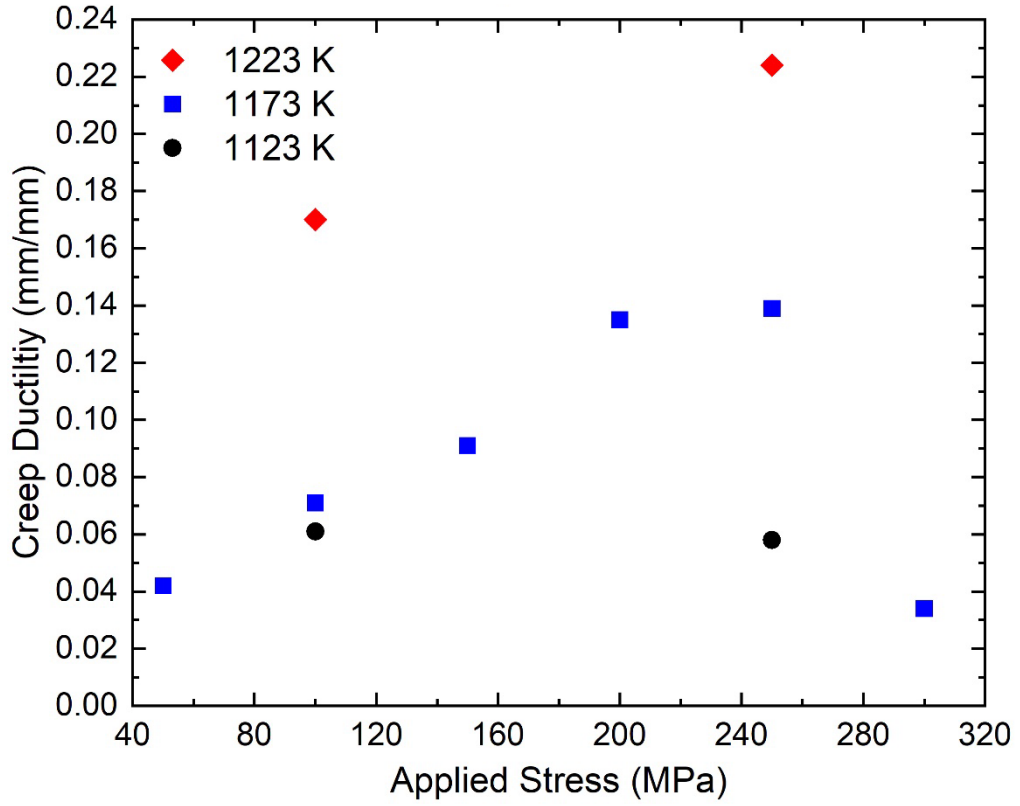
Fig. 5-15 Creep ductility of $Nb_{45}Ta_{25}Ti_{15}Hf_{15}$.
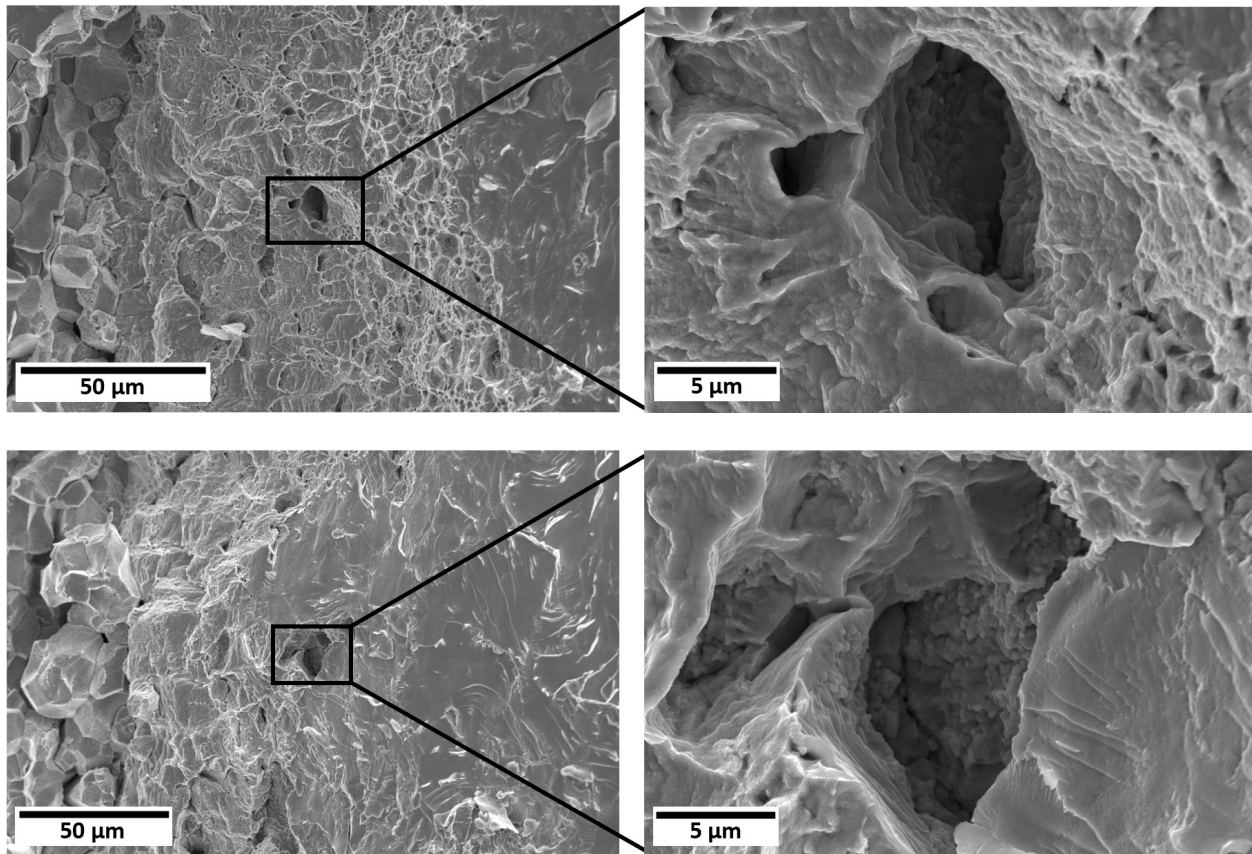
Fig. 5-16 Fracture surface of $Nb_{45}Ta_{25}Ti_{15}Hf_{15}$ ruptured under 1173 K and 300 MPa illustrating voids from the casting process.

5.4 Conclusions

Constant stress creep tests in the ranges of 1123-1223 K and 50-300 MPa were conducted on an arc melted $Nb_{45}Ta_{25}Ti_{15}Hf_{15}$ refractory multi-principal element alloy (RMPEA) to determine its creep behavior. The results for $Nb_{45}Ta_{25}Ti_{15}Hf_{15}$ were compared to the most creep resistant FCC MPEA to date, CrCoNi, and the only other RMPEA for which creep data have been published, equiatomic TaNbHfZrTi, (Senkov alloy).

1. Creep deformation in the $Nb_{45}Ta_{25}Ti_{15}Hf_{15}$ alloy was determined to be controlled by stress assisted and thermally activated dislocation glide with oxygen contamination resulting in artificially high creep rates in the low stress regime. However, $Nb_{45}Ta_{25}Ti_{15}Hf_{15}$ exhibited excellent high stress creep resistance in the tested stress range.

2. $Nb_{45}Ta_{25}Ti_{15}Hf_{15}$ has a superior creep resistance compared to the Senkov alloy at all but the lowest applied stresses. However, convergence of data for a reference FCC MPEA with the RMPEA creep rates at low stress (~10 MPa) indicate that FCC MPEAs are better suited for applications with low applied stresses due to their superior oxidation resistance.

3. The $Nb_{45}Ta_{25}Ti_{15}Hf_{15}$ RMPEA exhibited excellent creep ductility compared to conventional BCC alloys due to its superb damage tolerance, with creep ductility increasing significantly at 1223 K.

4. Characterization of fracture surfaces and specimen gage surfaces post fracture indicates that poor creep resistance, creep ductility, and creep life at low applied stress may be an artifact of Hf-oxide formation at grain boundaries. This implies that if processing and testing can be conducted in an environment with less oxygen than was present in this

study and other RMPEA studies, the creep behavior of RMPEAs at low applied stress may be better than the values currently reported.

Acknowledgements

References

[1]   J.W. Yeh, S.K. Chen, S.J. Lin, J.Y. Gan, T.S. Chin, T.T. Shun, C.H. Tsau, S.Y. Chang, Nanostructured high-entropy alloys with multiple principal elements: Novel alloy design concepts and outcomes, Advanced Engineering Materials 6(5) (2004) 299-303.
[2]   B. Cantor, I.T.H. Chang, P. Knight, A.J.B. Vincent, Microstructural development in equiatomic multicomponent alloys, Materials Science and Engineering: A 375-377 (2004) 213-218.
[3]   D.B. Miracle, O.N. Senkov, A critical review of high entropy alloys and related concepts, Acta Materialia 122 (2017) 448-511.
[4]   B. Gludovatz, A. Hohenwarter, D. Catoor, E.H. Chang, E.P. George, R.O. Ritchie, A fracture-resistant high-entropy alloy for cryogenic applications, Science 345(6201) (2014) 1153-1158.
[5]   M. Zhang, E.P. George, J.C. Gibeling, Tensile creep properties of a CrMnFeCoNi high-entropy alloy, Scripta Materialia 194 (2021).
[6]   G. Sahragard-Monfared, M. Zhang, T.M. Smith, A.M. Minor, E.P. George, J.C. Gibeling, The influence of processing methods on creep of wrought and additively manufactured CrCoNi multi-principal element alloys, submitted to Acta Materialia.
[7]   O.N. Senkov, G.B. Wilks, D.B. Miracle, C.P. Chuang, P.K. Liaw, Refractory high-entropy alloys, Intermetallics 18(9) (2010) 1758-1765.

[8] O.N. Senkov, J.M. Scott, S.V. Senkova, D.B. Miracle, C.F. Woodward, Microstructure and room temperature properties of a high-entropy TaNbHfZrTi alloy, Journal of Alloys and Compounds 509(20) (2011) 6043-6048.

[9] S.B. Wang, M.X. Wu, D. Shu, G.L. Zhu, D.H. Wang, B.D. Sun, Mechanical instability and tensile properties of TiZrHfNbTa high entropy alloy at cryogenic temperatures, Acta Materialia 201 (2020) 517-527.

[10] O.N. Senkov, D.B. Miracle, K.J. Chaput, J. Couzinie, Development and exploration of refractory high entropy alloys—A review, Journal of Materials Research 33(19) (2018) 3092-3128.

[11] O.N. Senkov, S. Gorsse, D.B. Miracle, High temperature strength of refractory complex concentrated alloys, Acta Materialia 175 (2019) 394-405.

[12] C. Liu, C. Gadelmeier, S. Lu, J. Yeh, H. Yen, S. Gorsse, U. Glatzel, A. Yeh, Tensile creep behavior of HfNbTaTiZr refractory high entropy alloy at elevated temperatures, Acta Materialia 237 (2022).

[13] C. Gadelmeier, Y. Yang, U. Glatzel, E.P. George, Creep strength of refractory high-entropy alloy TiZrHfNbTa and comparison with Ni-base superalloy CMSX-4, Cell Reports Physical Science 3(8) (2022).

[14] Z. Lin, E.J. Lavernia, F.A. Mohamed, High-temperature deformation in a Ta-W alloy, Acta Materialia 47(4) (1999) 1181-1194.

[15] F.C. Campbell, Elements of metallurgy and engineering alloys, ASM International, Materials Park, Ohio, 2008.

[16] C. Zhang, B.E. MacDonald, F.W. Guo, H.R. Wang, C.Y. Zhu, X. Liu, Y.W. Kang, X.C. Xie, Y.Z. Zhou, K.S. Vecchio, E.J. Lavernia, Cold-workable refractory complex concentrated alloys with tunable microstructure and good room-temperature tensile behavior, Scripta Materialia 188 (2020) 16-20.

[17] M.W. Decker, J.R. Groza, J.C. Gibeling, Creep properties of an extruded copper-8% chromium-4% niobium alloy, Mat Sci Eng a-Struct 369(1-2) (2004) 101-111.

[18] G. Sahragard-Monfared, M. Zhang, T.M. Smith, A.M. Minor, J.C. Gibeling, Superior tensile creep behavior of a novel oxide dispersion strengthened CrCoNi multi-principal element alloy, submitted to Acta Materialia.

[19] S.E. Broyles, M. Zhang, J.C. Gibeling, Influence of annealing on the creep behavior of GlidCop Al-15, Materials Science & Engineering A 779 (2020).

[20] C. Zhang, H.R. Wang, X.Y. Wang, Q. Yu, C.Y. Zhu, M.J. Xu, S.T. Zhao, R. Kou, X. Wang, B.E. MacDonald, R.C. Reed, K.S. Vecchio, P.H. Cao, T.J. Rupert, E.J. Lavernia, Strong and ductile refractory high-entropy alloys with super formability, Acta Materialia 245 (2023).

[21] S.L. Wei, S.J. Kim, J.Y. Kang, Y. Zhang, Y.J. Zhang, T. Furuhara, E.S. Park, C.C. Tasan, Natural-mixing guided design of refractory high-entropy alloys with as-cast tensile ductility, Nat Mater 19(11) (2020) 1175-+.

[22] O.D. Sherby, P.M. Burke, Mechanical behavior of crystalline solids at elevated temperature, Progress in Materials Science 13 (1968) 323-390.

[23] U.F. Kocks, A.S. Argon, M.F. Ashby, Thermodynamics and kinetics of slip, Progress in Materials Science 19 (1975).

[24] W.D. Nix, J.C. Gibeling, Mechanisms of Time-Dependent Flow and Fracture of Metals, in: R. Raj (Ed.), Flow and Fracture at Elevated Temperatures, American Society for Metals, Metals Park, Ohio, 1985, pp. 1-63.

[25] M. Zhang, E.P. George, J.C. Gibeling, Elevated-temperature deformation mechanisms in a CrMnFeCoNi high-entropy alloy, Acta Materialia 218 (2021).

[26] H.J. Frost, M.F. Ashby, Deformation mechanism maps: the plasticity and creep of metals and ceramics, Pergamon Press, Oxford, 1982.

[27] G.S. Nakayama, J.C. Gibeling, Constant substructure creep of aluminum following stress reductions, Acta Metallurgica et Materialia 38(10) (1990) 2023-2030.

[28] S.E. Broyles, J.C. Gibeling, Constant structure creep of copper at 973K, Scripta Metallurgica et Materialia 33(5) (1995) 767-772.

[29] M. Zhang, S.E. Broyles, J.C. Gibeling, An improved description of creep in dispersion-strengthened metals, Acta Materialia 196 (2020) 384-395.

[30] F.A. McClintok, A criterion for ductile fracture by the growth of holes, Journal of Applied Mechanics 35(2) (1968) 363-371.

[31] R. Lombard, H. Vehoff, Nucleation and growth of cavities at defined grain boundaries in bicrystals, Scripta Metallurgica 24(3) (1990) 581-586.

[32] E.P. George, R.L. Kennedy, D.P. Pope, Review of trace element effects on high-temperature fracture of Fe- and Ni-base alloys, Physica Status Solidi A 167(2) (1998) 313-333.

[33] Y.S. Lee, J. Yu, Effect of matrix hardness on the creep properties of a 12CrMoVNb steel, Metallurgical and Materials Transactions A 30A (1999) 2331-2339.

[34] M.E. Kassner, T.A. Hayes, Creep cavitation in metals, International Journal of Plasticity 19(10) (2003) 1715-1748.

[35] J.B. Conway, P.N. Flagella, U.S. Atomic Energy Commission. Division of Reactor Development and Technology., Creep-rupture data for the refractory metals to high temperatures, Gordon and Breach, New York, 1971.

Chapter 6. Summary of Results and Future Research Opportunities

The influence of processing methods and oxide dispersion strengthening (ODS) on the creep behavior and deformation mechanisms of several FCC multi-principal element alloys (MPEA) and the effect of a BCC crystal structure comprised of refractory elements on the creep behavior of an MPEA was investigated in this dissertation. The materials examined are equiatomic wrought and additively manufactured (AM) CrCoNi, equiatomic AM ODS CrCoNi, and wrought $Nb_{45}Ta_{25}Ti_{15}Hf_{15}$. Constant stress creep tests and stress reduction creep tests were performed to probe creep properties and creep deformation mechanisms as revealed through operational activation areas. Scanning electron microscopy (SEM) and transmission electron microscopy (TEM) were used to observe initial microstructures and dislocation structures, steady state dislocation structures, and fracture surfaces after rupture to further the understanding of underlying creep deformation mechanisms. The most significant conclusions are as follows:

1. A larger percentage of Cr-rich oxides was observed in the AM CrCoNi than its wrought counterpart due to oxygen contamination during the AM process. Dislocation interactions with these oxide particles contributed to the increased creep resistance of the AM material. The particles also limit the area swept by gliding dislocations resulting in less strain per activation event. Additionally, AM processing resulted in a smaller percentage of low angle grain boundaries (LAGB) in the AM material compared to wrought, contributing to its superior creep resistance. The average creep ductility of wrought CrCoNi was higher than the AM material due to the higher volume fraction of oxides in the AM material providing additional cavity nucleation sites leading to more rapid void coalescence and consequent fracture. Similarly, the higher percentage of LAGBs in the wrought material allowed deformation to propagate more readily, reducing the stresses

that cause cavity nucleation at GBs and prolonging fracture. Additionally, the higher percentage of twin boundaries in the AM material do not act as dislocation sources and thereby reduce the possibility of slip transmission on the other side of the boundary.

2. The stress exponent of AM ODS CrCoNi was found to be below the value normally associated with ODS materials, suggesting the addition of 0.6 vol% of yttria is most likely too low to cause significant rate-controlling dislocation/oxide interactions typical of ODS materials. However, the AM ODS CrCoNi exhibited an 84% lower steady state creep rate than its non-ODS counterpart at similar stresses and temperatures indicating that its elongated grain structure and the addition of yttria improved creep resistance. The yttria and Cr-rich oxides in AM ODS CrCoNi act as cavity nucleation sites leading to void coalescence which is expected to decrease creep ductility while a high percentage of LAGBs allow easy propagation of deformation across grain boundaries avoiding the Zener-Stroh mechanism of cavity formation, which should increase creep ductility. The dynamic balance of these two mechanisms appears to favor the easy propagation of slip across LAGB at the highest applied stress leading to higher ductility than in AM CrCoNi.

3. The operational activation areas measured for AM CrCoNi and AM ODS CrCoNi indicate that interaction of gliding dislocations with forest dislocations controls the rate of steady state creep deformation in these alloys. The operational activation areas of both materials are nearly identical revealing that the addition of 0.6 vol% yttria does not affect the mechanism controlling the rate of thermally activated dislocation glide during steady state creep in this alloy. Large stress reductions in AM CrCoNi and AM ODS CrCoNi result in continuously decreasing creep rates while small stress reductions result in creep rates that increase until fracture. These different responses suggest that there is a limit to

how large of a stress reduction can occur, above which the mobile dislocation density is prevented from adjusting to the reduced stress due to dislocation/oxide interactions. Due to the inverse additive nature of activation areas, it can be inferred that the solute effect and dislocation detachment from particles in AM CrCoNi and AM ODS CrCoNi does not control the creep rate of these alloys as significantly as forest dislocation strengthening.

4. Creep deformation in the $Nb_{45}Ta_{25}Ti_{15}Hf_{15}$ RMPEA was determined to be controlled by stress assisted and thermally activated dislocation glide with oxygen contamination resulting in artificially high creep rates in the low stress (long creep life) regime. However, $Nb_{45}Ta_{25}Ti_{15}Hf_{15}$ exhibited excellent high stress creep resistance in the tested stress range, despite embrittlement by oxygen. Convergence of data for a reference FCC MPEA with the RMPEA creep rates at low stress (~10 MPa) indicate that FCC MPEAs are better suited for applications with low applied stresses due to their superior oxidation resistance. The $Nb_{45}Ta_{25}Ti_{15}Hf_{15}$ RMPEA exhibited excellent creep ductility compared to conventional BCC alloys due to its superb damage tolerance. Improvements in the processing and testing environments to reduce oxygen contamination may result in improved creep behavior of RMPEAs at low applied stresses.

The findings of this dissertation research enhance the fundamental understanding of the high temperature mechanistic behavior of MPEAs, which is essential for the application of these alloys to energy conversion systems and other extreme environments applications. AM was determined to result in a property tradeoff between higher creep resistance and lower creep ductility due to oxide formation. However, creep ductility in excess of ~4% is not necessary for most structural applications, so the application significance weighted result is that AM produces a superior alloy. As expected, ODS resulted in higher creep resistance as well. However, the

grain structure post hot isostatic pressing remained elongated due to grain boundaries being pinned by oxides resulting in an unexpected increase in creep ductility. Additionally, forest dislocation interactions were found to be rate limiting despite the presence of these oxides, suggesting that dislocation detachment from particles and the solute effect in these alloys only contributes minimally to the creep deformation behavior. The degradation of creep properties in $Nb_{45}Ta_{25}Ti_{15}Hf_{15}$ due to oxidation, despite a concerted effort to minimize this effect, indicates that oxidation-resistant FCC MPEAs are ideal for applications requiring long creep lifetimes. Regardless, the excellent creep properties of $Nb_{45}Ta_{25}Ti_{15}Hf_{15}$ observed in specimens with short creep lifetimes supports the continued development of RMPEAs. As in all scientific endeavors, as fundamental mechanisms are uncovered more research opportunities arise. A few of the research opportunities that complement the findings in this dissertation are listed below:

1. An unconventional sigmoidal strain-time response was observed in the primary creep regime of wrought and AM CrCoNi. This was also observed in CrMnFeCoNi (Cantor alloy) [1]. The observation of this behavior in these alloys and its dissipation before steady state creep is achieved suggests that it is not dependent on grain structure but instead may be an effect of short-range order or stacking fault tetrahedra. To probe this behavior, it is necessary to observe the dislocation structure of these alloys at consistent strain intervals in the primary creep regime. Due to the high temperature nature of creep testing, the specimens must be cooled quickly to avoid an annealing effect during furnace cool down which could alter the dislocation structure. An optical furnace in conjunction with sufficient cooling water for rapid furnace cooling can be utilized.

2. The rate controlling creep deformation mechanism of AM CrCoNi and AM ODS CrCoNi were sufficiently characterized in this dissertation. However, it would be interesting to

probe the mechanism controlling creep of wrought CrCoNi to determine if it is similar to AM CrCoNi and AM ODS CrCoNi or if it is rate limited by the same solute effect observed in the Cantor alloy. Similarly, probing the rate controlling creep deformation mechanism of an ODS Cantor alloy would strengthen this study as the influence of ODS to the rate controlling mechanism could be investigated bi-directionally.

3. The AM ODS CrCoNi investigated in this study did not achieve a significant extent of particle strengthening, as reflected in the low stress exponents compared to those typical of ODS alloys and the fact that forest dislocation interactions, rather than particles, control the rate of dislocation glide. Therefore, an investigation of an AM ODS CrCoNi alloy with a higher vol% yttria is proposed to potentially increase the creep resistance of this FCC MPEA. In the work presented in this dissertation acoustic mixing was used to coat the CrCoNi powder with yttria before the laser powder bed fusion solidification process. The proposed study may require a new approach to achieve a larger vol% yttria such as utilizing smaller powder particles to increase surface area such that more yttria is incorporated into the alloy. Alternatively, different mixing methods could be investigated.

4. The work in this dissertation investigated the creep behavior of RMPEAs through mechanical testing and SEM. However, oxygen contamination led to artificially high creep rates and low creep ductilities of the specimens tested over long creep lifetimes. It is thus proposed to perform additional constant stress creep tests at high vacuum (1×10^{-8} torr). Alternatively, a more leak resistant testing system could be utilized in conjunction with a multi-stage procedure in which the furnace chamber is filled with ultra high purity Ar gas, evacuated, and filled again. These additional tests can be used to confirm the

observations made in this dissertation. Additionally, detailed characterization of elements/particles on embrittled fracture surfaces observed in this dissertation has not been performed. Similarly, the steady state creep dislocation structure of these alloys has not yet been characterized via TEM. It is thus proposed to utilize scanning TEM energy dispersive x-ray spectroscopy to characterize the observed particles and TEM to further the understanding of creep behavior in RMPEAs by observing the steady state creep dislocation structure.

5. The long-term goal of the work described in this dissertation is the development of an ODS refractory MPEA (RMPEA). It is inferred that with continued tailoring of the RMPEA compositional design space and the additional high temperature stable strengthening effect of ODS, an ODS RMPEA could provide superior creep resistance than conventional Ni-based superalloys. To accomplish this goal, the issue of oxidation must first be resolved. Therefore, it is suggested that future development of RMPEAs focuses on ODS RMPEAs with elements that resist oxygen gathering at grain boundaries or utilize an oxidation-resistant coating. Although achieving high ductility in RMPEAs is scientifically impressive, it is not necessary for engineering applications. This reality is beneficial to implementation of an oxidation-resistant coating as these coatings are generally not compatible with significant elongation.

Reference

[1]   M. Zhang, Creep properties and dislocation kinetics of dispersion-strengthened alloys and multi-principal element alloys, University of California, Davis, 2021.

Appendix: List of Creep Data

Table A1 Constant stress creep data for wrought CrCoNi. These data correspond to the results presented in Chapter 2.

Material	Test Method	Temperature (K)	Stress (MPa)	Steady State Creep Rate (s^{-1})	Creep Ductility (%)	Creep Life (s)
Wrought CrCoNi	Constant Stress	1023	60	4.15×10^{-7}	21.3	398751
			80	1.68×10^{-6}	16.4	78576
			130	1.31×10^{-5}	16.8	10167
			200	9.30×10^{-5}	14.6	1233
		1073	60	1.89×10^{-6}	16.2	67372
			80	5.40×10^{-6}	20.1	26303
			130	5.86×10^{-5}	17.2	2216
			200	2.84×10^{-4}	17.9	459
		1098	200	5.81×10^{-4}	17.3	226
		1123	40	1.21×10^{-6}	18.9	120054
			60	5.57×10^{-6}	17.3	23497
			80	1.97×10^{-5}	15.0	5753
			130	1.89×10^{-4}	17.6	683
			200	1.17×10^{-3}	19.3	126
		1173	40	2.65×10^{-6}	18.1	50094
			60	1.58×10^{-5}	17.0	7278
			80	7.02×10^{-5}	17.0	1691
			130	6.53×10^{-4}	18.2	204

Table A2 Constant stress creep data for AM CrCoNi and annealed AM CrCoNi. These data correspond to the results presented in Chapter 2.

Material	Test Method	Temperature (K)	Stress (MPa)	Steady State Creep Rate (s^{-1})	Creep Ductility (%)	Creep Life (s)
AM CrCoNi	Constant Stress	1023	60	4.60×10^{-8}	8.1	909524
			80	1.96×10^{-7}	6.3	205487
			130	3.89×10^{-6}	7.6	13914
			200	6.34×10^{-5}	6.9	937
		1073	60	2.73×10^{-7}	6.5	152575
			80	1.29×10^{-6}	6.2	31855
			130	2.19×10^{-5}	8.1	2737
			200	3.95×10^{-4}	6.9	146
		1098	200	8.60×10^{-4}	7.5	74
		1123	40	1.35×10^{-7}	5.1	225054
			60	1.45×10^{-6}	6	26333
			80	6.66×10^{-6}	7.5	7103
			130	1.13×10^{-4}	8.1	537
			200	1.79×10^{-3}	8.2	38
		1173	40	5.37×10^{-7}	4.9	56692
			60	6.56×10^{-6}	6.8	6173
			80	2.82×10^{-5}	8.5	1727
			130	4.85×10^{-4}	9.4	142
Annealed AM CrCoNi		1073	60	2.74×10^{-7}	6.7	144532
			80	1.54×10^{-6}	6.9	29653
			130	2.66×10^{-5}	8.5	2245
			200	4.65×10^{-4}	7.4	124

Table A3 Constant stress creep data for AM ODS CrCoNi. These data correspond to the results presented in Chapter 3.

Material	Test Method	Temperature (K)	Stress (MPa)	Steady State Creep Rate (s^{-1})	Creep Ductility (%)	Creep Life (s)
AM ODS CrCoNi	Constant Stress	1023	80	2.11×10^{-8}	--	--
			100	7.19×10^{-8}	5.7	356689
			130	4.52×10^{-7}	9.1	138289
			200	9.15×10^{-6}	14.2	12809
		1073	60	3.53×10^{-8}	--	--
			80	1.54×10^{-7}	6.3	395324
			130	4.76×10^{-6}	6.8	10331
			200	7.23×10^{-5}	17.4	1923
		1123	60	1.94×10^{-7}	7.4	257692
			80	1.01×10^{-6}	8	51494
			130	1.97×10^{-5}	11.2	4555
			200	4.83×10^{-4}	19.5	345
		1148	60	2.96×10^{-7}	11	244255
		1173	60	8.68×10^{-7}	9.1	65332
			80	5.15×10^{-6}	6.7	7663
			130	9.63×10^{-5}	11.8	1035
			200	2.12×10^{-3}	22.5	94

Table A4 Stress reduction creep data for AM CrCoNi and ODS AM CrCoNi. These data correspond to the results presented in Chapter 4.

Material	Test Method	Temperature (K)	Initial Stress (MPa)	Reduced Stress (MPa)	$\dot{\varepsilon}_A$ (s^{-1})	$\dot{\varepsilon}_C$ (s^{-1})	$\dot{\varepsilon}_D$ (s^{-1})
AM CrCoNi	Stress Reduction	1073	130	100	1.38x10^{-5}	1.24x10^{-6}	2.31x10^{-6}
				80	1.48x10^{-5}	7.45x10^{-7}	5.43x10^{-7}
				80	1.26x10^{-5}	6.03x10^{-7}	5.45x10^{-7}
				60	1.28x10^{-5}	1.10x10^{-7}	5.91x10^{-8}
AM ODS CrCoNi				100	4.20x10^{-6}	3.44x10^{-7}	6.71x10^{-7}
				100	3.20x10^{-6}	2.70x10^{-7}	6.75x10^{-7}
				80	2.98x10^{-6}	1.12x10^{-7}	1.66x10^{-7}
				60	4.09x10^{-6}	4.63x10^{-8}	4.03x10^{-8}

Table A5 Constant stress creep data for $Nb_{45}Ta_{25}Ti_{15}Hf_{15}$. These data correspond to the results presented in Chapter 5.

Material	Test Method	Temperature (K)	Stress (MPa)	Steady State Creep Rate (s^{-1})	Creep Ductility (%)	Creep Life (s)
$Nb_{45}Ta_{25}Ti_{15}Hf_{15}$	Constant Stress	1123	100	2.48×10^{-7}	6.1	73638
			250	1.23×10^{-6}	5.8	28445
		1173	50	1.78×10^{-7}	4.2	103132
			100	3.04×10^{-7}	7.1	103964
			150	6.88×10^{-7}	9.1	72284
			200	1.54×10^{-6}	13.5	46128
			250	4.57×10^{-6}	13.9	15424
			300	1.60×10^{-5}	3.4	1363
		1223	100	6.37×10^{-7}	17	220770
			250	1.12×10^{-5}	22.4	7639